PREDICTION OF DRAG FORCE ON GIMBAL SYSTEM VIA BALANCE TECHNIQUE AND WAKE INTEGRATION METHOD

A THESIS SUBMITTED TO
THE GRADUATE SCHOOL OF NATURAL AND APPLIED SCIENCES
OF
MIDDLE EAST TECHNICAL UNIVERSITY

BY

EMRAH YEŞİLYURT

IN PARTIAL FULFILLMENT OF THE REQUIREMENTS
FOR
THE DEGREE OF MASTER OF SCIENCE
IN
MECHANICAL ENGINEERING

JANUARY 2014

Approval of the thesis:

PREDICTION OF DRAG FORCE ON GIMBAL SYSTEM VIA BALANCE TECHNIQUE AND WAKE INTEGRATION METHOD

submitted by **EMRAH YEŞİLYURT** in partial fulfillment of the requirements for the degree of **Master of Philosophy in Mechanical Engineering Department, Middle East Technical University** by,

Prof. Dr. Canan Özgen _____
Dean, Graduate School of **Natural and Applied Sciences**

Prof. Dr. Süha Oral _____
Head of Department, **Mechanical Engineering**

Prof. Dr. Kahraman Albayrak _____
Supervisor, **Mechanical Engineering Dept., METU**

Examining Committee Members:

Assoc. Prof. Dr. Cemil Yamalı _____
Mechanical Engineering Dept., METU

Prof. Dr. Kahraman Albayrak _____
Mechanical Engineering Dept., METU

Asst. Prof. Dr. Cüneyt Sert _____
Mechanical Engineering Dept., METU

Asst. Prof. Dr. M. Metin Yavuz _____
Mechanical Engineering Dept., METU

Dr. Tolga Köktürk _____
Senior Expert Engineer, ASELSAN

Date: 22 January 2014

I hereby declare that all information in this document has been obtained and presented in accordance with academic rules and ethical conduct. I also declare that, as required by these rules and conduct, I have fully cited and referenced and results that are not original to this work.

Name, Last name: Emrah Yeşilyurt

Signature :

ABSTRACT

PREDICTION OF DRAG FORCE ON GIMBAL SYSTEM VIA BALANCE TECHNIQUE AND WAKE INTEGRATION METHOD

Yeşilyurt, Emrah
Ms., Mechanical Engineering Department, METU
Supervisor: Prof. Dr. Kahraman Albayrak
January 2014, 153 pages

This thesis study examines the drag force exerted on a mini gimbal system through two methods of drag prediction. Wind tunnel experiments are performed with the real gimbal model since it is small enough. Drag force is measured by the balance technique using a load-cell, consisting of a metal beam and strain gauges adhered to it, which is designed and produced. For various Reynolds numbers drag force exerted on the model is measured. Results are essential since there is a restricted literature about it due to its military feature. Also drag force is estimated for various Reynolds numbers by wake integration method which is based on the conservation of linear momentum over a control volume and related measurements in the wind tunnel. Results obtained by two methods are compared and discussed for optimum selection of the control volume for the second method used. Furthermore, flow over the gimbal is examined and some flow visuals are obtained in a qualitative manner.

Keywords: Flow over immersed bodies, drag force, load-cell, strain gauge, control volume analysis, wake integration.

ÖZ

GİMBAL SİSTEMİ ÜZERİNDE OLUŞAN SÜRÜKLEME KUVVETİNİN BALANS TEKNİĞİ VE ART İZ BİRLEŞTİRME YÖNTEMİYLE ELDE EDİLMESİ

Yeşilyurt, Emrah
Yüksek Lisans, Makina Mühendisliği Bölümü, ODTÜ
Tez Yöneticisi: Prof. Dr. Kahraman Albayrak
Ocak 2014, 153 sayfa

Bu tez çalışması mini gimbal sistemi üzerinde oluşan sürükleme kuvvetini farklı iki yöntem ile incelemektedir. Gerçek gimbal modeli yeterince küçük olduğu için gerçek model ile rüzgar tüneli testleri yapılmıştır. Sürükleme kuvveti balans tekniği kullanılarak ölçülmüştür. Bu amaçla metal çubuk ve üzerine yapıştırılan gerinim ölçerlerden oluşan yük hücresi tasarlanmıştır ve üretilmiştir. Model üzeinde etki eden sürükleme kuvveti farklı Reynolds sayıları için ölçülmüştür. Askeri kullanım özelliğinden dolayı hakkında literatürde kısıtlı çalışma bulunan sistem için önemli sonuçlar elde edilmiştir. Ayrıca sürükleme kuvveti doğrusal momentumun korunumu ve bununla alakalı bazı ölçümleri içeren farklı bir yöntem kullanılarak farklı Reynolds sayıları için tahmin edilmiştir. Her iki yöntem ile bulunan sonuçlar karşılaştırılıp irdelenerek ikinci method için en uygun kontrol hacmi belirleme çalışmaları yapılmıştır. Ayrıca gimbal modeli üzerindeki akış deneysel olarak incelenmiştir ve bazı nitel akış görselleri elde edilmiştir.

Anahtar Kelimeler: Batık cisimler etrafında akış, sürükleme kuvveti, yük hücresi, gerinim ölçer, kontrol hacim analizi, art iz birleştirme yöntemi (entegral momentum)

To my mother.

ACKNOWLEDGMENTS

The author wishes to express his appreciation to his supervisor Prof. Dr. Kahraman Albayrak who guided and encouraged the author during the thesis study. His advises and discipline were very significant for the author and contribute the author's work very much.

The author wishes to express his deepest gratitude and love to his deceased mother, Leyla Yeşilyurt, who was a retired educationist. The author lost her few weeks before his first thesis defense in September 2013. The author dedicates this thesis to his mother who was the most incentive person for the master study of the author.

The author would like to thank his engaged Serra Okur and his family; his father Selçuk Yeşilyurt, his brother Saygın Yeşilyurt and sister-in-law Mürüvvet Yeşilyurt for their endless love and supports.

The author also would like to thank his dear friends, primarily Gülsüm Çaylan who helps the author in wind tunnel experiments for her great support and suggestions, Uğur Erdem Güzel, Selçuk Öksüz, Semih Çakıl and his colleagues from Aselsan Inc. for their valuable supports.

The author acknowledges Ulusal Makina Ltd. Şti. and Nejat Ulusal for load-cell production and support and also Bias Engineering and Şükrü Özen for his technical support.

The author also thanks İlhan Öztürk who works in the wind tunnel with another test section, Rahmi Ercan and Mehmet Özçiftçi for their technical support and work who are technicians of Fluid Mechanics Laboratory of Mechanical Engineering Department in METU.

TABLE OF CONTENTS

LIST OF TABLES

TABLES

LIST OF FIGURES

FIGURES

LIST OF SYMBOLS

A : Area

$A_{frontal}$: Frontal area

C_d : Drag coefficient

C_l : Lift coefficient

D : Drag force

D_p : Pressure drag

D_v : Vortex drag

F : Force

h : Enthalpy

H : Head of a fluid

L : Lift force

M : Moment

$\vec{n}$: Unit normal vector

p : Pressure

P : Power

R : Reaction force

Re : Reynolds number

s : Entropy

S : Side force

S_b : Surface of body

T : Temperature

u : x component of the velocity

U_∞ : Free stream velocity

v : y component of the velocity

$\vec{V}$: Velocity vector

w : z component of the velocity

Greek Letters

ε : Strain

μ : Absolute viscosity

τ : Shear stress tensor

τ_w : Wall shear stress

ρ : Density

ω : Vorticity

Abbreviations

CV : Control volume

GF : Gauge factor

LDA : Laser Doopler anemometry

UAV : Unmanned aerial vehicle

Subscripts

e : Exit

i : Inlet

S : Control surface

t : Total

W : Wake region

∞ : Free stream

CHAPTER 1

INTRODUCTION

In recent days unmanned aerospace or aerial vehicles (UAV) are very popular. They have been expanding all over the world as the technological developments arise. Many people have a great interest on these vehicles as a hobby seriously. Some of them can have a capability of assembling and disassembling parts of them, even modifying them self styled and making them from the rough. Since access to the desired information is easy and practicable, the number of such people increases. Nowadays universities are also active about UAVs. Especially, in some engineering departments of universities, students work on these systems and deal with designing and prototyping. This is a significant step for development of UAVs and it progresses rapidly. Despite commercial trend on UAVs, the main utilization purpose and area of these devices bases on military applications. Actually, this situation is the main factor related to professional development of UAVs. Hence, they are designed according to military standards.

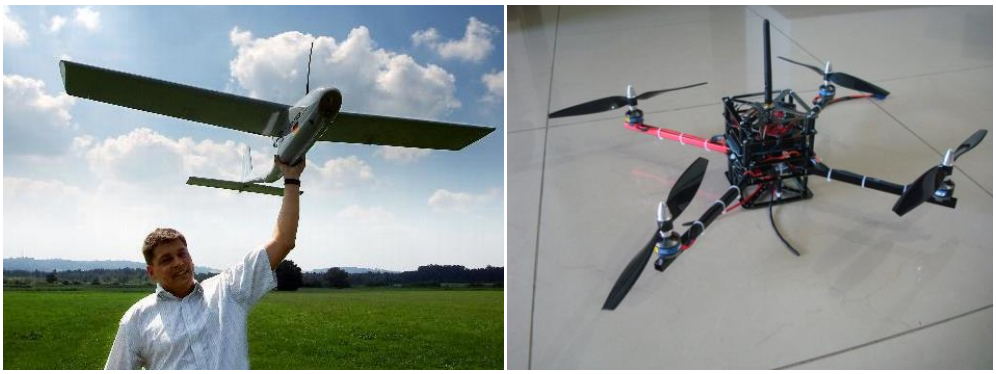

Figure 1.1: Examples of some commercial UAVs [1] [2]

UAVs can be classified and divided into many sub-categories according to range, wingspan, definition of its mission, etc. Main aim of the UAV usage is to carry out a specified task. Therefore, a typical UAV carries a payload or payloads. Examples of payloads are weapons, radar systems, surveillance systems etc. Examples can be propagated. Nevertheless, it is a common sense that A UAV must have a payload which is generally a gimbal system having electro optic systems, mostly a day-TV camera or a thermal imager, in it. Actually gimbal systems are the most common payloads used in UAVs. Generally when it performs its task, surveillance is the most important part of its mission.

Figure 1.2: Typical UAV used for military application [3]

Actually gimbal as a word has a definite meaning. It means a pivoted support that allows rotation of an object about an axis. But, it is a general word used for systems having two or more axis of revolution, actually general name of structure of this type of mechanisms. In this study, gimbal is referring to camera system containing the structure above mentioned. A gimbal system used in UAVs usually has a two degree of freedom. It means that it is able to have a rotation about two different axes. As a sensor unit it can often have a thermal imager or imagers operating in different wavelengths, a day-tv camera and extenders if necessary, laser range finder, laser

designator, simple pointer, also rarely ground positioning system (GPS) and digital magnetic compass (DMC). It can have all of the units in the same system as well as it can have only one of them. It differs according to application field and necessities. It can be used in terrestrial and naval applications in addition to aerial applications. Gimbal system shown in Figure 1.3 is significant in terms of giving an opinion related to these systems. Most probably it is a relatively big payload having nearly 15-20” diameter and it has a thermal imager, a day-tv imager and different types of laser systems.

Figure 1.3: Example of a gimbal system [4]

In this study, work on mini UAV gimbal systems is the main subject. Mini UAVs are smaller versions having a weight range of 2-20 kg. Dimensions of them are relatively small, for example the average length of wingspan is 3-5 m. Therefore, payloads of them have relatively small dimensional weight characteristics. A mini gimbal generally has either a thermal imager or a day-tv camera with an assistant sensor which can be a laser pointer for example. Gimbal system used in this work is a mini one and it has a thermal imager and a laser pointer. It can also have a day-tv camera instead of the thermal imager with in a minute since a modular structure is applied to its design. Modularity was the basic concern for its design.

Figure 1.4: Prototype of the mini gimbal

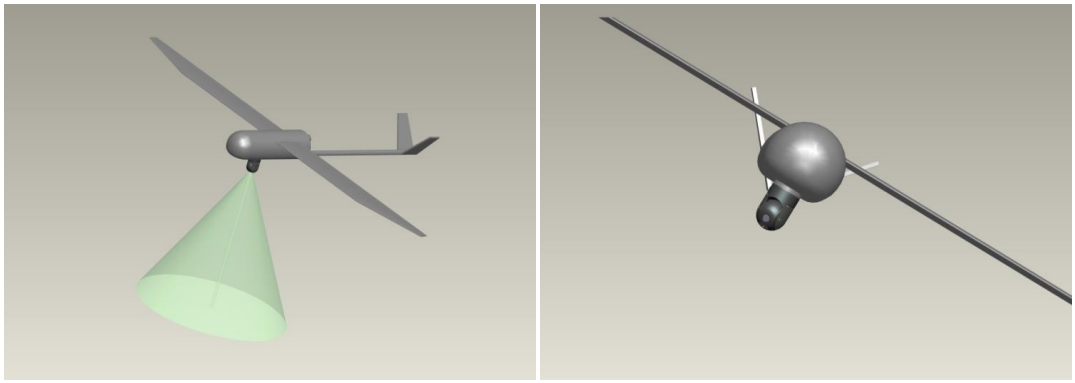

Figure 1.5: 3D model of mini gimbal assembled on a UAV

For a good quality of vision gimbal system must have a very well stabilized characteristics. These are actually high-end products and stabilization is a significant capability of them. Stabilization of these systems can be done electronically by image processing algorithms and mechanically by gyros. Even though these stabilization systems are used, they may not be sufficient every time because of the flow characteristics around gimbal system. Therefore, in addition to UAVs, gimbals

also must be designed to obtain good aerodynamic characteristics. Flight characteristics of UAVs can change from system to system. Also when mission goes on, flow characteristics around the gimbal can change as the position and the velocity of the system changes. Since it may encounter various flow structures, corruptions and interruptions of vision will be inevitable when it is in operation. Although stabilization exists in the system, it may not be sufficient every time. Stabilization quality of the system will decrease dramatically.

It can be said that at point that gimbal system can be considered as an immersed body in aerodynamics. Flow around it and its consequences can be seen as an area of interest in aerodynamics. Aim of this study is the examination of drag forces exerted on mini UAV gimbal systems. In fact, drag is the one of the most famous concepts of fluid mechanics and aerodynamics that has been studied and investigated over many years by several scientists and aerodynamicist. Year by year it could be seen that there have been progress about the topic parallel to developments of technology providing researches and experiments to be done in much professional and improvable manner. Within this context, it is possible to have so many studies and researches.

CHAPTER 2

LITERATURE SURVEY

Drag is a very wide phenomenon of the aerodynamics. Owing to its complexity and wideness of the concept, there have been many sub-topics related to the drag concept that requires literatures distinctively. Being narrowed down in the concept is a must and gives relevant viewpoints for the thesis study that have been conducted so far.

It can be easily predicted that the drag topic has been investigated for many years, actually more deeply since the beginning of modern aerodynamics, and many developments have been achieved in terms of understanding the physic behind it and finding methods that can be used for calculations and predictions of drag in a much more convenient manner. Wake integration method is one of these methods, that is combined with the wind tunnel experiments and measurements and it gives a useful step for this study.

Wake integral theory was first idealized and utilized by German physicist A.Betz [5] in 1925. Actually wake integration is a method for obtaining and determining drag forces acting on a body in free flight. Betz started with expressing Navier-Stokes equations simply for a region, which is control volume identified by him including the model in wind tunnel. After a series of steps and several assumptions, drag force was expressed by the combination of the wake integral and surface integral over the control volume selected. Wake integral part of his drag force expression was introduced by him as the profile drag component and the other part was identified as the induced drag. Integrating determination of the profile drag generated by Betz expression with experimental measurements in the wind tunnel was appropriate and

required less effort due to the fact that measurements only in the vortical wake region were necessary. On the other hand, the induced drag occurred in lifting bodies was the expression of surface integrals of upstream and downstream planes containing the kinetic energy with the transverse velocity components at these planes. According to theory of Betz for the induced drag, it was not easy to determine the induced drag combined with the experimental measurements since this part of his drag force expression was bringing out some experimental problems in accuracy and time owing to necessity of measurement of transverse velocity components over a wide region containing upstream and downstream planes and planes far from the vortical wake region. Also these velocity components were very small compared with the axial component and this caused another difficulty for measurements and was an obstacle for good accuracy. Difficulties enhanced in the determination of the induced drag could be regarded as the weak part of his theory; however, Betz theory was base of the wake integral method for drag prediction and gives physical insight about the drag force and its components acting on a body.

Further development on Betz theory was introduced by E.C Maskell [6] in 1973. It was actually originated from Betz formulation. Maskell dealt with the induced drag term of the drag expression of Betz. Wake integral form of the induced drag term was obtained by Maskell with an additional term. He also expressed the velocity correction terms related with wind tunnel walls placed in the profile drag formulation of Betz as wake integrals and defined a new velocity related to that part. Vortex drag expression was used instead of induced drag by him.

Wu et al [7] conducted a study about wake integral approach for drag determination in three dimensional flows. It was an explanatory study for understanding formulations of Betz and Maskell. They explained methods and formulations with assumptions and certain circumstances considered. They also conducted an experimental study and took measurements in the wake plane. They revealed that the induced drag could be evaluated with good accuracy with these measurements for an aircraft model.

Wu [8] conducted a study related to the wake integral method for the induced drag. It was a further research that was the development of studies of Betz and Maskell about the induced drag formulation. It was defined by him as the sum of two integrals standing for the axial vorticity and the transverse vorticity. The axial component of vorticity was represented as the wake integral and the transverse component, on the contrary, was expressed with an integral over the entire cross section of the wind tunnel. Actually, they were formulated separately and in case of relatively small transverse vorticity, measurements only in the wake plane would be sufficient for the determination of the drag.

Van Dam [9] mentioned alternative methods for determining the drag force. Wake integral method and following works by other scientists based on this method were summarized. By expressing the conservation of momentum equations over a control volume having a body in terms of the gradients and using second law of thermodynamics, the drag was resolved. Kusunose [10] did some scientific work about drag prediction and by identifying flow variables with small perturbations in incompressible wake region and using thermodynamics, the drag force was decomposed. Works of [9] and [10] evaluated the drag in similar manner. Enthalpy and entropy contributions to profile and induced drag terms were denoted. Another similar work was conducted by van der Wooren [11]. Aircraft model was used in wind tunnel tests and wake surveys with discussing compressible flow in addition to incompressible flow.

The paper of Giles and Cummings [12] was about wake integration for three dimensional flow. Analytical, experimental and computational views of the determination of the drag force of an aircraft in flight were examined. Drag was expressed as an integral over a crossflow plane selected arbitrarily behind the aircraft by using conservation of momentum approach and then it was decomposed according to vorticity, entropy and enthalpy variations as [9] and [10]. It was taken into consideration that whether analysis of the aircraft would be done with powered

engines or not. Connection with the lifting line theory and CFD applications were also examined in the study.

Examples of literature related to the wake integration can be enlarged. On the other hand, some of wind tunnel works can also help this study because experimental work will be conducted. Actually there is not enough literature about this topic related to experiments and test facilities due to the fact that gimbals are usually used in defense sector, and firms and incorporations dealing with these designs do not share their information conceived as trade secret. However, some researches and studies about flow around bodies and drag force concept can be used as a literature since gimbal is also an immersed body and rules of aerodynamics are valid for it.

Son et al. [13] conducted an article about free-stream turbulence effects over a sphere. With different turbulent intensities drag and lift coefficients and pressure distributions were obtained via the constructed experimental set-up. A load-cell, called CASS BCL-1L, was directly used for the drag measurement of the sphere. Drag coefficient was also obtained from the integration of the surface pressure measurements and compared with the direct measurement by the load-cell. In Figure 2.1, basics of their set-up can be seen.

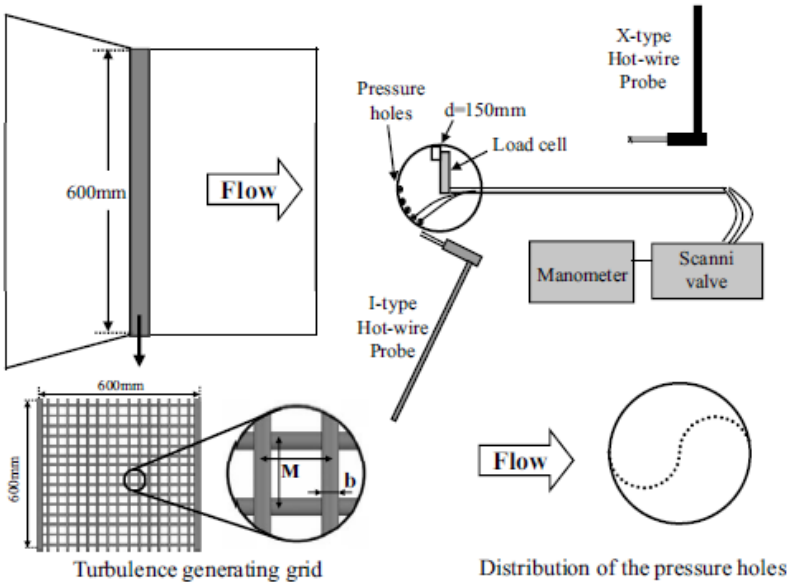

Figure 2.1: General view of test set-up of Son et al. [13]

Another work with wind tunnel was conducted by Tamura and Miyagi [14]. Their aim was to see the effects of turbulence on aerodynamic forces acting on a square cylinder. They also examined various corner shapes experimentally. Aerodynamic forces were measured with a 3 component load cell. For simulating 2D flow conditions and separating the model from the boundary layer of wind tunnel walls they decided to install end plates with elliptical leading edges at the top and bottom of the model. For 3D model tests, only up plate was removed and experiments were repeated. Turbulence level was adjusted by grids which can be seen on Figure 2.2.

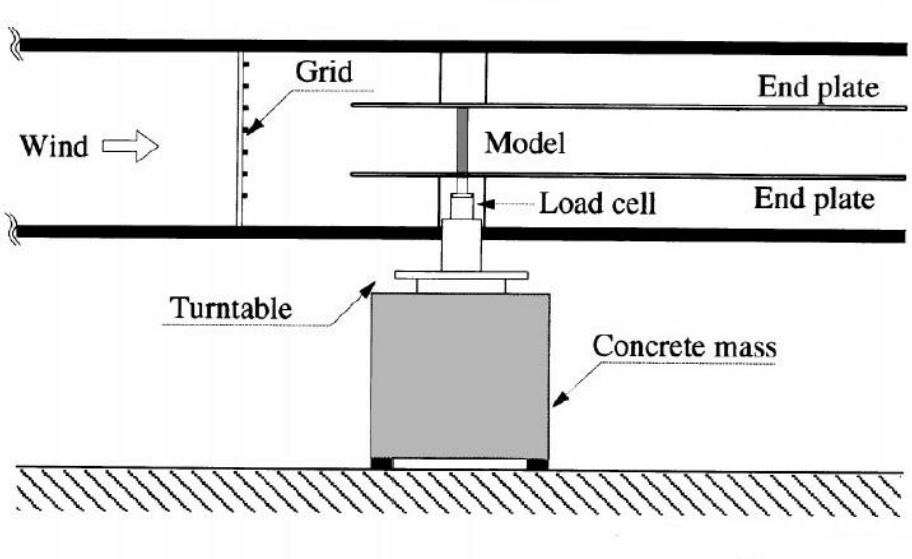

Figure 2.2: Test section of Tamura and Miyagi [14]

Suhariyono et al. [15] worked on a balance and measurement system for testing micro aerial vehicles. Generally micro aerial vehicles, operating at relatively low Reynolds numbers, have a wingspan of 100-150 mm and can be regarded as small vehicles. They designed a precision aerodynamic balance so as to measure lift and drag forces and rolling and pitching moments. It was analyzed with finite element methods and compared with calibration results.

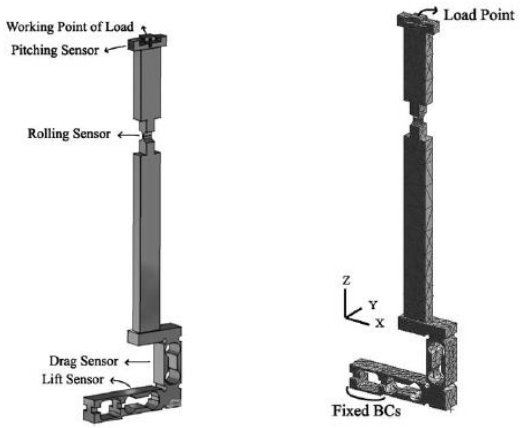

Figure 2.3: Designed balance system by Suhariyono et al. [15]

The balance system, made from aluminum, had sensors of strain gauges constructed in a full-bridge configuration to detect extremely small changes of measured forces and moments. Limit of the balance for the forces was ±10 N and for the moments was ±50 Nmm and they had a sensitivity of 0.1% of maximum load. Tests were conducted at an open wind tunnel and it was stated that the maximum blockage ratio was nearly 5% with the full model of micro aerial vehicle with 150 mm wingspan.

Sun et al. [16] developed a small aerial vehicle as a prototype and tested it in wind tunnel and water tunnel. In the open return low-speed wind tunnel airframe models in triangle and square wing planforms related to their vehicle were tested in order to examine the lift and drag coefficients. The load cell, Kistler Model 9251A, was used to measure drag and lift forces which was stated as the three-component quartz piezoelectric load cell. It was well isolated from the wind tunnel that could affect measurements of forces with vibration of it. By the use of a charge amplifier signal of the load cell was amplified to proportional voltage value which was utilized to interpret physical forces. Calibration was processed with the calibration rod and weight of 1 kg which was mounted on the calibration rod and producing moment on load cell could be used.

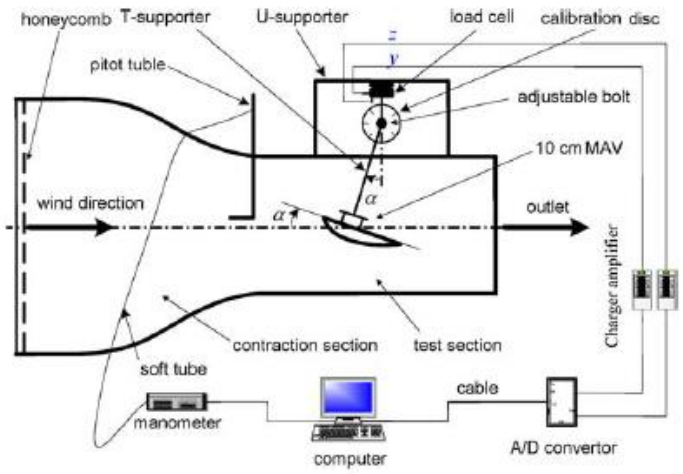

Figure 2.4: Schematic of wind tunnel tests of Sun et al. [16]

They also studied on water tunnel tests so as to examine the vortex and the turbulence creation of airfoil. After the wind tunnel and water tunnel tests, the developed vehicle was prototyped and the first prototype was tested in real flight conditions successfully. Test section used in wind tunnel tests and experimental set-up and their flow chart can be seen in Figure 2.4.

Almeida et al. [17] dealt with the wind tunnel testing. They aimed to measure dynamic forces in wind tunnel testing. Tested model was a bridge deck which was suspended by helical springs. Utilization of ring strain sensors was the method for measuring dynamic forces. In the Figure 2.5, the model tested in wind tunnel, shaft and suspension arms, helical springs, drag wires and ring strain sensors can be seen as (1), (2), (3), (4) and (5-6) respectively.

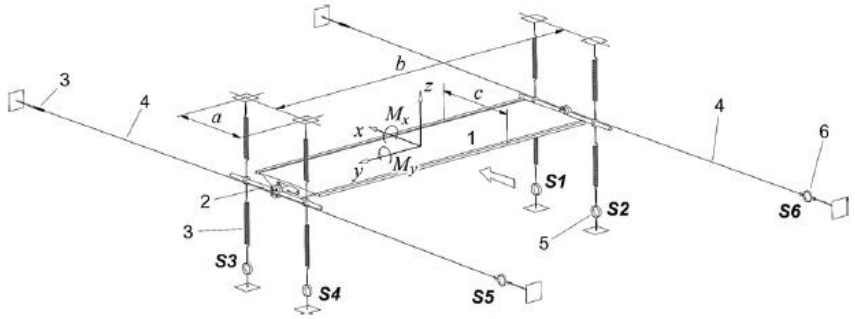

Figure 2.5: Force balance with strain ring sensors [17]

A full Wheatstone bridge circuit was configured with well located strain gauges which must have high sensitivity for this type of application to detect the change of strain. Places of strain gauges were determined to have max strains at stuck locations on rings which were made of brass. For measuring lift and drag forces, two types of rings were built and can be seen in Figure 2.6. S1, S2, S3 and S4 were same types and used for measuring the lift force and moment caused by flow. On the other hand,

S5 and S6 were identical and the drag force acting on the model was detected by means of them.

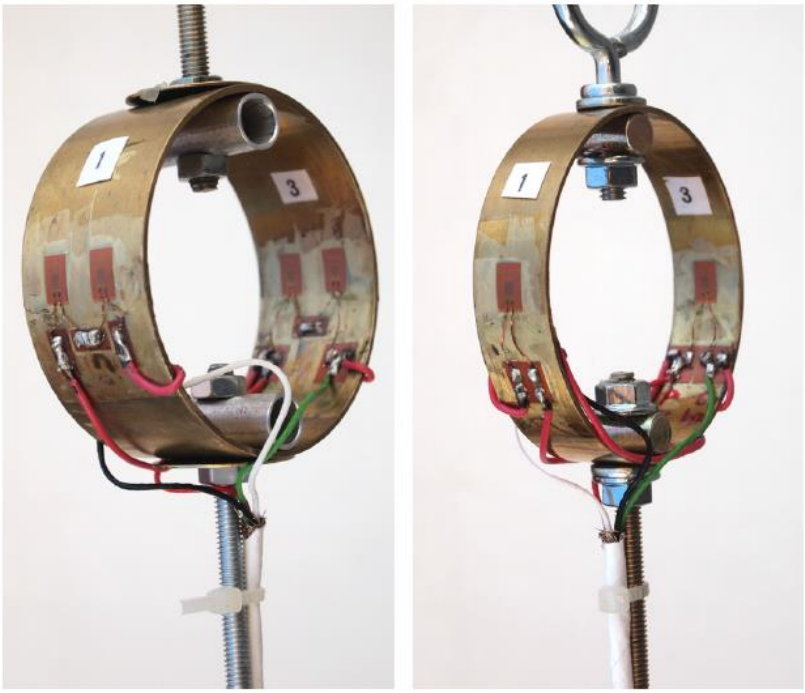

Figure 2.6: Strain ring sensors [17]

CHAPTER 3

THEORY

Flows around several different bodies have been examined for decades. This concept constitutes an essential part of fluid mechanics, aerodynamics. Actually aerodynamics is very curious about objects which are moving and have an interaction with any fluid.

When dealt with any immersed bodies, some concepts of aerodynamic become more of an issue.

3.1 Drag and Lift Forces

Fluid exerts a resultant force on an immersed body in it due to the interaction between the body and the fluid surrounding it. As a result of fluid flow over a body, some forces and moments are formed. In literature these can be mentioned as drag, lift and side forces and yaw, pitch and roll moments. Drag and lift forces are the most known and significant ones since they have critical affects on aerodynamic designs. For instance, an airfoil of an aircraft must experience drag force as less as possible and have a good lift characteristic. Also a car design must have a less drag. On the other hand, a parachute does need a relatively high drag coefficient and force to have better performance for its usage.

To get basic information about how lift and drag forces form, a small element can be taken as seen Figure 3.1. Then, force on this element can be written as:

$$dF_x = (pdA)cos\theta + (\tau_w dA)sin\theta \quad (3.1)$$

$$dF_y = (-pdA)sin\theta + (\tau_w dA)cos\theta \quad (3.2)$$

where p is the pressure and τ_w is the wall shear stress.

For this small element by integrating above equations drag and lift forces, respectively, can be written basicly as:

$$D = \int pcos\theta dA + \int \tau_w sin\theta dA \quad (3.3)$$

$$L = -\int psin\theta dA + \int \tau_w cos\theta dA \quad (3.4)$$

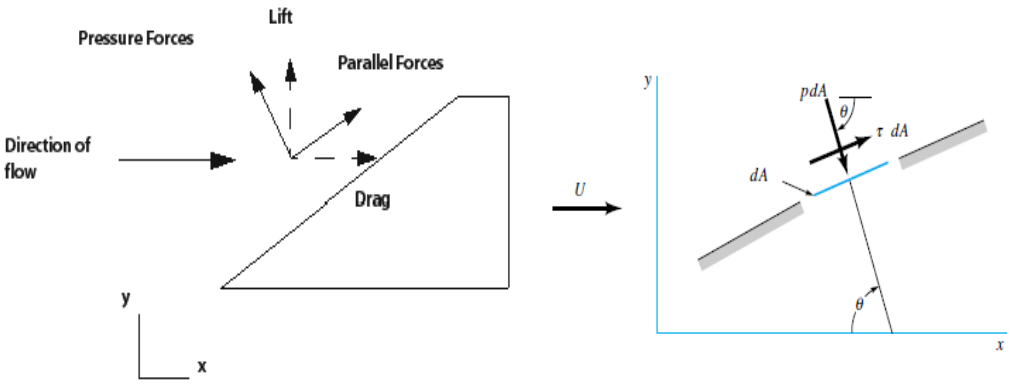

Figure 3.1: Decomposition of the aerodynamic force

In above equations one must have pressure and wall shear stress distribution on an immersed body to calculate lift and drag forces. Most of the time, these distributions, especially, wall shear stress distribution over a body, are not easily determined or predicted analytically or experimentally. Therefore, experiments in wind tunnels are

the essential part of the getting information about drag and lift forces. This situation comes out with dimensionless coefficients of those forces, drag and lift coefficients obtained more easily and simply. These non-dimensional coefficients are stated as [18] [19] [20]:

$$C_d = \frac{D}{0.5\rho {U_\infty}^2 A} \tag{3.5}$$

$$C_l = \frac{L}{0.5\rho {U_\infty}^2 A} \tag{3.6}$$

where D and L are drag and lift forces respectively, ρ is the density of the fluid, U_∞ is free stream velocity and A is the planform area which must be interpreted according to drag and lift forces separately.

3.1.1 Drag Force

When a body is in a motion in a fluid media, it experiences drag force which is a net force parallel to the flow, actually in the direction of the flow, owing to normal forces due to pressure and tangential forces due to skin friction forces causing shear stress as discussed above. Actually we can divide the drag force into two basic parts, pressure (form) drag and friction drag.

Several factors affect the drag. Shape and surface roughness of the body, and also non-dimensional parameters which are Reynolds number, Mach number, Froude number have responsibilities on drag coefficient.

Significant portion of the drag of most airplanes and most vehicles travelling through the atmosphere is directly related with the skin friction drag owing to shear stresses at the surface. In addition to skin friction, pressure (form) drag is the part of the drag steaming from pressure and its distribution on the body.

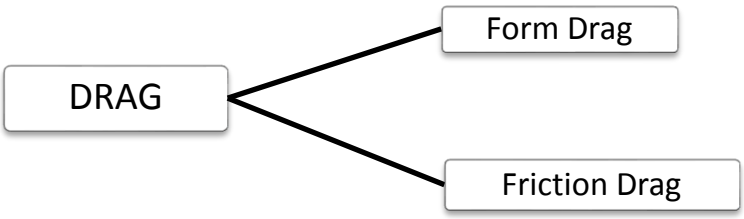

Figure 3.2: Simple drag classification

According to inviscid theory in which viscosity of the fluid is not considered, a body which moves in a fluid experiences no drag. In such a body, pressure distribution will be same for the up and bottom surfaces then there is no net force due to pressure since they will cancel each other. In Figure 3.3, a uniform cylinder in a potential flow can be seen. Pressure and velocity distribution are same for upper and bottom hemispheres and also body is highly well streamlined [18] [20].

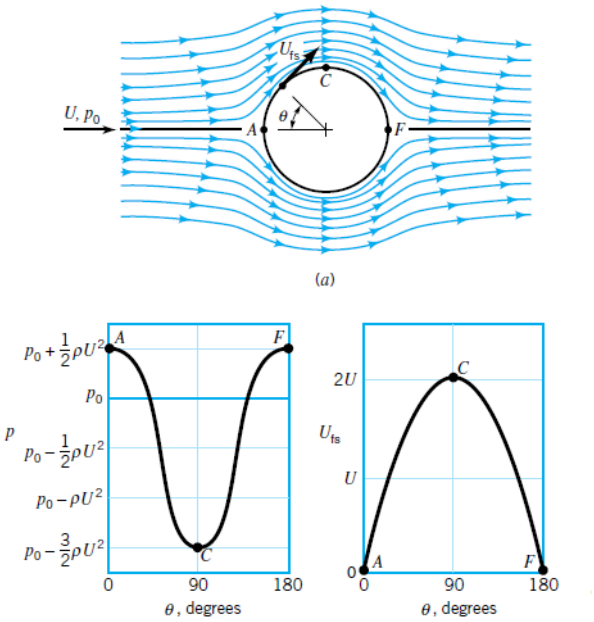

Figure 3.3: Inviscid flow over a cylinder [20]

However, actually the body must experience a drag force anyway (D'alembert paradox). In the presence of viscosity, boundary layer has been developed. Viscosity affects the pressure distribution on a body and as a consequence pressure drag occurs. It also has called as form drag since this type of drag has a big dependency to shape of a body. Pressure drag is mostly experienced and dominant component of drag for flows that the boundary layer separation is observed.

Actually type of drag has a relation with orientation of bodies. For example, a flat plate with a 0° angle of attack experiences skin friction drag mainly. Pressure forces on the surface of the flat plate will be normal to flow direction and in this case any contribution of pressure to the drag force cannot be mentioned. When the angle of attack is increased, pressure forces have an effect in the direction of flow and start to make contributions to total drag. When the angle of attack of the flat plate is 90°, flat plate is normal to flow, all drag is the consequence of pressure forces.

In Figure 3.4, trade-off between the friction and form drag in an airfoil-like shaped body can be seen. It can be interpreted that shape of bodies and their slenderness ratio affect drag type experienced on it directly.

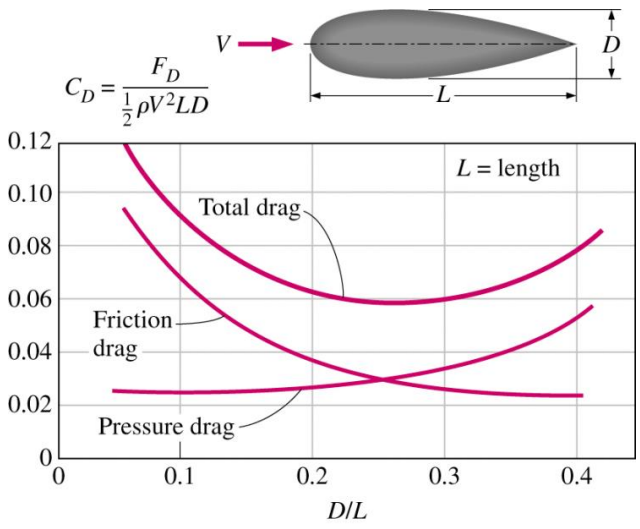

Figure 3.4: Relation between friction and pressure drag [21]

3.2 Wake Integral Formulation for Determining Drag Force

Two different perspectives and techniques are used basically for determining drag on bodies in integral form. Total force on a body in fluid flow can be written as [9] [10] [12]:

$$\overrightarrow{F_t} = \int_{S_b} (-p\vec{n} + \tau : \vec{n})\, dS_b \tag{3.7}$$

where S_b is the surface of the body, p stands for pressure, τ denotes the shear stress tensor, $\vec{n}$ is the outward unit normal vector to the surface of the body.

$$\tau = \begin{bmatrix} \tau_{xx} & \tau_{xy} & \tau_{xz} \\ \tau_{yx} & \tau_{yy} & \tau_{yz} \\ \tau_{zx} & \tau_{zy} & \tau_{zz} \end{bmatrix} \tag{3.8}$$

$$\vec{n} = n_x\vec{\imath} + n_y\vec{\jmath} + n_z\vec{k} \tag{3.9}$$

F_t is the total force exerted on the body by the fluid and contains also lift and side forces as well as drag force. This can be written for a right-handed Cartesian coordinate system as:

$$\overrightarrow{F_t} = D\vec{\imath} + S\vec{\jmath} + L\vec{k} \tag{3.10}$$

where D is the drag force which must be in the direction of the flow, S is the side, lateral, force and L is the lift force. Then drag force can be written more detailed as [9]:

$$D = \iint_{S_b} \left(-pn_x + \tau_{xx}n_x + \tau_{xy}n_y + \tau_{xz}n_z\right) dS_b \tag{3.11}$$

Above drag equation is known as “near-field” drag force expression [9] [10] [12]. It can be interpreted from body perspective since near-field drag force expression is the result and summation of the forces exerted on the body. This equation looks simple and explanatory. However, it is not sufficient to calculate drag forces for complex shapes and conditions as well. Calculating drag with this method can be time consuming due to hardness of the measurement of the shear stress distribution on the body surface.

The other view point for calculating the drag force is known as “far-field” method which can be derived from the conservation of linear momentum principle. For a fixed control volume surrounding a body with a steady uniform flow, the total force acting on the control volume can be written as:

$$\Sigma\vec{F} = \iint_S \rho\vec{V}(\vec{V}.\vec{n})dS \tag{3.12}$$

where ρ is the density of the fluid, V is the velocity vector of the flow, $\vec{V} = u\vec{\imath} + v\vec{\jmath} + w\vec{k}$, S is the control surface, $\vec{n}$ is the outward unit normal vector to the control surface S. The total force acting on the control volume can also be expressed as:

$$\Sigma F = \Sigma F_{surface} + \Sigma F_{ext} \tag{3.13}$$

where $\Sigma F_{surface}$ stands for the surface forces exerted on the control volume and its boundaries, ΣF_{ext} stands for gravity and electro-magnetic forces, also called body forces, acting on the fluid particles within the control volume [18] [19] [20]. Since there is no body force, it can be denoted that $\Sigma F_{ext} = 0$. Then the total force becomes:

$$\Sigma\vec{F} = \Sigma F_{surface} = \vec{R} + \iint_S -p\,\vec{n}\,dS + \iint_S \tau{:}\,\vec{n}\,dS \tag{3.14}$$

where R is the total reaction force exerted by the body in control volume on the fluid. Second term and third term stand for pressure forces and shear forces on the control surface respectively.

By using equation (3.13) and (3.14),

$$\vec{R} + \iint_S -p\,\vec{n}\,dS + \iint_S \tau{:}\,\vec{n}\,dS = \iint_S \rho\vec{V}(\vec{V}.\vec{n})dS \tag{3.15}$$

$$\vec{R} = \iint_S [p\,\vec{n} + \rho\vec{V}(\vec{V}.\vec{n}) - \tau{:}\,\vec{n}]\,dS \tag{3.16}$$

As stated before, R is the total force generated on the fluid by the body in control volume. Therefore, the total force exerted on the body by the fluid equals to the total force acting on the body, R, with a minus sign. Thus, equation (3.16) becomes

$$-\vec{R} = \overrightarrow{F_t} = \iint_S [-p\,\vec{n} - \rho\vec{V}(\vec{V}.\vec{n}) + \tau{:}\,\vec{n}]\,dS \tag{3.17}$$

As it is seen, the difference between equation (3.7) and (3.17) is the momentum flux term, $\rho\vec{V}(\vec{V}.\vec{n})$. Actually both two equations are theoretically equivalent for computing total force on the body in a steady uniform flow.

With a help of equation (3.17), far-field drag expression can be written as

$$D = \iint_S [-p\,n_x - \rho u(\vec{V}.\vec{n}) + (\tau_{xx}n_x + \tau_{xy}n_y + \tau_{xz}n_z)]\,dS \tag{3.18}$$

It can be interpreted at this point that the far-field drag force expression cannot be easily handled. In fact, it does not have essential difference from the near field drag

expression about calculating drag in an easier manner since it still has shear stress terms. Also all surfaces of the control volume are included in the drag force expression. Hence, dealing with the far-field expression with current form is tedious and does not give deeper insight about the drag.

Certain assumptions are necessary for simplifying and making sense of the far-field expression. In Figure 3.5, control volume and surfaces surrounding a body, the right-handed Cartesian coordinate system and free stream velocity are demonstrated. It is convenient to make the assumption that the control volume and surfaces are selected far enough from the body and thus flow has same characteristics as free stream, $U_\infty, p_\infty, \rho_\infty$, at four side surfaces of control volume parallel to free stream. This provides no momentum flux through these side surfaces and they can be omitted for the evaluation of wake integral. Another assumption is neglecting the viscous stresses by choosing the control volume away enough from the body. At far enough downstream, they can be ignored.

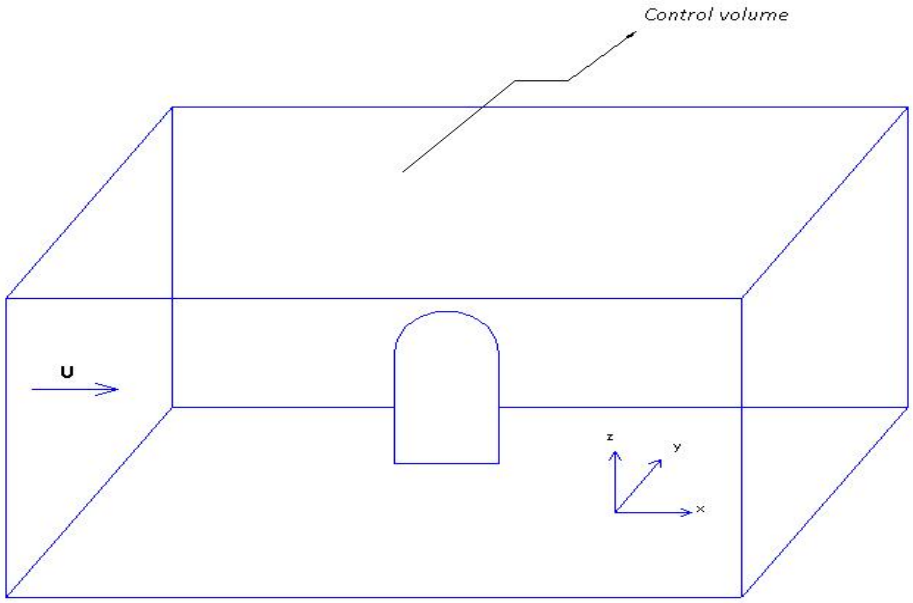

Figure 3.5: Control volume surrounding a body

After applying these assumptions, equation (3.18) comes to a state of:

$$D = -\iint_{S_{exit}} [(p - p_\infty) + (\rho u^2 - \rho_\infty U_\infty^2)]\, dy\, dz \tag{3.19}$$

By using conservation of mass;

$$\iint_{S_{inlet}} \rho_\infty U_\infty \; dy\, dz = \iint_{S_{exit}} \rho u \; dy\, dz \tag{3.20}$$

Then the drag force expression changes to:

$$D = -\iint_{S_{exit}} [(p - p_\infty) + \rho u(u - U_\infty)]\, dy\, dz \tag{3.21}$$

This wake integral equation steaming from the far-field method is suitable for experimental methods and data. Applicability of the equation (3.21) is quite feasible compared with equation (3.7) and (3.17). All quantities in equation are measurable and interpretable. Also it has the advantage of taking data only in wake region which is the exit surface of the control volume. Calculations of integrals over only this region will be easier than calculation of the other integrals mentioned previously.
However, this form of wake integral equation was not thought as enough owing to its inadequacy for not providing more physical interpretation of understanding the drag sources. Therefore, some techniques were developed in order to realize the drag mechanisms.

Betz [5] was the first who introduced a method of wake integration for the determination of the drag force. He generalized the wake integral theory and resolved the drag force into two components, profile drag and induced drag, on lifting bodies.

He started to develop his formula with the continuity and Navier-Stokes equations for a steady viscous incompressible flow.

$$\nabla H + \mu \nabla x \vec{\omega} = \rho \vec{V} x \vec{\omega} \tag{3.22}$$

$$\nabla . \vec{V} = 0 \tag{3.23}$$

Equation (3.22) was integrated over a connected region R of the fluid. By the help of vector calculus, he could re-express the equation in boundary integrals [5].

$$\oiint_B H \vec{n} dB - \mu \oiint_B \vec{\omega} x \vec{n}\, ds = \rho \iiint_R \vec{V} x \vec{\omega} dR \tag{3.24}$$

where H is the total head of the fluid, $H = p + \rho V^2/2$, ρ is the density, μ is the absolute viscosity, $\vec{\omega}$ is the vorticity of the fluid. $\vec{n}$ is a unit normal vector outward from R. As shown in Figure 3.6, B is summing of the surfaces that two constant x planes, S_1 and S_2, and effective tunnel boundary between these two planes. S_s is the surface of the model between the two planes.

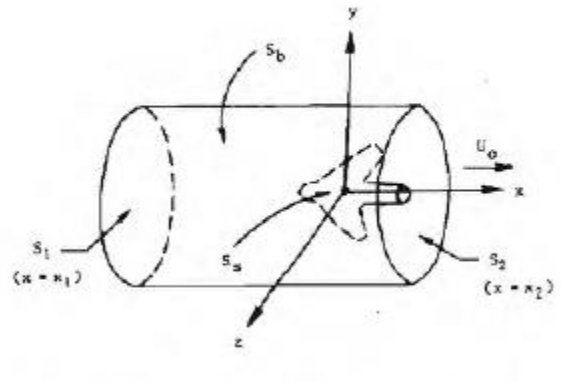

Figure 3.6: Definition of axes and integration surfaces in Betz formula [7]

It was stated that surface S_b has the undisturbed wind tunnel flow that, $\vec{\omega} = 0$ and $H = H_0$, the undisturbed wind tunnel stream total head. On the other hand, there

is a contribution of surfaces S_1 and S_2 to the left hand side of equation (3.24) By the help of (3.24), drag was given as [5]

$$D = \iint_{S_1} H\, dydz - \iint_{S_2} H\, dydz + \rho \iiint_R (v\zeta - w\eta) dR \tag{3.25}$$

where v and w are the components of velocity and η and ζ are y and z components of $\vec{\omega}$, respectively. Then the alternative form of drag steaming from equation (3.25) is as below.

$$D = \iint_{S_1} \left[H + \frac{1}{2}(u^2 - v^2 - w^2)\right] dydz$$
$$- \iint_{S_2} [H + \frac{1}{2}(u^2 - v^2 - w^2)]\, dydz \tag{3.26}$$

The above equation stands for the D acting on S_s and it is independent from the location of the model, it can be or cannot be between the locations x_1 and x_2 [5]. The complete derivation of it can be found in [5].

For the case of the model being between the locations x_1 and x_2, it was introduced a velocity magnitude as reference velocity in the undisturbed wind tunnel stream total head equation as

$$H_0 = \rho + \frac{1}{2}\left(u^{*2} + v^2 + w^2\right) \tag{3.27}$$

and it was given that $u^*=u$ at $x=x_2$ outside of vortical wake and at $x=x_1$. For the deviation of u^* from the undisturbed tunnel velocity u_0, u'' was defined as

$$u'' = u^* - u_0 \tag{3.28}$$

Then for using in wake integral a relation starts with $u^2 = u^2$ and adding and subtracting u^{*2},

$$u^2 = u^2 - u^{*2} + u^{*2} \tag{3.29}$$

By using definition of reference velocity:

$$u^2 = u^2 - u^{*2} + (u^{"} + u_0)^2 \tag{3.30}$$

$$u^2 = u^2 - u^{*2} + {u_0}^2 + 2u_0 u^{"} + {u^{"}}^2 \tag{3.31}$$

$$u^2 = u^2 - u^{*2} + {u_0}^2 + 2u_0(u^* - u_0) + {u^{"}}^2 \tag{3.32}$$

$$u^2 = u^2 - u^{*2} + {u_0}^2 + 2u_0 u^* - 2{u_0}^2 + {u^{"}}^2 \tag{3.33}$$

From conservation of mass, it can be obtained that

$$\iint_A (-2{u_0}^2)\, dydz = -2u_0 \iint_A u_0 dydz = -2u_0 \iint_A u dydz \tag{3.34}$$

where A stands for the effective cross-section of the tunnel.
By using (3.34), equation (3.33) was integrated [5] [6].

$$\iint_A u^2\, dydz = \iint_A (u - u^*)(u + u^* - 2u_0) dydz + \iint_A {u^{"}}^2 dydz + \iint_A {u_0}^2 dydz \tag{3.35}$$

The first integral in equation (3.35) was called as wake integral because u is not equal to reference velocity only in the vortical wake region. Therefore, for the first

integral, right hand side of equation (3.35), the integration region A turned to W which stands for the wake region [5] [6]. Using equation (3.35) inside equation (3.26) yields

$$D = \iint_W [(H_0 - H_2) + \frac{1}{2}\rho(u_2^* - u_2)(u_2^* + u_2 - 2u_0)]dydz + \frac{1}{2}\rho \iint_A [(v_2^2 + w_2^2) - (v_1^2 + w_1^2)]dydz - \frac{1}{2}\rho \iint_A \left(u"_2^2 - u"_1^2\right) dydz \quad (3.36)$$

with a note that $H \neq H_0$ only in the wake region.

As a total, equation (3.36) was first yielded by Maskell. The first integral in equation (3.36) was identified by Betz, the wake integral term, as the profile drag term acting on a body in an external flow. The sum of the form drag and the skin friction drag can be defined as the profile drag. The second integral in equation (3.36) was called as the induced or vortex drag by Betz. As conventionally defined, the induced drag is actually is the lift-induced drag which is the direct affect of the lift. It can be seen more commonly in airplanes due to their wing characteristics, actually steaming from wing tips and its vortices generally. The third integral term in equation (3.36) was first identified by Maskell, and it was the correction term for the flow which was occurred because of constraints placed on the flow by wind-tunnel walls and their effects [6] [8].

Equation (3.36) has good characteristics related to understanding of the physical reasons leading to the drag force and will have good impact on the drag reduction methods. But, it must be pointed out that interchanges between these three integral terms mentioned above can be possible due to location of measurement plane and the flow conditions [8].

Vortex drag and the correction term were also expressed as a wake integral by Maskell. He expressed the vortex drag as

$$D_v = \frac{1}{2}\rho \iint_W \psi\xi dydz + \frac{1}{2}\rho \iint_A (\phi_1\sigma_1 - \phi_2\sigma_2)dydz \tag{3.37}$$

where ξ is the x-component of vorticity and σ is defined as

$$\xi = \frac{\partial w}{\partial y} - \frac{\partial v}{\partial z} \tag{3.38}$$

$$\sigma = \frac{\partial v}{\partial y} + \frac{\partial w}{\partial z} = -\frac{\partial u}{\partial x} \tag{3.39}$$

and ψ and ϕ are scalar functions that satisfy the below equations and have the no-slip boundary conditions at the wind tunnel wall [6] [8].

$$-\xi = \frac{\partial^2 \psi}{\partial y^2} + \frac{\partial^2 \psi}{\partial y^2} \tag{3.40}$$

$$\sigma = \frac{\partial^2 \phi}{\partial y^2} + \frac{\partial^2 \phi}{\partial y^2} \tag{3.41}$$

If x_1 and x_2, upstream and downstream positions, are enough far from the model placed in control volume, thereby the wind tunnel, then σ_1 and σ_2 are negligible since u component of velocity cannot change at these locations, x_1 and x_2. However, being far enough from the model for x_1 and x_2 can be impractical to get measurements in the wind tunnel. Hence, it can be stated that σ_1 and σ_2 are not sufficiently small for being neglected, yet $\phi_1\sigma_1$ and $\phi_2\sigma_2$ are nearly equal that the difference of them is negligible [8]. In case of making one of these assumptions, second term in equation (3.37) can be neglected.

Then the correction term as wake integral is

$$\frac{1}{2}\rho \iint_A \left(u^{"2}{}_2 - u^{"2}{}_1 \right) dydz = -\rho u_b \iint_W (u_2^* - u_2) dydz \tag{3.42}$$

where u_b is a wake-blockage velocity defined by [6]

$$u_b = \frac{1}{2A} \iint_W (u_2^* - u_2) dydz \tag{3.43}$$

Thus all terms in equation (3.36) are seen that they could be written in wake integral forms. By doing further assumptions and neglecting of some terms especially according to upstream and downstream conditions related with the control volume selected, they come to a state of different forms that can be easily integrated with tests and measurements conducted in the wind tunnel. Complete derivations of (3.37), (3.42) and (3.43) can be found in [6].

Originated from work of Betz, Maskell, Hackett and Wu, the drag force is expressed by Giles and Cummings [12], Van Dam et al [9], Kusunose [10] with different ways and they contributed to interpretation of the drag sources and mechanisms from several viewpoints.

Equation (3.21) can be re-expressed in terms of gradient by combining the second law of the thermodynamics as equation (3.46) [9] [10] [12].

$$D = \frac{1}{2} \iint_{S_{exit}} (\vec{r}.\nabla)(p + \rho u^2)\, dS_{exit} \tag{3.44}$$

$$dp = \rho dh - \rho T ds \tag{3.45}$$

$$D = \frac{1}{2}\iint_{S_{exit}} [\vec{r}.(\rho\nabla\left(h + \frac{1}{2}V^2\right) - \rho T\nabla s - \frac{1}{2}\rho\nabla(v^2 + w^2 - u^2) + u^2\nabla\rho)]dS_{exit} \quad (3.46)$$

r is the position vector and free stream flow conditions are satisfied at the tip of the infinite plane [9]. Examining the equation (3.46) by some assumptions provides simplifying.

Equation (3.46) can be re-handled as

$$D = -\rho\iint_{S_{exit}} \Delta h_t dS_{exit} + \frac{p_\infty}{R}\iint_{S_{exit}} \Delta s dS_{exit} + \frac{\rho_\infty}{2}\iint_{S_{exit}} (\psi\xi)dS_{exit} \quad (3.47)$$

where $h_t = h + \frac{1}{2}V^2$, the total enthalpy, R is the gas constant, $\Delta h_t = h_t - h_{t_\infty}$ and $\Delta s = s - s_\infty$. Neglecting the higher order Δu terms in third term of equation (3.46), assuming ρ as a constant and using the relations of (3.40) and (3.41) from Maskell's vortex drag expression constitute the equation (3.47) [9] [10] [12].

There have been three integrals in equation (3.47). The first integral is related with the total enthalpy and can be neglected for the zero propulsion systems because of the fact that the flow can be regarded as steady and adiabatic that total enthalpy remains constant. Thus the drag equation consists of the second and third integrals which are associated with profile and induced drag respectively [9] [10] [12]. It is seen that non-isentropic process causes the profile drag. The reasons of non-isentropic process are given as boundary-layer flow actually frictional flow and flow with shock waves [18]. Therefore, the profile drag can be decomposed into viscous drag and wave drag. As mentioned, induced drag is a vortex drag arising from cross flows in the wake region directly related with the lift generation and continual shedding of vortices in three-dimensional flows [8] [12].

Then the total drag is decomposed as

$$D = D_{profile} + D_{induced}$$

$$= D_{viscous} + D_{wave} + D_{induced} \tag{3.48}$$

that was well accepted by [9] [10] [12] [22].

Another useful approach for the drag sources can be seen in Figure 3.7 which is parallel with the decomposition shown in equation (3.48) by Hendrickson et al [23].

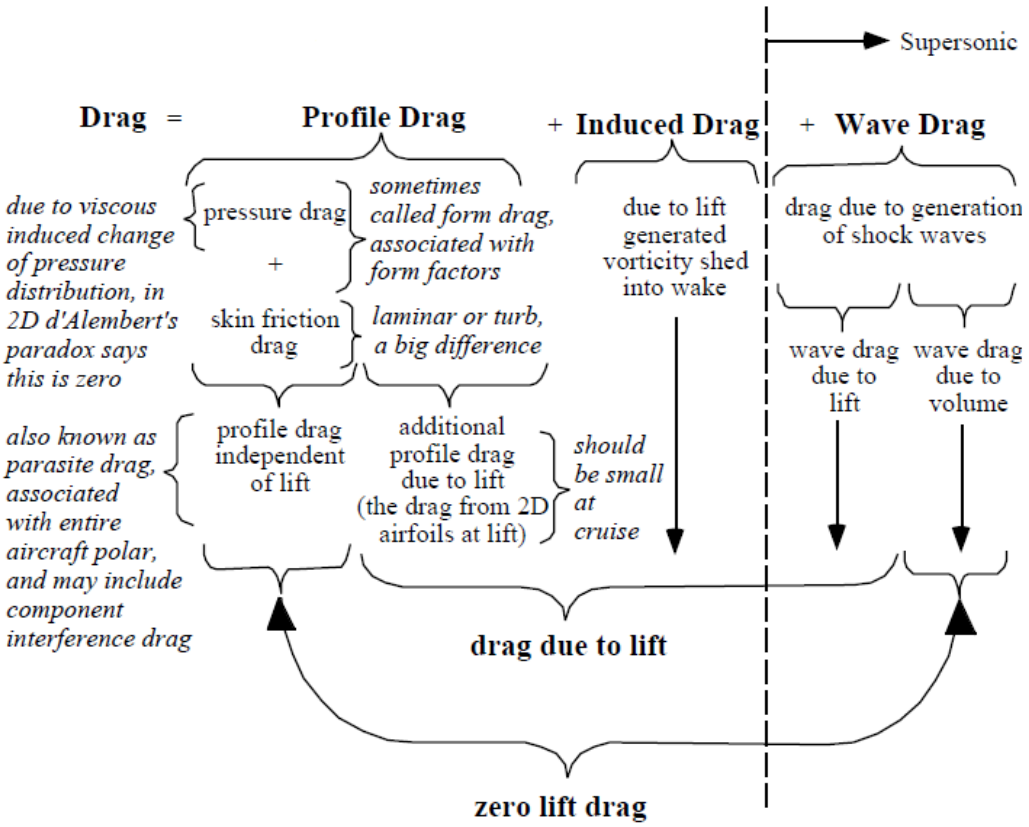

Figure 3.7: Categorization of drag [23]

In the near-field expressions, surface integrals of the model were used and the drag force on the model was expressed. With this method, the drag is mechanically decomposed as pressure (form) drag and viscous (friction) drag. On the other hand, in the far-field analysis, the drag force is re-expressed by wake integrals providing physical decomposition and more physical sense for understanding the drag sources.

$$\underbrace{D = D_{pressure} + D_{viscous}}_{mechanical\ decomposition} = \underbrace{D_{induced} + \overbrace{D_{viscous} + D_{wave}}}_{physical\ decomposition} \tag{3.49}$$

As a summary of the equation (3.49), Figure 3.8 can also be seen below.

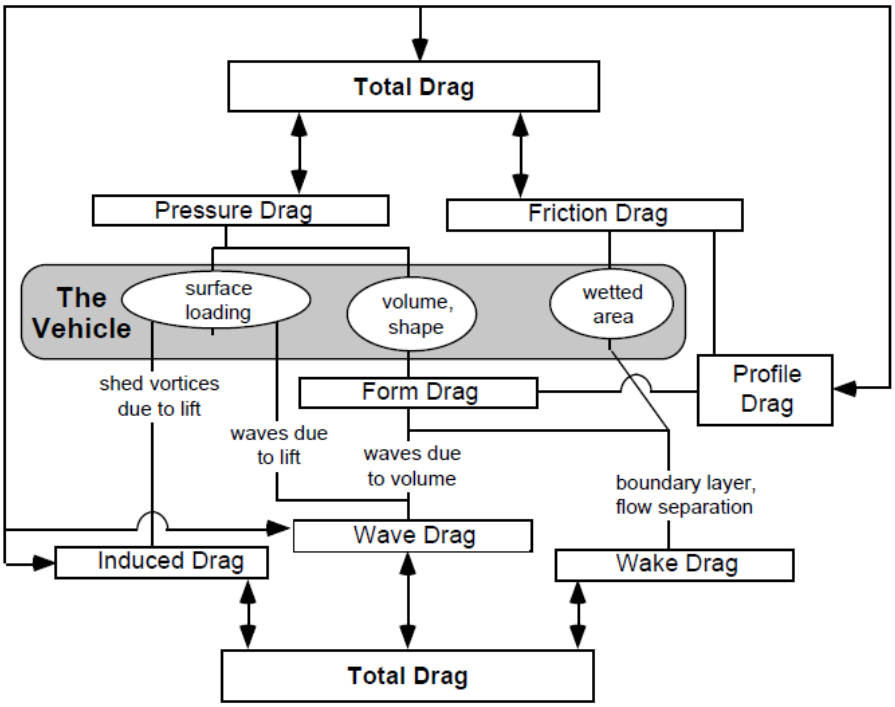

Figure 3.8: Further decomposition of the drag [23]

CHAPTER 4

EXPERIMENTAL SET-UP

Aerodynamic tests and experiments are the most crucial parts beside the theory and physics, in fact, value of tests and experiments causes us to gain very beneficial sense, which must not be underestimated, for understanding the theory and physics deeper. For investigating the drag characteristic of the gimbal, several experiments were planned.

Actually drag must be measured by means of a load-cell and to be able to apply the wake-integration method for estimating the drag in different way, series of pressure and velocity measurements were needed fundamentally. In order to maintain these planned experiments, some devices and designs in addition to model tested in the wind tunnel were utilized and experimental set-up was constituted.

4.1 Model Used in Wind Tunnel Tests

The main objective of experiments held in wind tunnel was testing some aerodynamic characteristics of the gimbal which was specifically designed for an identified aim.(Gimbal is general word used for this type of systems which have two or more axis of revolution, actually general name of structure of this type of mechanisms. In this study, gimbal is referring to camera system containing the structure above mentioned.) It can be stated that gimbal model used in wind tunnel experiments was not scaled version; in contrast, it was the real system, planning to be used in different types of UAV systems. Therefore, mechanical dimensions of the model used in experiments are real dimensions and there was no need for

underscaling and similitude analysis. Undoubtedly, this situation provided certain advantages for post studies of experiments.

Casing of the gimbal body was manufactured by plastic injection method. Hence, surface roughness value, Ra, is very low owing to manufacturing method and the model has very smooth surface which can be regarded as an advantage for experiments. Its shape can be defined as combination of circular cylinder and sphere. The model is shown in Figure 4.1. Also mechanical dimensions of it can be seen in Table 4.1.

Table 4. 1: Dimensional properties of model

Mechanical Dimensions of Model	
Diameter (ø)	120 mm
Length (L)	140 mm
Estimated frontal area	15250 mm^2

Figure 4.1: Model tested in experiments

4.2 Wind Tunnel

Planned experiments were carried out in the open return type wind tunnel located in Mechanical Engineering Department, in Middle East Technical University. Type of the wind tunnel can be also known as suction type wind tunnel. It is driven by an axial fan located at the end of the tunnel and it has normally contraction and diffuser sections in addition to test section and also turbulence and safety screen located before and after the test section respectively. Schematic view of the wind tunnel used is shown in Figure 4.2.

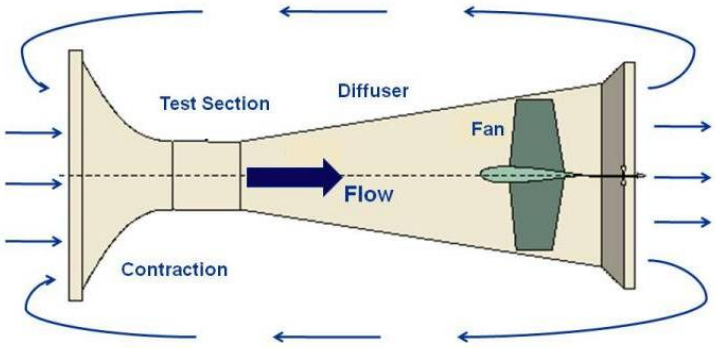

Figure 4.2: Schematic of wind tunnel

Sections of the wind tunnel are made from wood substantially. On the other hand, lateral walls of the test section of the wind tunnel are made of plexiglass allowing making observations regarding experiments and the flow and these lateral plexiglass wall parts can be easily removed and placed on, enabling the direct intervention to the test section and the model used in experiments when desired. Also small part of the upper wall, of the test section is made of plexiglass.

The axial fan providing the air flow has twelve blades and a diameter of more than one meter and it is driven by an AC electrical motor. The rotational speed of the axial flow fan is adjusted via the control panel located near the test section as an open loop

controller by the means of potentiometer and screen located in control panel which shows instantaneous percentage of its capacity and corresponding instantaneous rotational speed of the axial fan in rpm.

General characteristics of wind tunnel containing dimensions of test section are summarized in Table 4.2.

Table 4.2: Wind tunnel characteristics

Type	Horizontal, Open return, Suction type, Subsonic
Length of the test section	2410 mm
Width of the test section	750 mm
Height of the test section	500 mm
Area of the test section (approx.)	370000 mm^2
Maximum speed (estimated)	30 m/s
Turbulence Level	< 1%
Motor Power (max)	45 kW (60 hP)

Figure 4.3: General view of the wind tunnel

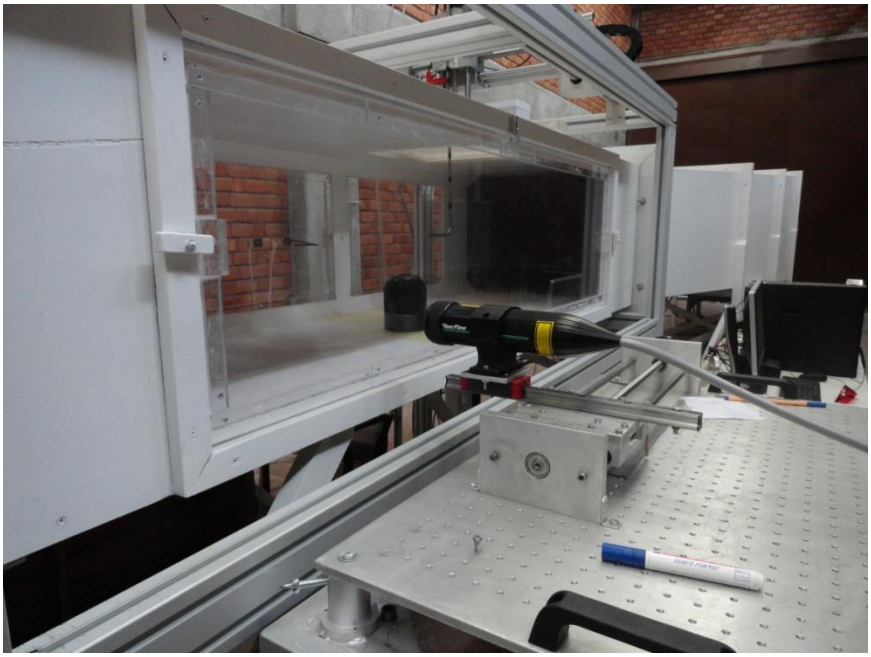

Figure 4.4: Test section

Figure 4.5: Control panel of wind tunnel

Figure 4.6: Indicator of control panel

4.3 Traverse Mechanism

A traverse mechanism designed and constructed in Mechanical Engineering Department latterly was used in wind tunnel experiments. It was used for another thesis study. The main task of the traverse mechanism is to reach desired points on the test section which can be defined by 3D Cartesian coordinate system. It contains screw mechanisms lying on x, y and z axes and has three degree of freedom via three DC electrical motor actuating the screw mechanisms of each axis independently. Movement range of the traverse in each axis is identified by two optical sensors located at the beginning and the end of each screw mechanism. Its control is provided by its control panel (Figure 4.8). Its motion starts by entering the desired x, y and z positions over control panel after self-initializing of the traverse system.

Figure 4.7: Traverse mechanism

Figure 4.8: Touch-operated control panel of the traverse mechanism

It is placed according to the test section actually since the plexiglass part of the upper wall of the test section has a sliding mechanism with a hole which allows motion in x, y and z axis when combined with the traverse mechanism. Multi-purpose holder made of delrin, a type of plastic, is designed and assembled to the z axis of traverse mechanism and it is used to hold pitot tube and cylindrical bar of the hot-wire probe during measurements. Usage of the traverse mechanism with its supporters above mentioned allows us to get measurements on desired cross sectional points of test section and with this facility wake surveys are able to be completed.

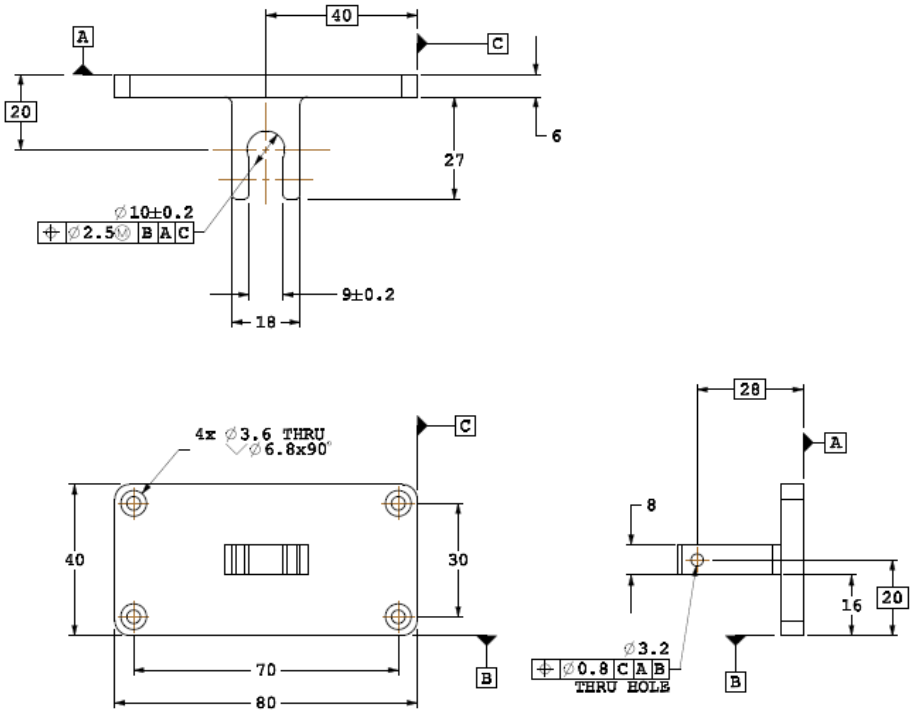

Figure 4.9: Technical drawing of the multi-purpose holder

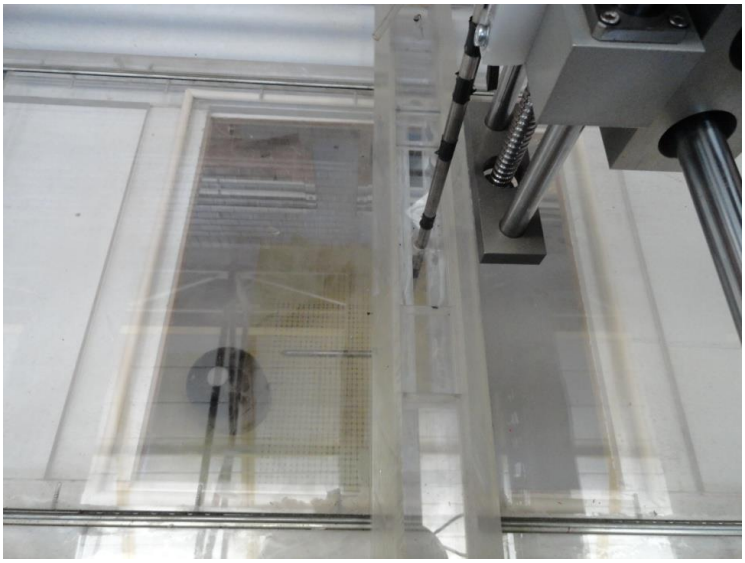

Figure 4.10: Traverse mechanism and upper wall of the test section

4.4 Equipments for Drag Force Measurements

To obtain the drag force exerted on the gimbal model and the coefficient of drag, C_d, for different free stream velocities, some measurements are performed by the usage of several equipments. First of all, a load-cell is designed for the direct measurement of the exerted drag force. The load-cell which is made of aluminum has four strain gages glued on it basically. It is designed specifically for the drag measurements of the gimbal model; however, being usable of the load-cell with different tested models, available in fluid mechanics laboratory, for the drag measurement is taken into consideration during design process. Also the measurement range and the sensitivity of the drag-cell are some other important points and they are considered as well. Further information and details about the design of the load-cell can be found in Appendix A. The load-cell is fixed to the model by using M2 screws and nuts rigidly.

Figure 4.11: Load-cell

Figure 4.12: Assembly of the load-cell and the model

Circuit containing strain gages laying on the load-cell was fed by a power supply. In fact, the circuit composed of strain gages, which are actually resistances, has a feature of Wheatsone bridge. Thus, an output signal can be read from related points of the Wheatsone bridge according to applied force to the load-cell since with the

applied force resistance value of strain gages changes and change in output voltage value can be detected. Output signal of the load-cell can be read by a multimeter and an oscilloscope is used to record the output data.

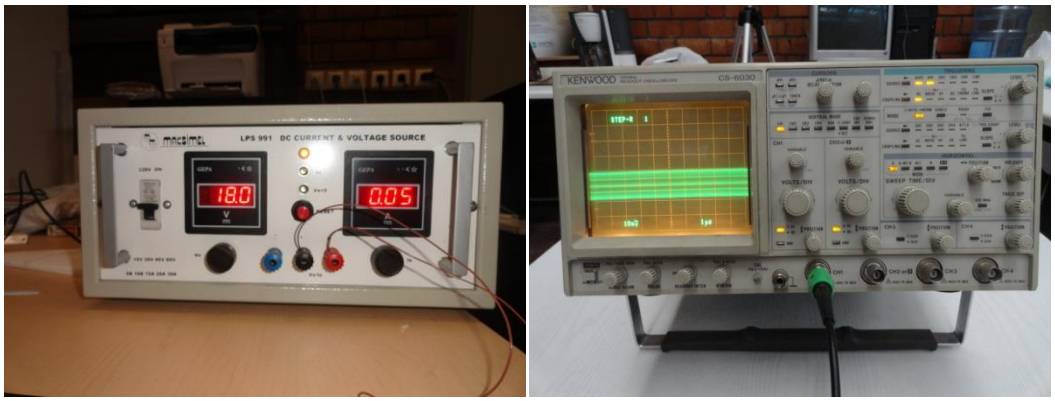

Figure 4.13: Power supply and oscilloscope

Figure 4.14: Loadcell-model assembly in test section

4.5 Pitot-Static Tube

In the wind tunnel experiments, pressure is the one of properties that are desired to be measured. A Pitot-static tube, also called Prandtl tube, is used to measure the pressure values at desired points on the test section. It is hung down to the test

section thereby being passed inside the hole on the sliding mechanism of the upper wall of the wind tunnel and assembled to the z axis of the traverse mechanism with the multi-purpose holder. It has a length of 75 cm approximately and its diameter is nearly 1cm. So, its length is adequate for scanning the test section when assembled to the traverse mechanism.

Figure 4.15: Pitot-static tube in test section

A Pitot-static tube mainly has the capability of measuring the total pressure and static pressure simultaneously. The hole at the tip of it is responsible for the total pressure and the peripheral holes, which are relatively small compared to the hole at the tip,

detect the static pressure. It is possible to deduce that one can obtain the dynamic pressure and, as a result, the flow velocity by using Pitot-static tube.

4.6 Air Flow Meter

Flow velocities at several points of test section are measured by this equipment. It has a connection with Pitot-static tube. It senses pressure differences between two output pressures of Pitot-static tube, which are total and static pressure and this difference means the dynamic pressure. For negative flows it also gives an output; but, the accuracy of the output is unknown and output values must be compared with known values. Therefore, it is not preferred for measurements of negative flow region.

Figure 4.16: Air flow meter

4.7 Laser Doppler Anemometry (LDA)

Laser doppler anemometry is a technique for measuring the flow velocity of fluids by Doppler shift of a laser beam. Owing to transparent lateral walls of test section this technique could be used for measuring flow velocity at some certain locations since it is an optical technique that uses intersecting laser beams. Intersection point is the measurement volume of LDA. However, it needs some tracer particles to obtain a successful measurement. For this purpose, smoke generator placed at the beginning of the wind tunnel was used.

LDA is an advantageous technique since it is an absolute measurement technique. This means that no calibration is required for this device. In addition to measuring the velocity, turbulence intensity of the flow can be acquired by LDA.

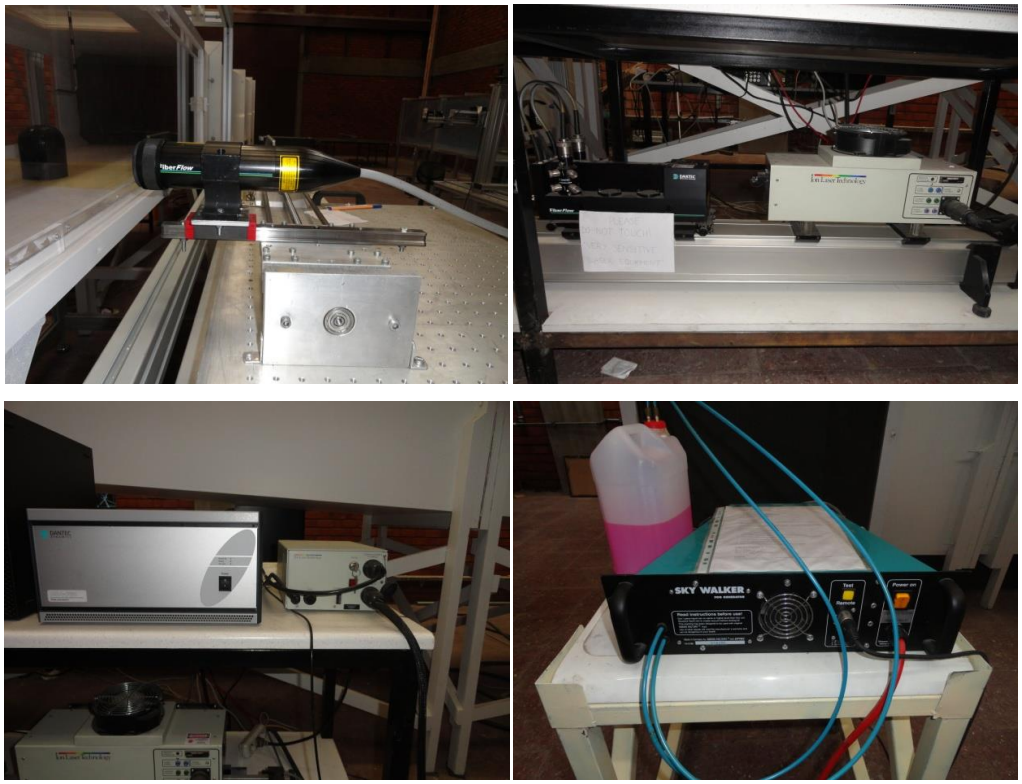

Figure 4.17: Components of LDA

LDA data is collected via the processor of the device which runs in the computer. User friendly interface of the processor simplifies the utilization of LDA technique.

4.8 Hot Wire Probe with Multifunction Measuring Instrument

Hot wire anemometry is a method for measuring flow velocities which stands for the basic principle of the heat transfer. Heat is transferred from the heated wire, which is an element in a bridge circuit, to the cold surrounding fluid. Convective heat transfer coefficient and thereby heat transfer are functions of the fluid velocity. Temperature of the heated wire changes with the change of fluid velocity. Then, resistance of the heated wire also changes. Finally the output of the bridge circuit is affected. Thus a relationship between the fluid velocity and the electrical output can be established.

Flow velocities at some points are measured by a multifunction measuring instrument working with a hot wire probe. Hot wire probe senses the velocity of the flow and gives the absolute value of the flow velocity. It is not useless for negative flows. However, it does not give any opinion related to direction of the flow. By courtesy of this feature, flow velocities are measured in negative flow regions which have been known previously.

Figure 4.18: Hot wire probe and multifunction measuring instrument

4.9 Manometer

Detected pressures by Pitot-static tube could be visualized by connecting the outlet of the total and the static pressure holes of Pitot-static tube to the simple manometer. Manometer is a simple device that shows the difference from the atmospheric pressure. Inclination of the manometer tubes, the angle between tube and ground, was important for the readibility of the liquid level since the inclination increases the travel path of fluid and even big differences can be observed.

4.10 Flow visualization equipment

It is tried to visualize the flow over the body. Some equipment is used for the flow visualization. First of all, images are taken by a CCD based image sensor. Smoke is generated by a CO_2 tube and the plane of visualization is lightened by a light-beam source. For more homogenous smoke flow over the body, a comb like instrument is used. It divides the CO_2 smoke coming from one tube into smaller tubes.

Figure 4.19: CO2 smoke generator tube and comb-like instrument

CHAPTER 5

WIND TUNNEL EXPERIMENTS

Experiments constituted the significant portion of this study. Therefore, in this chapter, conducted experiments are explained. Experimental procedure is also mentioned. It is tried to be told that which measurements must be done for which purpose. Equipments and set-ups explained in previous chapter were used in these experiments.

5.1 Design of experiments

It can be said that the main aim of the experiments is to obtain the drag force and the drag coefficient of the gimbal model under certain conditions. It is planned to be done with two different ways. One is the direct measurement of the force exerted on the gimbal model by using the load-cell which was designed and manufactured. The other way is the drag estimation by momentum equation. For carrying out this scope, an experimental procedure is followed in a rational manner. Experiments are designed according to following notes and steps.

1. Due to being an experimental study with a wind tunnel, firstly the wind tunnel characteristics must be found out. Since it is driven by an axial flow fan which is controllable via the control panel, mentioned in previous section, by changing the rotational speed of the axial fan, free stream flow velocities must be measured at specific capacity rotational speed values nearly at middle points of y and z axis at any cross section. Free stream velocities can be measured by either LDA or Pitot-static tube.

2. After measuring free stream flow velocities, flow uniformity in the test section of wind tunnel must be examined. Boundary layer of the tunnel must be observed. Scanning the points at every section decided to be examined and at around walls of test section systematically for measuring flow velocities can be performed by traverse mechanism and Pitot-static tube. In other words, the wind tunnel must be calibrated.

3. With regard to calibrated tunnel velocity data and flow conditions enhanced by the model in real cases, some free stream values with which measurements are done must be decided.

4. Tested body must be positioned according to the range of the traverse mechanism in x and y axis since wake surveys of the body are supposed to be made.

5. Turbulence intensity must be obtained with respect to chosen free stream velocities absolutely by LDA for further interpretation of the results of experiments. In fact, it is more reasonable to evaluate the results according to measured turbulence intensities.

6. After understanding the wind tunnel basics, drag force measurements are performed by the load-cell. Calibration of the load-cell is an essential step that must be done before the drag measurements.

7. For applying the other drag estimation method which is based on basically conservation of momentum equation, wake surveys are planned. Term of wake survey stands for investigating the wake region of the model by taking several measurements. Wake region of the model is scanned section by section, along x axis, and sections, y-z planes, are scanned point by point to measure desired properties, which can be used for evaluation of the drag

equation obtained, such as flow velocity and static pressure. Then, measurement data are processed and used in the drag equation derived from conservation of momentum to estimate the drag force.

8. Observations of the flow over the model, especially observations of wake region are planned for selected free stream velocities by flow visualization technique in which CO_2 smoke is used in fluid media for easy-imaging with the help of laser beam.

5.2 Experimental Procedure

As mentioned in previous part, experimental work is designed. In this section, experimental procedure and calibration process and data of some instruments used in experiments are explained.

5.2.1 Wind Tunnel Measurements without Model and Calibration

As stated in design of experiments part, first of all characteristics of the wind tunnel must be known for conformity of the latter experiments which are related with the drag force measurement, which is the main task of this work.

Firstly, free stream velocities of wind tunnel are checked. During this process, free stream velocity is increased gradually by increasing the rotational speed of the axial flow fan and general observations is completed related to vibration level and free stream turbulence intensity. Free stream velocities are measured by LDA and Pitot-static tube at several wind tunnel conditions. Also turbulence intensities with increasing free stream velocity are obtained by LDA. It is seen that the turbulence intensity level of the wind tunnel is below 1.5% during these steps of experiments. Therefore, results of other measurements such as drag coefficient must be interpreted

according to this level. In the light of these observations and measurements, some free stream velocities are selected for wake surveys to work.

At this point a few things about the selected free stream velocities, thereby Reynolds number, can be said. Main reason to work with these velocities is the operating condition of the real system, which is a mini UAV. A typical mini UAV has a maximum velocity of 20-25 m/s approximately. In a routine flight, the UAV travels at around 10-15 m/s. According to this data, higher free stream flow velocities must be selected. However, condition of the wind tunnel didn't allow higher flow velocity selections. It is the fact that the wind tunnel has high level vibrations, because of the trouble thought to arise from axial flow fan, at around 20 m/s free stream flow condition which corresponded to rotational speed of 800 rpm for the axial fan. Since this situation is risk factor for the wind tunnel and other equipments, the highest working velocity is decided as around 15 m/s which simulates approximately the normal operation of the UAV. Thus, the other flow velocities are selected according to the highest working velocity. Moderate one is around 10 m/s and the lowest free stream velocity is selected as around 5 m/s..

Flow uniformity of the wind tunnel is one of the significant criteria for the wind tunnel tests. It is needed for the determination of the measurements planes and points. For the examination of the flow uniformity traverse mechanism is used easily for flow investigation of several location of the test section. However, movement area of the traverse mechanism is restricted by the upper wall of the test section. It travels 35 cm on the x axis beginning from the section which has a 160 cm distance from the starting point of the test section. It also travels limitedly on the y axis. Regarding the middle point of the y axis as zero, the traverse travels +18 cm and -18 cm from the zero, 36 cm travel as total. Actually the traverse has a self-limit. It can move up and down 20 cm totally. However, this problem is disappeared since Pitot-static tube used in experiments has a sufficient length. Therefore, in contrast to x and

y axis, there is no limitation about the movement on the z axis and it is possible to get measurements at desired locations of the z axis.

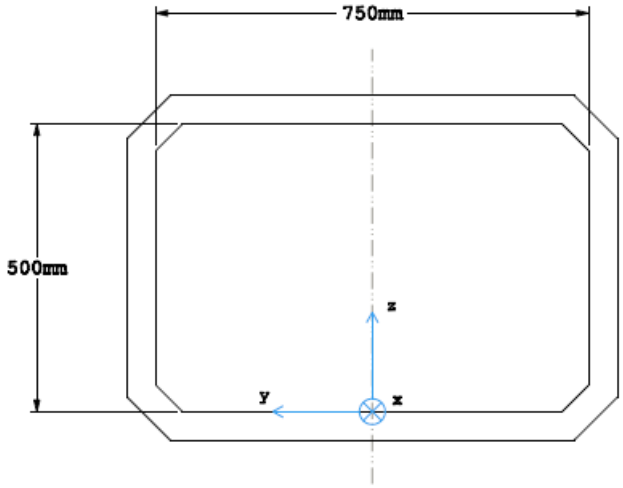

Figure 5.1: Cross-section of the test section and 3D coordinate system

Inside of the limits of the traverse motion, free stream flow measurements at different points of the test section are performed and consequences related with the flow uniformity are reached.

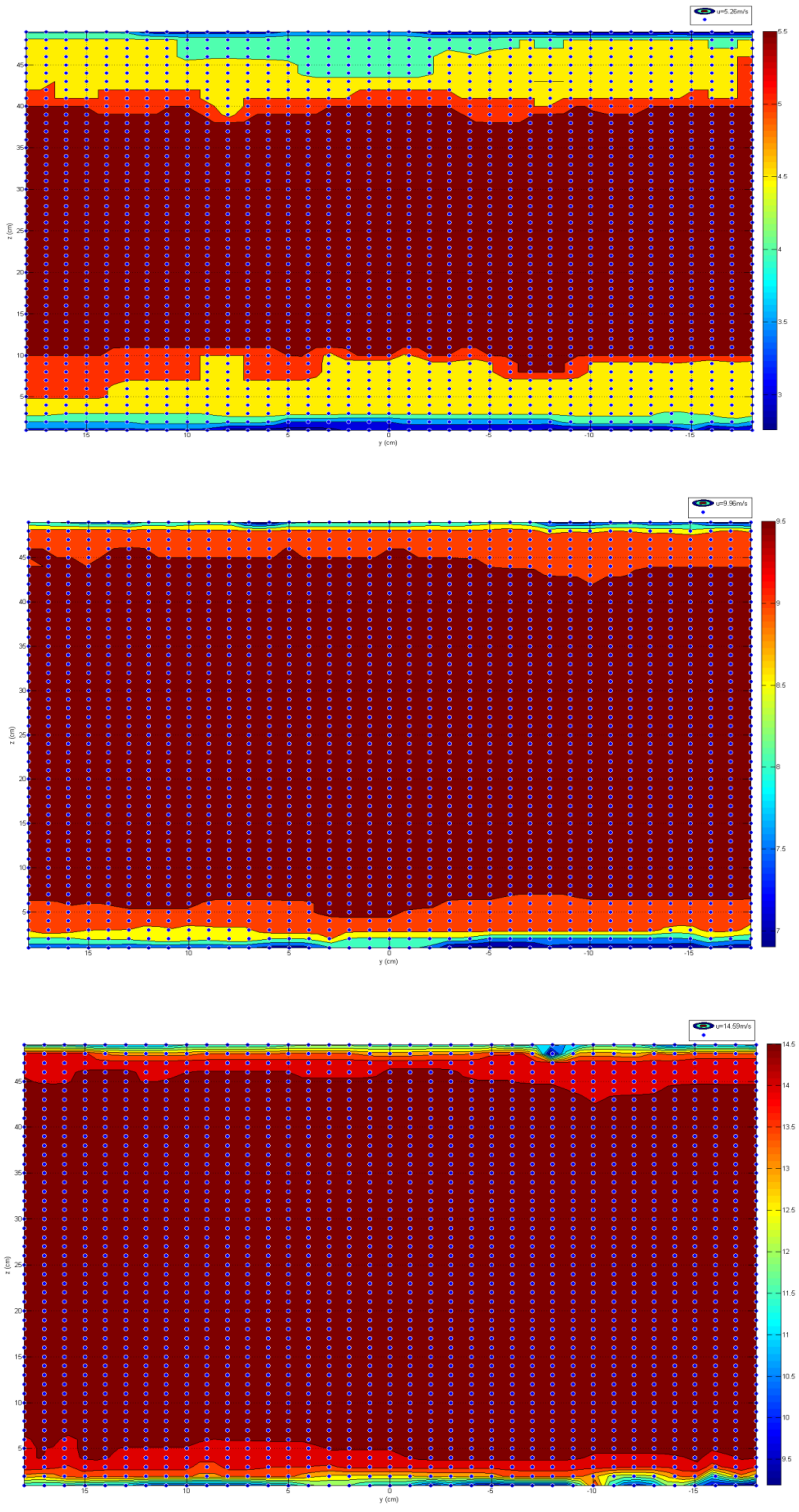

Figure 5.2: Flow uniformity for free stream velocities of 5.26 m/s, 9.96 m/s and 14.59 m/s

After examination of flow uniformity, the model is placed at a certain point in the test section. The location of the model in test section is selected according to not only flow uniformity results but also movement range of the traverse mechanism. It is placed 125cm from the beginning of the test section in x axis. Also symmetry axis of the model was coincident with the zero of y axis.

5.2.2 Drag Force Measurements with Load-cell

Drag force measurements are performed by using designed load-cell. For different free stream velocities, corresponding drag force is measured.

Wheatstone bridge circuit composed four identical strain gages is fed with a power supply. Then the output of the Wheatstone bridge which is supposed to be in milivolt levels could be read by using simple multimeter or oscilloscope. It is decided for the circuit of strain gages to feed them with 18V. The reason underlying this decision is related with the characteristics of the load-cell. When fed with lower voltage values than 18V, the sensitivity of the load-cell measurement decreases. On the other hand, higher supply voltages than 18V cause the load-cell, which is made of aluminum, to warm up and this situation leads to some problems. In fact, when warming up, irregularity of the load-cell output increases and it starts to give nonsense measurement values. It causes measurement errors to arise randomly. Therefore, after a few trials, it is seen that 18V was the optimum value for supplying the circuit of strain gages. Before the measurements, there is an inevitable step for the load-cell. This step is the calibration of the load-cell. The calibration of the load-cell is a very essential process and part of the drag force measurement. It is done by known weights and outputs of the load-cell corresponding to each weight are recorded. Then, the calibration curve of the load-cell is obtained. Actually two calibration processes combined are performed. By starting from lowers, calibration loads are gradually increased and the calibration curve is finalized.

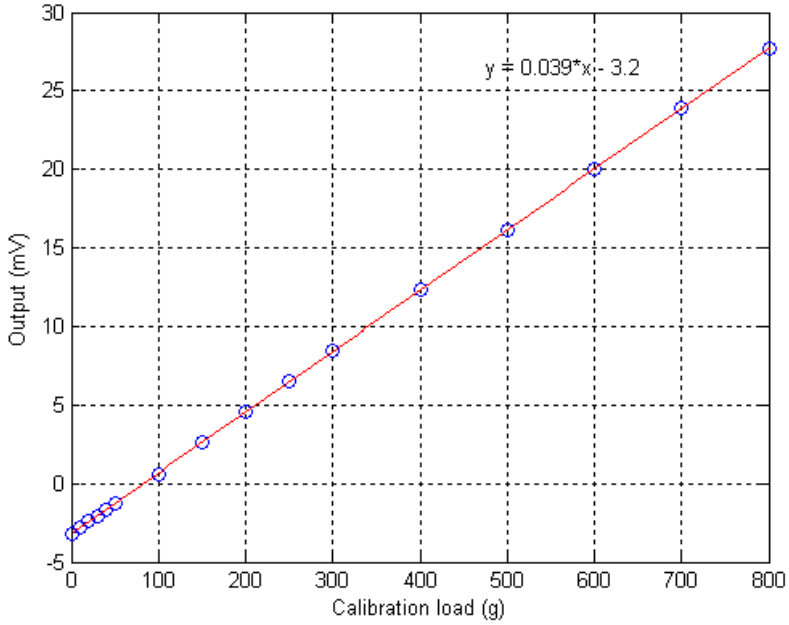

Figure 5.3: Calibration curve of the load-cell

Table 5.1: Calibration data of the load-cell

Calibration load (g)	Measured output (mV)	Calculated output from calibration curve (mV)	Percent error
0	-3.2	-3.2	0
10	-2.8	-2.86	1.99
20	-2.4	-2.47	2.87
30	-2.1	-2.08	0.86
40	-1.7	-1.7	0.29
50	-1.3	-1.31	0.63
100	0.6	0.63	4.38
150	2.6	2.56	1.51
200	4.6	4.5	2.28
250	6.5	6.43	1.08
300	8.5	8.36	1.6
400	12.3	12.23	0.54
500	16.1	16.1	0.01
600	20	19.97	0.14
700	23.9	23.84	0.25
800	27.7	27.71	0.03

As seen in Figure 5.4 and calibration data table, Table 5.1, a well-suited curve is fitted to the calibration data. Percent errors calculated from the fitted curve with respect to known weights are around 5% in the maximum case. This is evidence that the calibration was successfully done for the load-cell.

After the calibration process, drag force for different free stream velocities was measured by the help of the load-cell. Results of these measurements will be given and discussed in the next chapter in detail.

5.2.3 Wake Surveys

As stated before in previous sections, the drag force and the coefficient of the drag would be estimated with another method in which simply the conservation of momentum equation is used. For this method, a control volume was determined and the momentum equation was applied to the selected control volume. Free-stream conditions were basically the inlet conditions for the control volume. However, at the outlet the flow conditions were not very easy to be used directly. Therefore, wake surveys were performed for eight y-z planes. The main aim of these surveys was to observe flow characteristics at different locations behind the body and to get some measurements at some suitable points to be able to use them for the conservation of momentum equation.

At y-z planes behind the body different velocity profiles were obtained. Velocity and pressure values are recorded point by point which are located in y-z planes with a 1 cm distance from each other on both y and z direction.

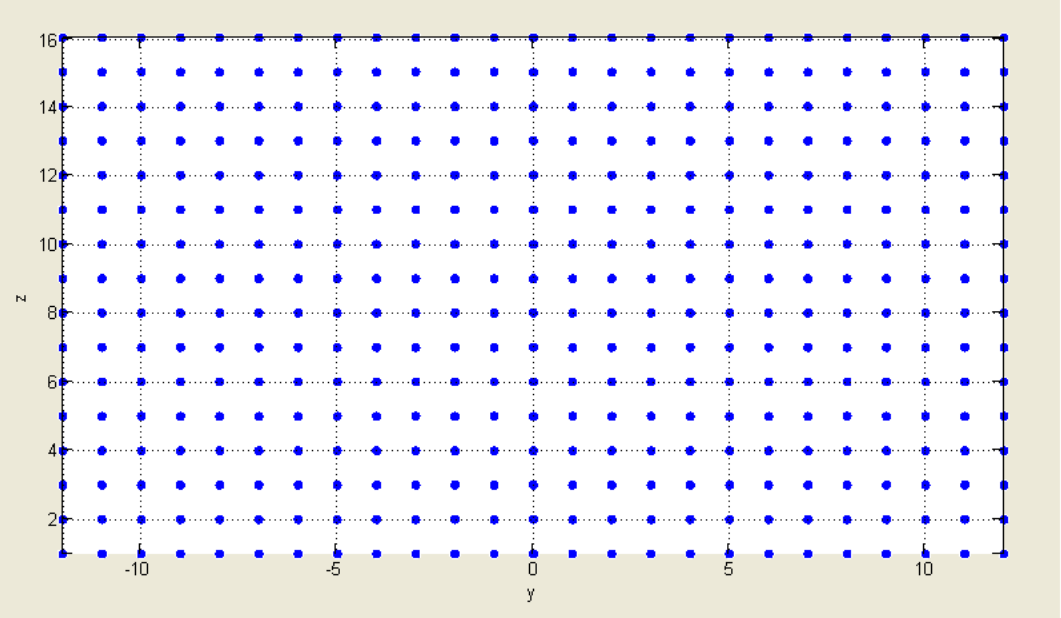

Figure 5.4: y-z planes of test section

In Figure 5.6, a schematic representation of a y-z plane can be observed. Every spot in the figure stands for the approximate measurement points. Existence of a traverse mechanism made easier to cope with wake surveys. Roughly four hundred points on each y-z plane were examined and the desired data was got at these points.

CHAPTER 6

RESULTS AND DISCUSSIONS

As stated at some points, the main aim of this thesis work is to analyze the characteristics of the flow around the gimbal body. Especially coefficient of drag for the gimbal and the drag force acting on it for different free stream velocities are basic concerns of the study.

Two different methods for drag estimation are used. First of all a load-cell is designed and manufactured. Detailed information about the load-cell design and calculations are given in Appendix A. In the wind tunnel drag force is measured directly by the means of the load-cell. This is the experimental way of measuring the drag force and coefficient of drag. Drag is also examined with another way. That is the estimation of the drag force by utilizing the conservation of linear momentum principle. For this purpose a momentum equation is applied to the control volume surrounding the body. However, flow characteristics at some certain planes of the control volume must be known to solve the momentum equation for the drag force. At that point again wind tunnel experiments are necessary for solving the momentum equation used. Therefore, the second method is the combination of experimental and analytical progress. Results obtained from these methods are compared with each other.

In this chapter, results of drag estimations are presented and discussed. Also at the end of the chapter some visuals acquired via the flow visualization technique, discussed earlier, for the tested body are given.

6.1 Results via Load-cell

After the calibration process which is mentioned in previous chapter, the gimbal body is assembled to the load-cell and wind tunnel experiments starts. With the load-cell a series of drag force measurement is performed.

Drag force measurement is done for different free stream velocities. The main purpose of measurement for different free stream velocities is to have more data and actually widen the data range. This will provide to interpret drag force results more correctly. Successively, the coefficient of drag is obtained for each case by further calculations. The results of drag force measurement with the load-cell can be seen in Table 6.1.

Table 6.1: Results of drag force measurement with the load-cell

U (m/s)	Re	D (N)	C_d	C_{d_cor}
5.26	$4.85x10^4$	0.42	1.35	1.23
6.81	$6.28x10^4$	0.65	1.32	1.20
8.62	$7.94x10^4$	0.96	1.29	1.17
9.96	$9.18x10^4$	1.29	1.28	1.16
11.63	$1.07x10^5$	1.65	1.24	1.13
13.18	$1.21x10^5$	2.12	1.18	1.07
14.59	$1.35x10^5$	2.46	1.09	0.99
16.25	$1.50x10^5$	2.72	1.01	0.92
17.99	$1.66x10^5$	2.95	0.91	0.83
20.06	$1.85x10^5$	3.31	0.81	0.74

In Table 6.1, first column represents free stream velocities for which drag force measurements are performed with the load-cell in the wind tunnel. Corresponding Reynolds numbers to free stream velocities, drag force, coefficient of drag and corrected coefficient of drag are given in the columns of the table respectively. It is natural to see the increase in the drag force with increasing free stream velocity.

Drag coefficient and its corrected form are presented in the table. Actually, variation of the coefficient of drag with Reynolds number is worthy to analyze and comment. It can be said basically by commenting on the table that drag coefficient is in downward trend. It decreases with increasing free stream velocity, in fact Reynolds number. However, it is not fair to make further comments of drag coefficient variations by looking at the table. Graphing the variables usually adds more sense to the tabulated data. For this purpose Reynolds number versus coefficient of drag curve is plotted.

In addition, a correction related to the blockage effect in the wind tunnel, available in Appendix C, is applied to the drag coefficient as seen. Then, the corrected form of drag coefficient is used in the related graph.

Two types of plot can be seen in Figure 6.1 and 6.2. One of them is plot of Reynolds number versus drag coefficient in linear scale. It can give an idea about drag coefficient variation. The drag coefficient decreases with increasing Reynolds number. Actually it is argued by looking at the drag coefficient result table generated by drag force measurements via the load-cell for ten different free stream velocities that until a level of Reynolds number the drag coefficient can be considered as almost a constant. After this level, sharper decreases in the drag coefficient are observed clearly. As a fact, flow is laminar for low Reynolds number. Then transition from laminar flow to turbulent flow starts with further increase of Reynolds number. Sharper decrease of drag coefficient is an evidence of transition to turbulent flow. Turbulent boundary layer having much momentum than laminar boundary layer to withstand the viscous effects, one of the causes of separation, shifts the separation point forward on the immersed body and the separation is delayed. In both laminar and turbulent flows wake region is observed. However, wake region is smaller in turbulent flows by the help of separation delay and direct consequence of this situation is a decrease in the drag coefficient. It must be taken into account that wake region of the body due to flow conditions and transition to

turbulent is related to the immersed body shape and positioning of the immersed body with respect to the flow around it. For example, in a vertical plate, the drag coefficient does not vary with Reynolds number. Owing to its shape, it can be stated that turbulent flow delays the separation on the gimbal, above discussions are valid for it also and it can be shown as the reason of the drag decrease seen on plot.

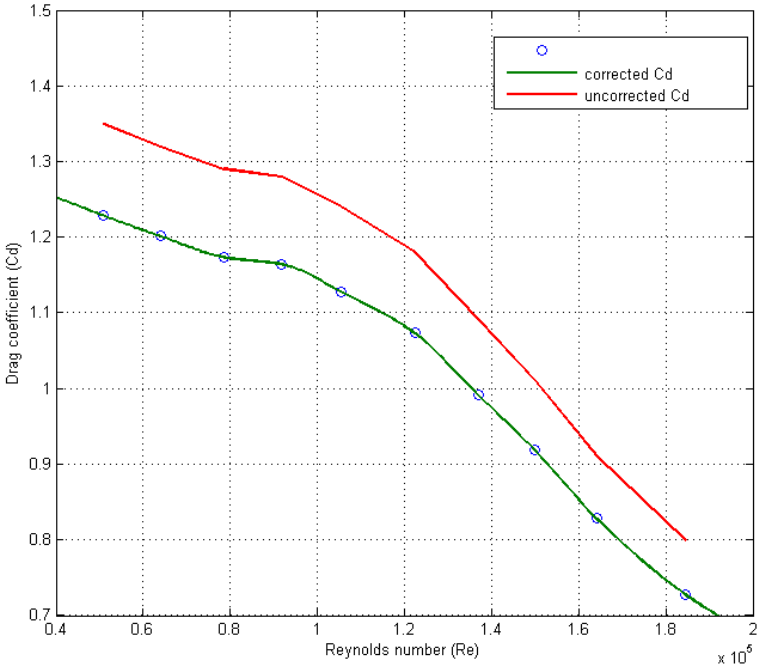

Figure 6.1: Reynolds number vs drag coefficient graph in linear scale

To compare results more sensibly, log-log scaled graph of Reynolds number versus drag coefficient is plotted since in the literature log-log scale is used for Reynolds number versus drag coefficient plots of different bodies. Unfortunately, the plot does not contain the results of higher Reynolds number since it is not tried to reach higher free stream velocities in the wind tunnel due to safety considerations. Hence, the plot stops at an early level. Nevertheless, it can be compared with cases of different bodies up to a point. It is stated that the variation of drag coefficient of the gimbal is not very different from that of cylinder and sphere. Similar variations can be seen

from place to place. Variation trend of the drag coefficient of the gimbal with Reynolds number is appeared as suitable and rational.

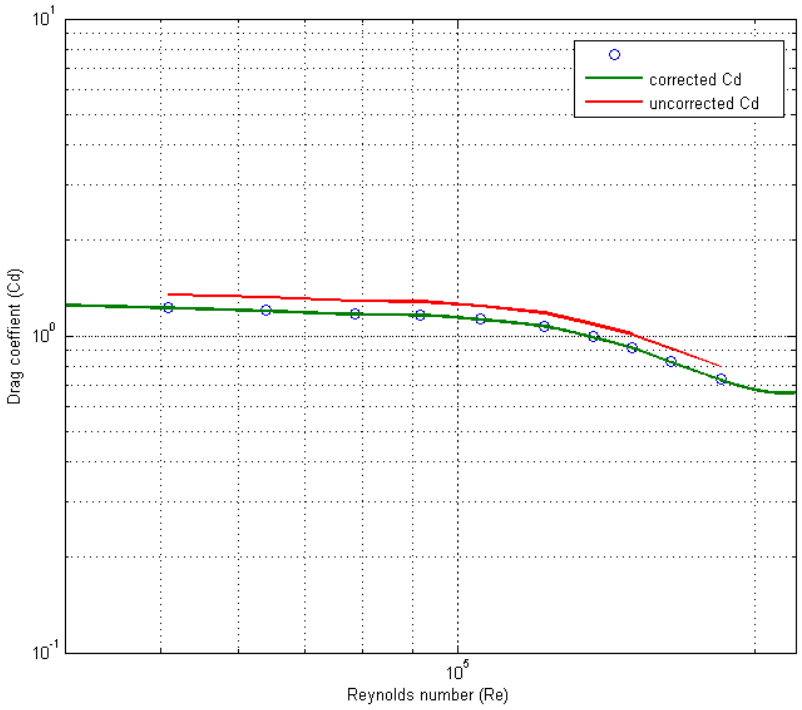

Figure 6.2: Reynolds number vs drag coefficient graph in logarithmic scale

Value of the drag coefficient of the gimbal, however, cannot be compared to any value in the literature since there is not enough work related in the literature due to traditional and military reasons most probably. Nonetheless, it does not seem as nonsense as the value of drag coefficient is not very high or very low compared with resembled bodies. It can be accepted to be in reasonable levels.

6.2 Results obtained by wake-integration method

For predicting the drag force and drag coefficient another method is used. This method is simply the combination of analytical equations and experimental data. Analytical side is coming from application of the conservation of momentum principle on a control volume including the gimbal body.

Before expressing details and results of the applied method, some purposes of the work must be stated. First of all, drag force prediction is the main aim of this method. However, the procedure of estimating drag has quite differences from the direct measurement. Since the control volume analysis is the most important part of this method, the aim of the technique is not directly estimate the drag force. Estimated drag force for certain control volume does not carry a meaning without comparing it with known results which are reliable in terms of its accuracy. Obtained drag force results by utilizing wake-integration method varies with the selected control volume. Inlet plane of the control volume and its selection are straight forward as flow characteristics can be regarded as stable and same at the cross-sections of the wind tunnel at some locations before the body. However, this action is not simple at the exit plane of the control volume. Hence, selecting the most suitable control volume by predicting the drag force and comparing it with known results is desired for this step. For which control volume the method gives better results of drag estimation is main question of the performed work.

For different exit planes of control volume lying behind the tested body measurements are performed. x component of the flow velocity is able to be measured for different planes of wake region. Measurement points of planes were mentioned in previous chapter. Then, surface plots of x component flow velocities are drawn for different measurement planes. It is significant since wake region is visualized basically for different x locations. This gives an idea about the flow and its effects behind the body and can be useful for making some interpretations.

6.2.1 Velocity plots of wake regions

Wake surveys are performed seven different y-z planes. For each plane, x component of the flow velocity and pressure are measured by Pitot tube with the manometer, air-flow meter and hot wire probe, of course by the help of traverse mechanism. Data obtained from these experiments will be used for estimating the drag force. Surface

plots of velocity and related contour plots are graphed via Matlab for getting informed about the flow in wake region.

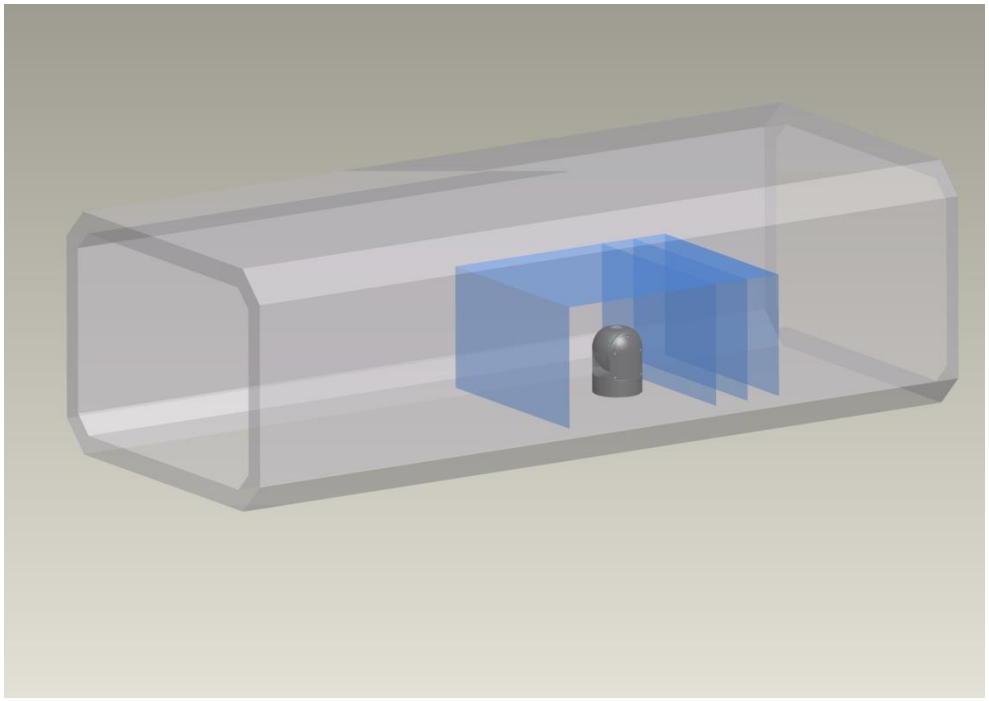

Figure 6.3: Wind tunnel test section and gimbal located in it with three imaginary exit planes of CV

In Figure 6.3, representation of the test section and the gimbal can be seen. For comprehensibility, the test section is shown as transparent. Blue transparent surfaces around the gimbal model symbolize some surfaces of the control volume. Three parallel surfaces behind the gimbal body stand for imaginary exit planes of the control volume which are separately used in wake analysis.

Results of three different free stream velocities are shown for seven different y-z planes as mentioned earlier. y-z planes are named with the distance from the gimbal body. The last point of gimbal body is assumed as origin and the planes are constituted. For example, when expressed for any y-z plane as x=1 cm, it must be

understood that the y-z plane is located 1 cm behind the gimbal body. In addition, the body is placed at y=0 position for all cases.

6.2.1.1 Results of x=1 cm

Surface and contour plots of three different free velocities are represented in following figures.

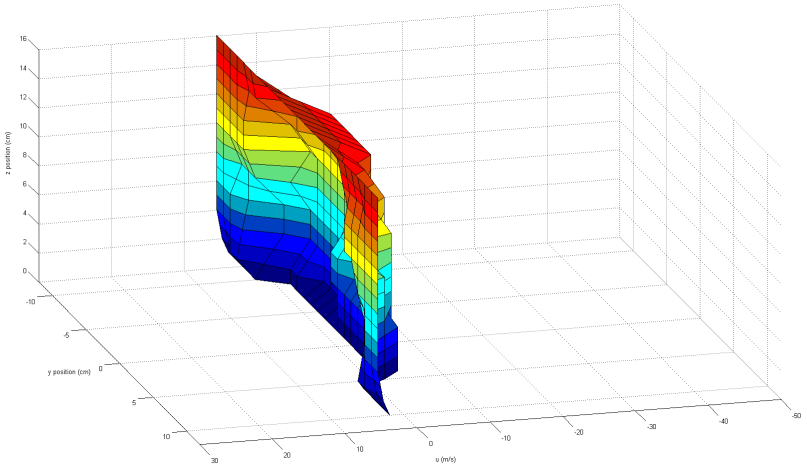

Figure 6.4: u vs y,z plot for U=5.26 m/s, at x=1 cm

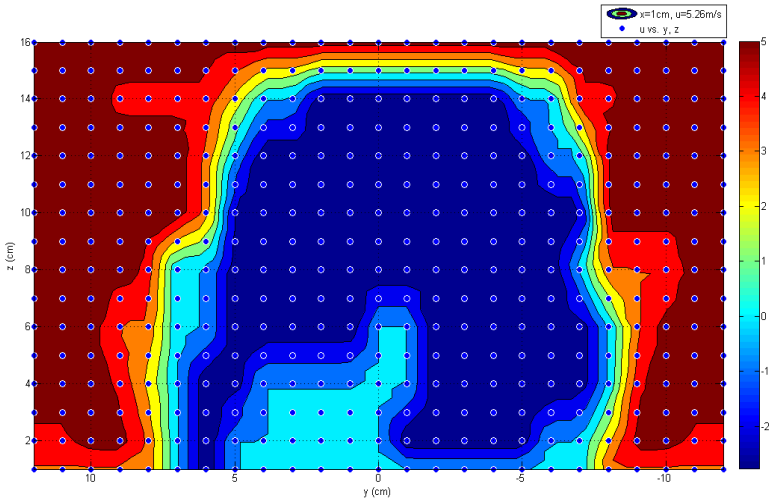

Figure 6.5: Contour plot for U=5.26 m/s, at x=1 cm

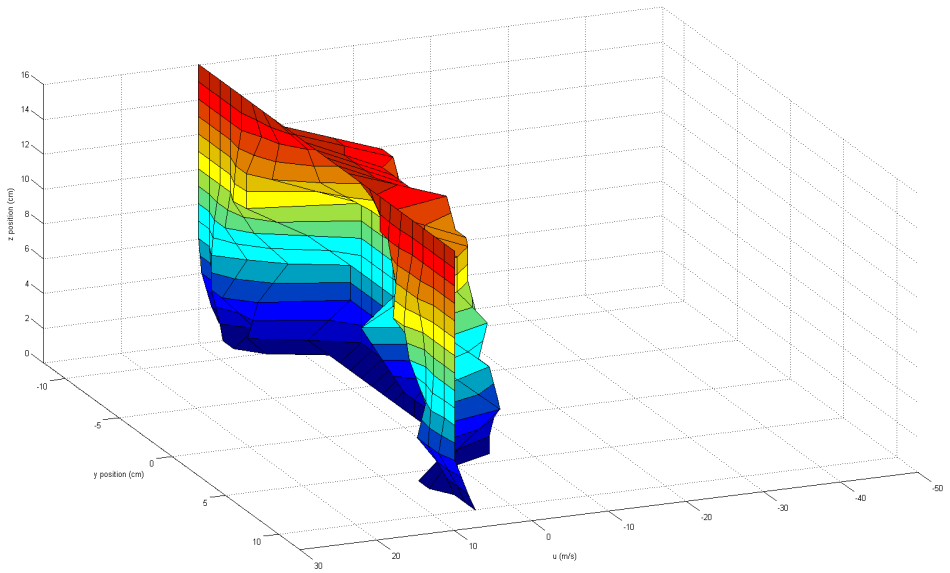

Figure 6.6: u vs y,z plot for U=9.96 m/s, at x=1 cm

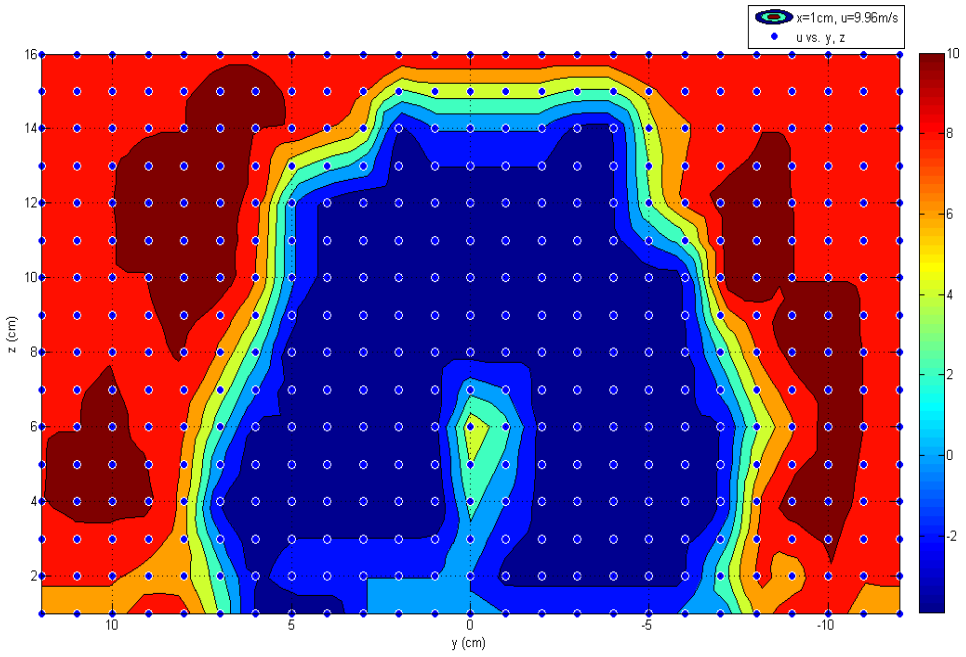

Figure 6.7: Contour plot for U= 9.96m/s, at x=1 cm

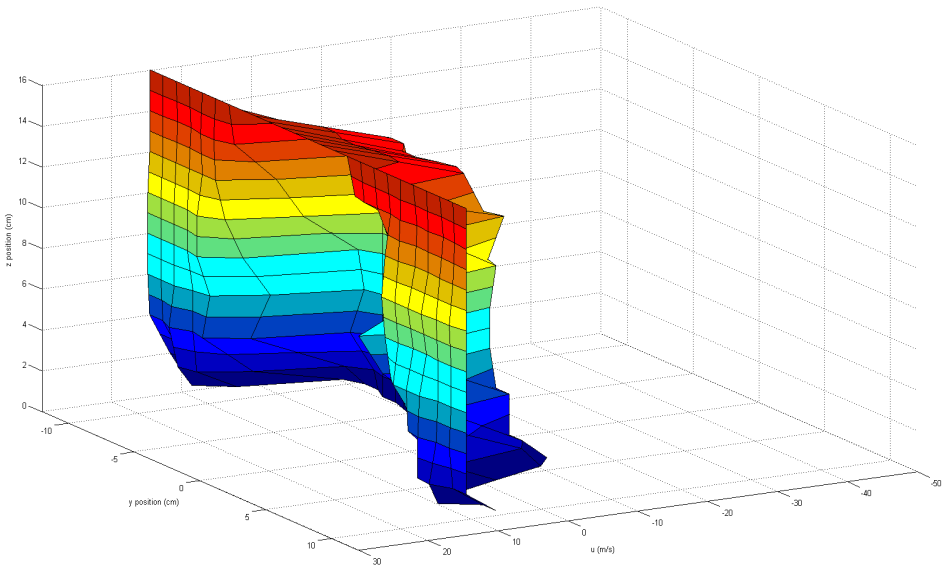

Figure 6.8: u vs y,z plot for U=14.59 m/s, at x=1 cm

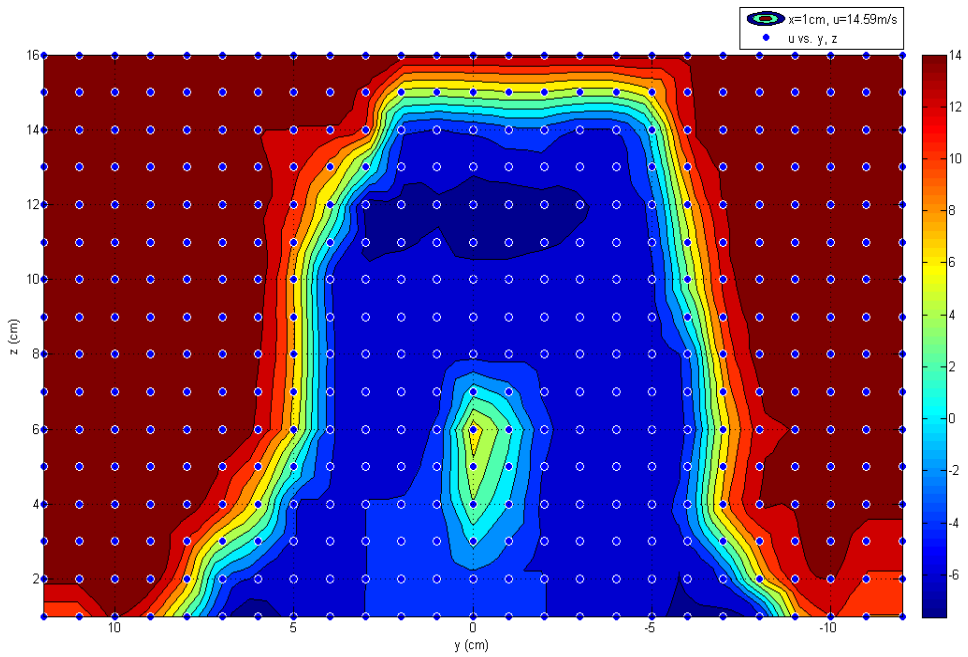

Figure 6.9: Contour plot for U=14.59 m/s, at x=1 cm

Generally, negative values of u are seen for all free stream velocities. Due to the fact that the y-z plane is very close to the body, wake has very dominant characteristics over velocity profiles. These negative values of flow velocity can be regarded as backflows. Vortices are the inevitable consequence of very close plane. Flow characteristics in the wake region are complicated. Flow irregularities can be seen clearly for all free stream conditions. Especially, for U=9.96 m/s, flow regularities are very clear for both y sides of the model. Positive values of flow velocities in locations interpreted as back flow regions are quite remarkable for U=9.96 m/s and 14.59 m/s free stream cases. They can be considered as evidences of instability and chaotic characteristics of the flow for this wake region.

6.2.1.2 Results of x=4 cm

Surface and contour plots of three different free velocities are represented in following figures.

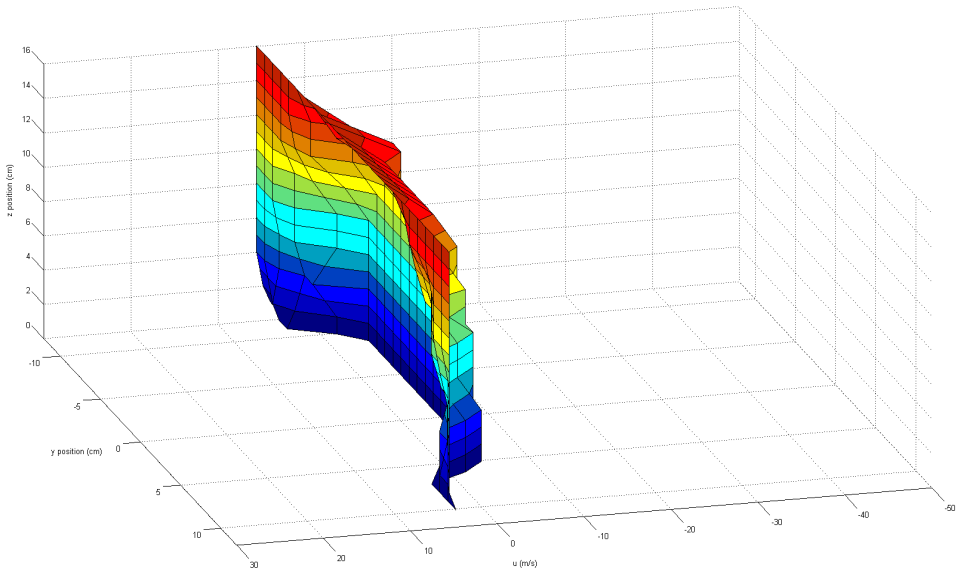

Figure 6.10: u vs y,z plot for U=5.26 m/s, at x=4 cm

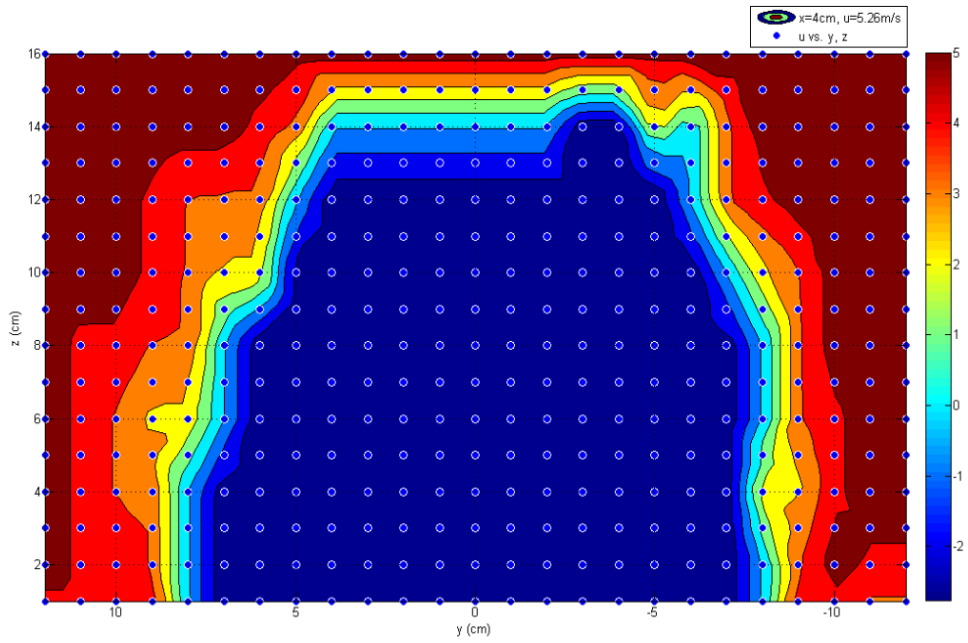

Figure 6.11: Contour plot for U=5.26 m/s, at x=4 cm

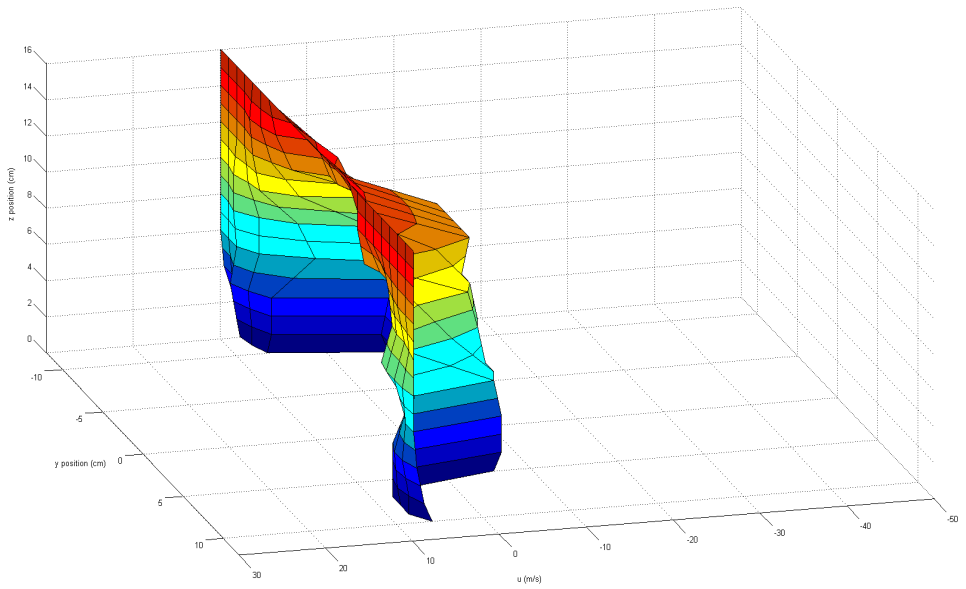

Figure 6.12: u vs y,z plot for U=9.96 m/s, at x=4 cm

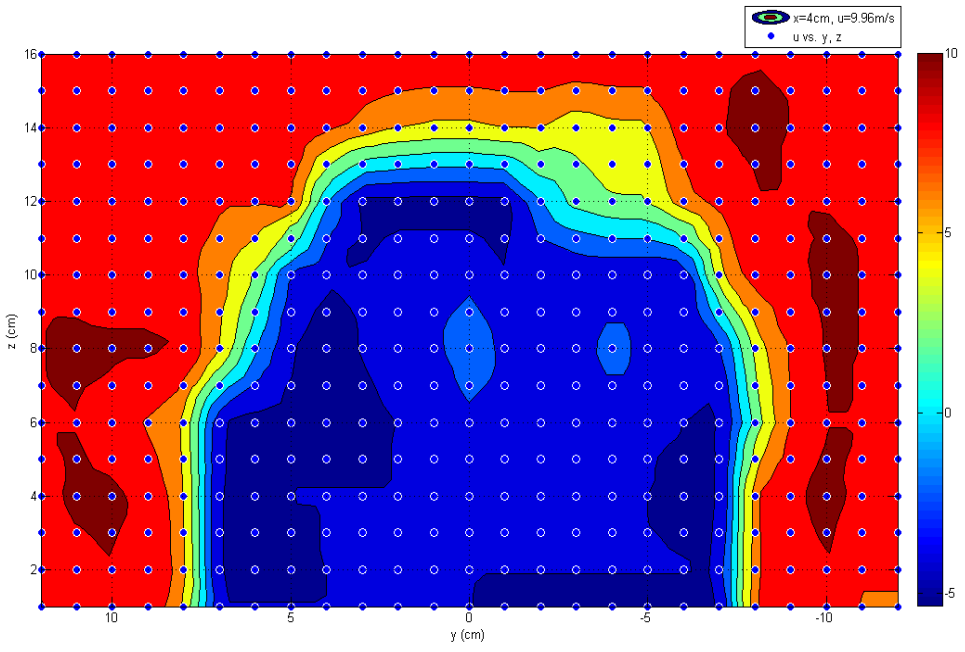

Figure 6.13: Contour plot for U=9.96 m/s, at x=4 cm

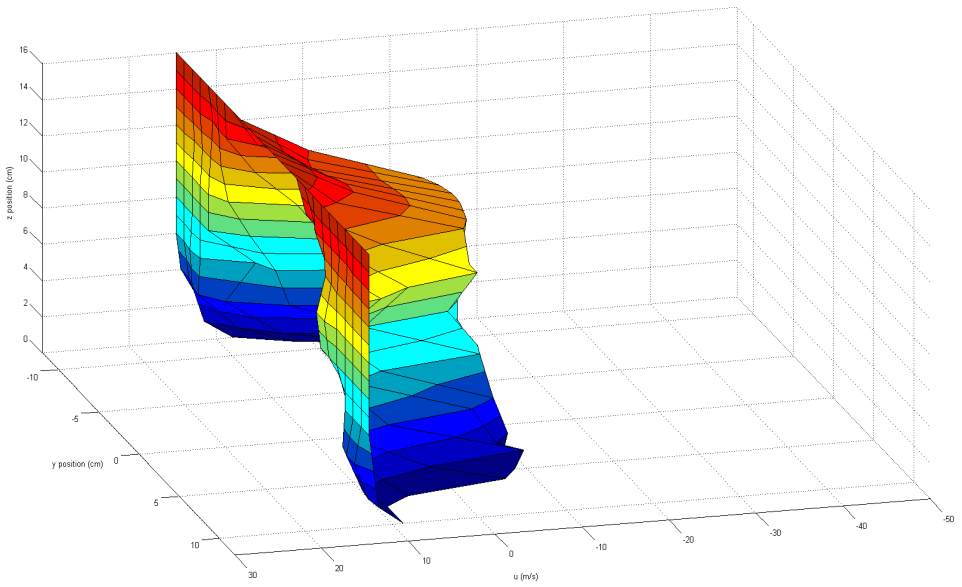

Figure 6.14: u vs y,z plot for U=14.59 m/s, at x=4 cm

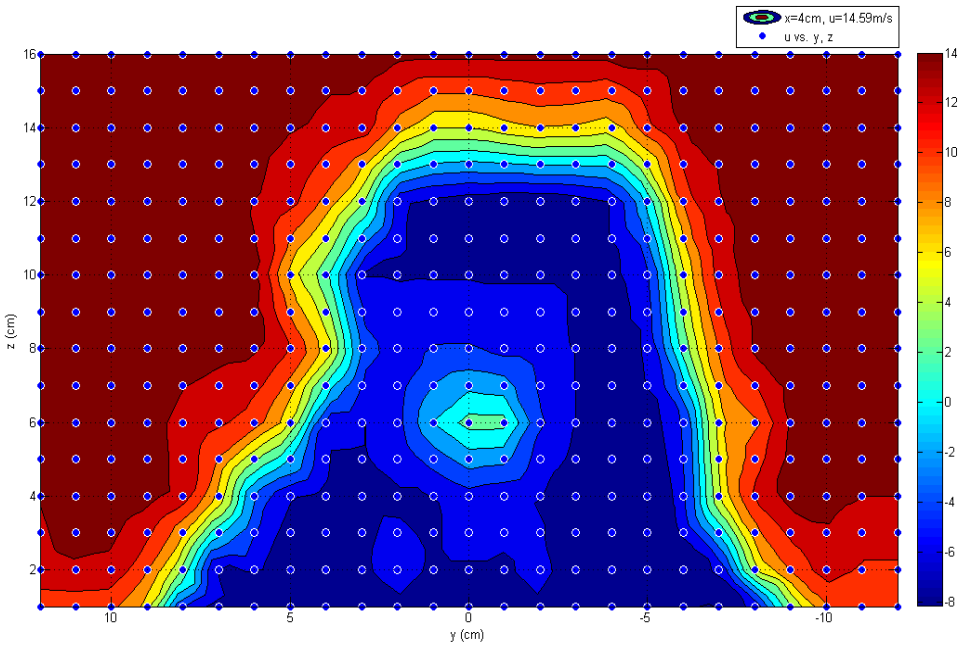

Figure 6.15: Contour plot for U=14.59 m/s, at x=4 cm

For this plane, negative velocity values are seen generally because the plane can be regarded as very close to the body, too. It is possible to talk about the effect of vortices and remarkable backflows of U=9.96 m/s and 14.59 m/s as well. Flow irregularities are still observed; but, the region of high irregularity for U=9.96 m/s located at both sides of the body is a bit smaller compared to previous case. It may mean that this region gets smaller as moving away from the model.

6.2.1.3 Results of x=7 cm

Surface and contour plots of three different free velocities are represented in following figures.

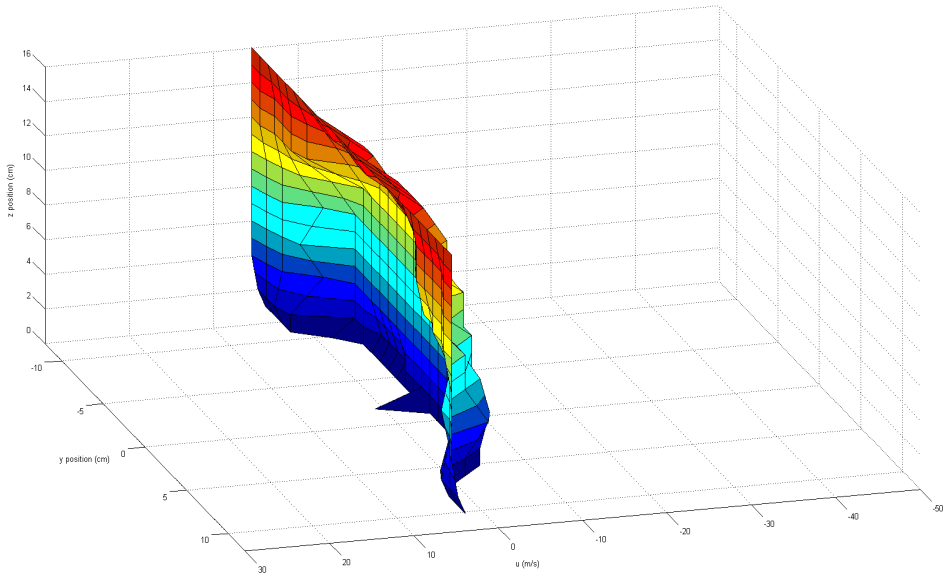

Figure 6.16: u vs y,z plot for U=5.26 m/s, at x=7 cm

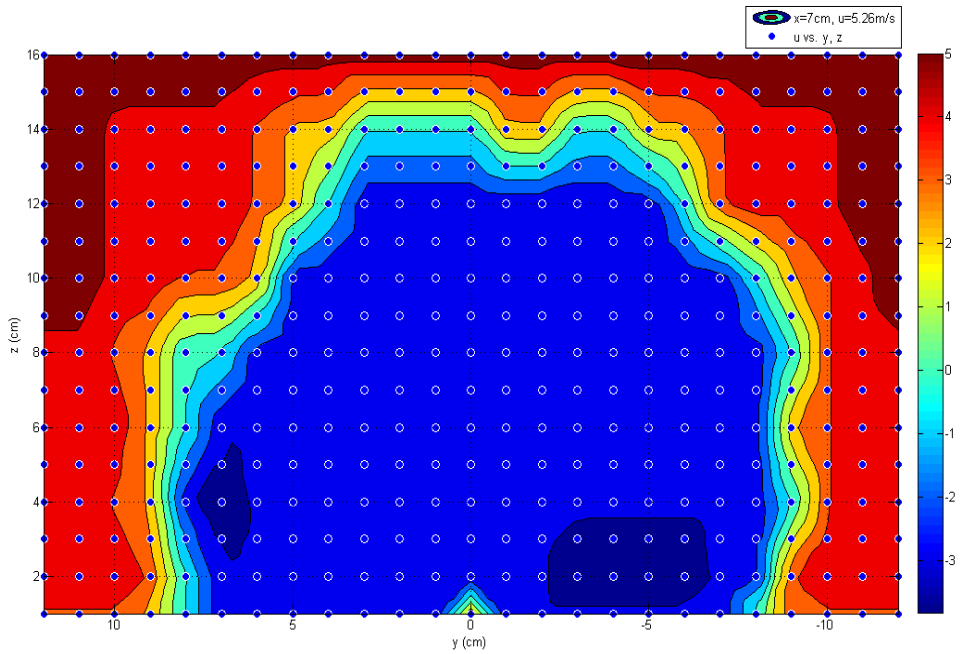

Figure 6.17: Contour plot for U=5.26 m/s, at x=7 cm

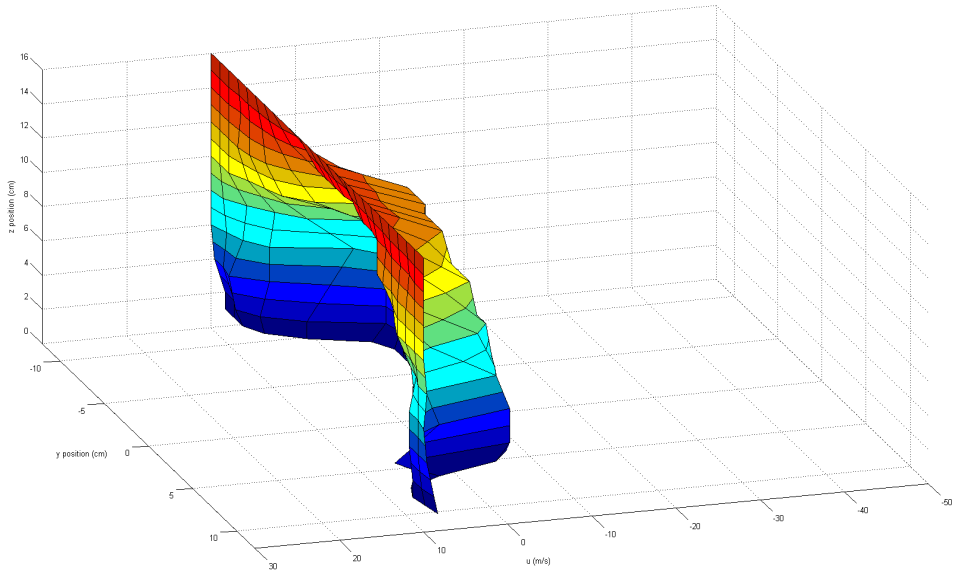

Figure 6.18: u vs y,z plot for U=9.96 m/s, at x=7 cm

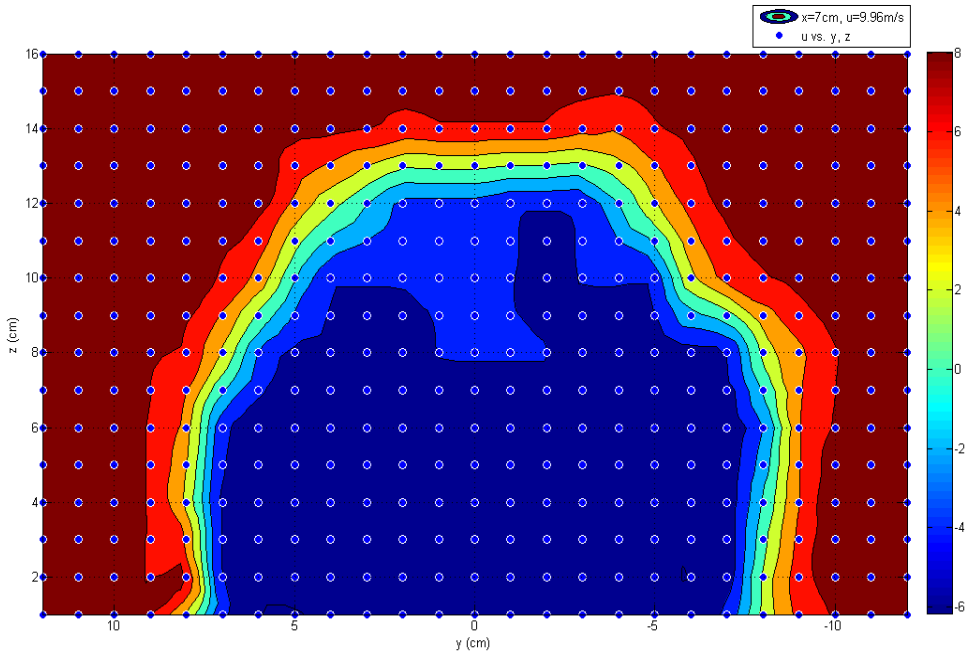

Figure 6.19: Contour plot for U=9.96 m/s, at x=7 cm

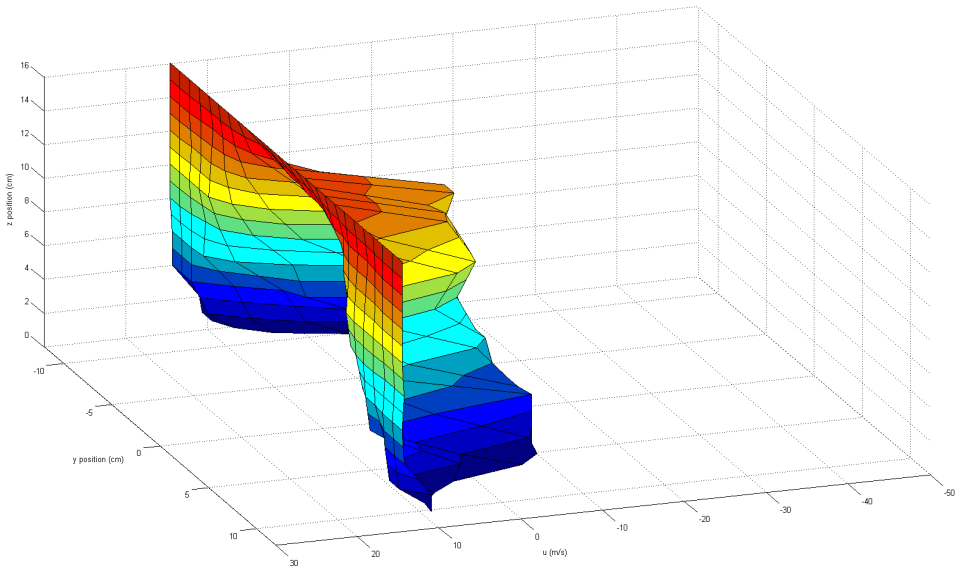

Figure 6.20: u vs y,z plot for U=14.59 m/s, at x=7 cm

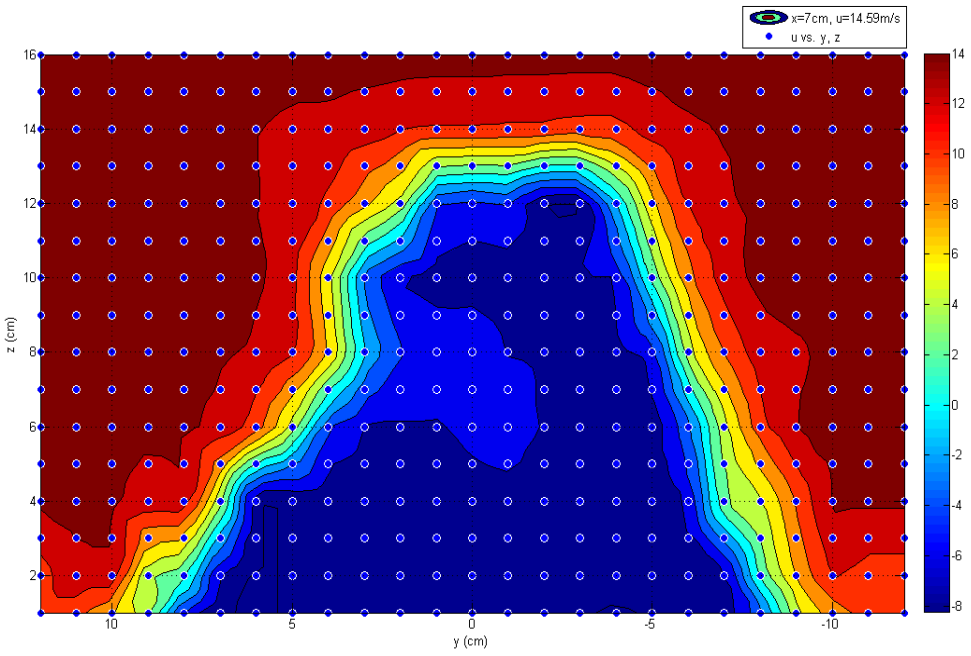

Figure 6.21: Contour plot for U=14.59 m/s, at x=7 cm

Firstly, it can be said that vanishing of observed flow irregularities of previous cases for U=9.96 m/s are seen obviously. It is possible to expect such results as the distance from the body increases. Negative flow regions behind the body are totally dominant in plots. However, for U=5.26 m/s, previously unobserved positive flow in the negative flow region is remarkable. It can be a backflow structure as interpreted before. Also interpretation of measurement error can be rational since this pattern is not expected generally at that location.

6.2.1.4 Results of x=10 cm

Surface and contour plots of three different free velocities are represented in following figures.

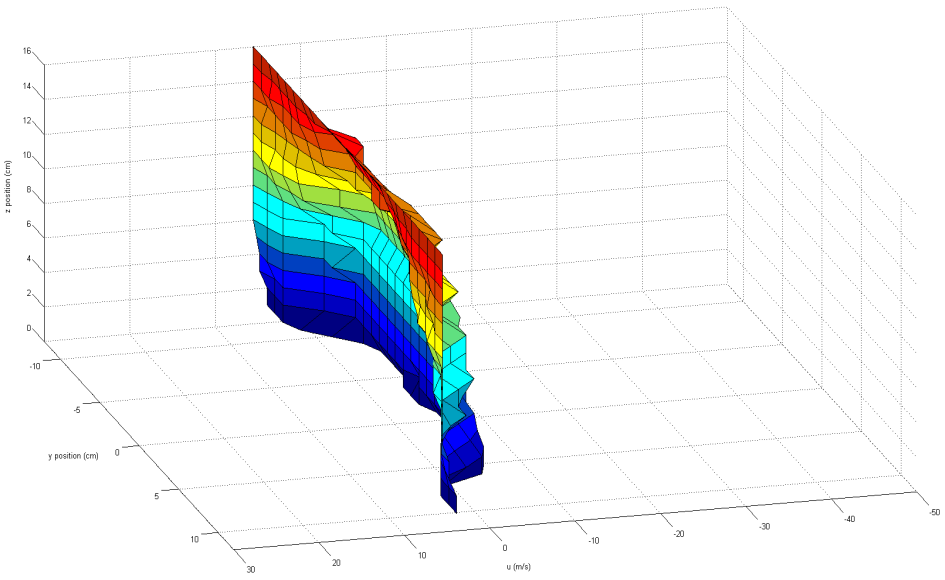

Figure 6.22: u vs y,z plot for U=5.26 m/s, at x=10 cm

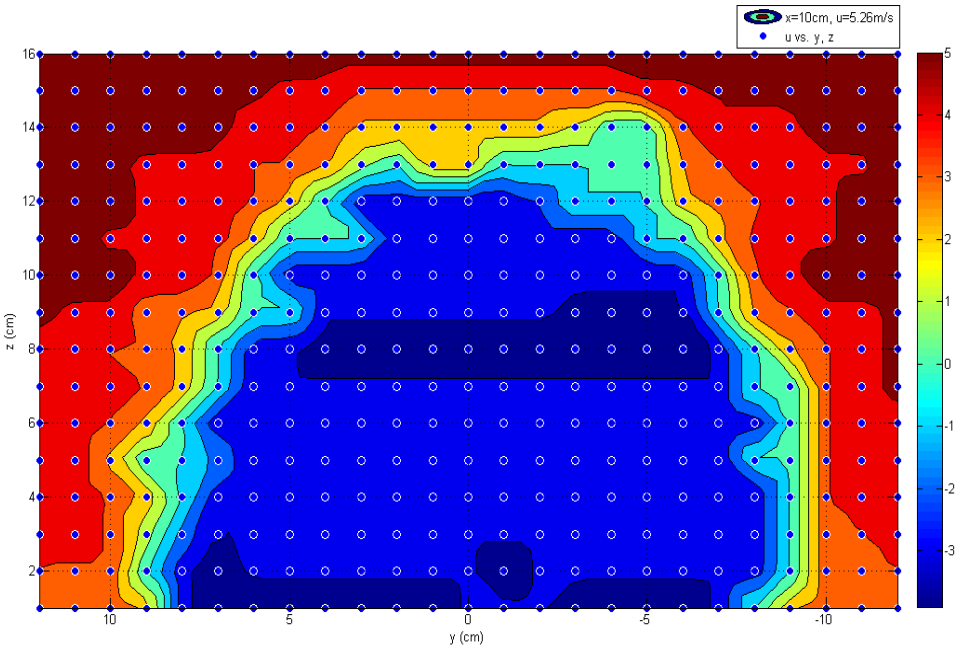

Figure 6.23: Contour plot for U=5.26 m/s, at x=10 cm

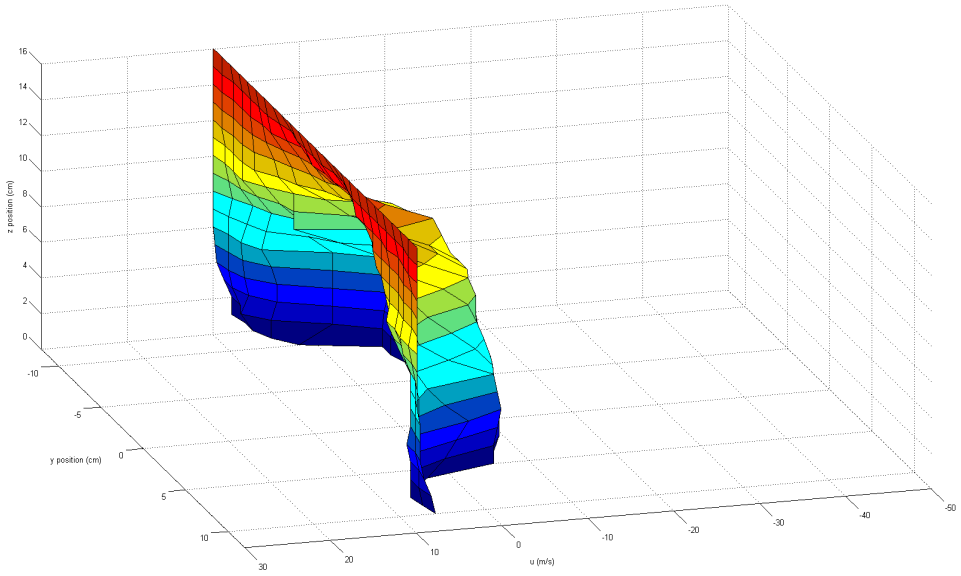

Figure 6.24: u vs y,z plot for U=9.96 m/s, at x=10 cm

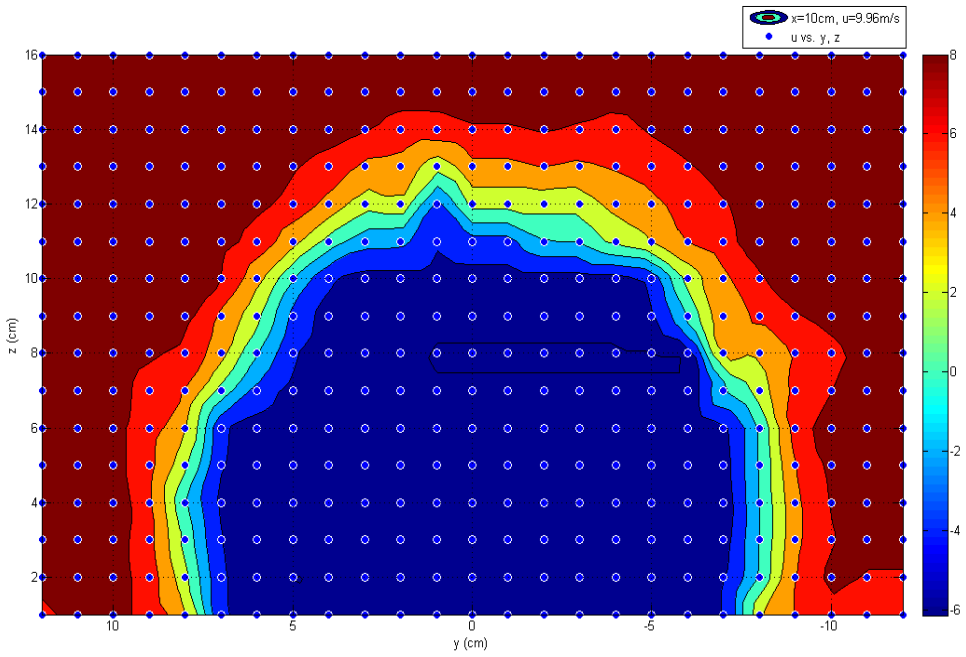

Figure 6.25: Contour plot for U=9.96 m/s, at x=10 cm

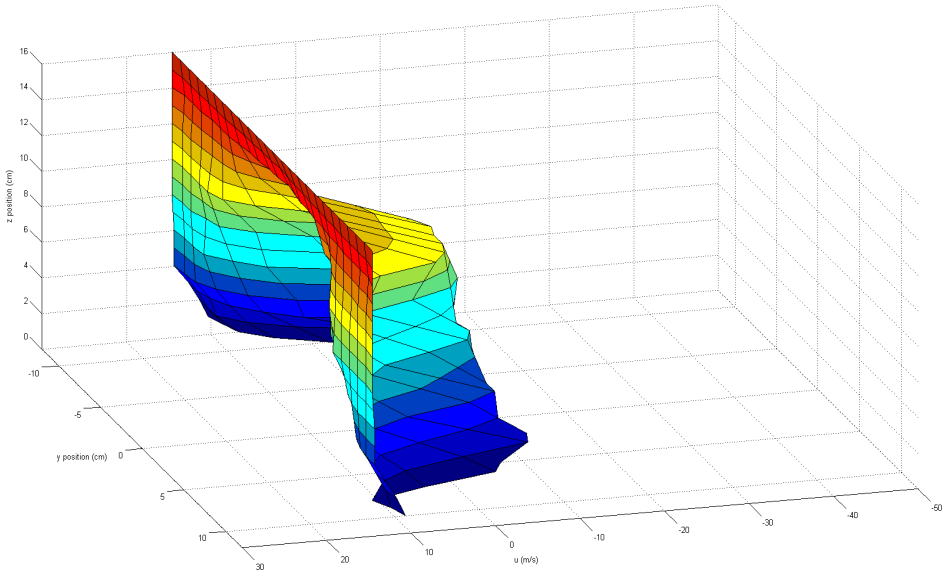

Figure 6.26: u vs y,z plot for U=14.59 m/s, at x=10 cm

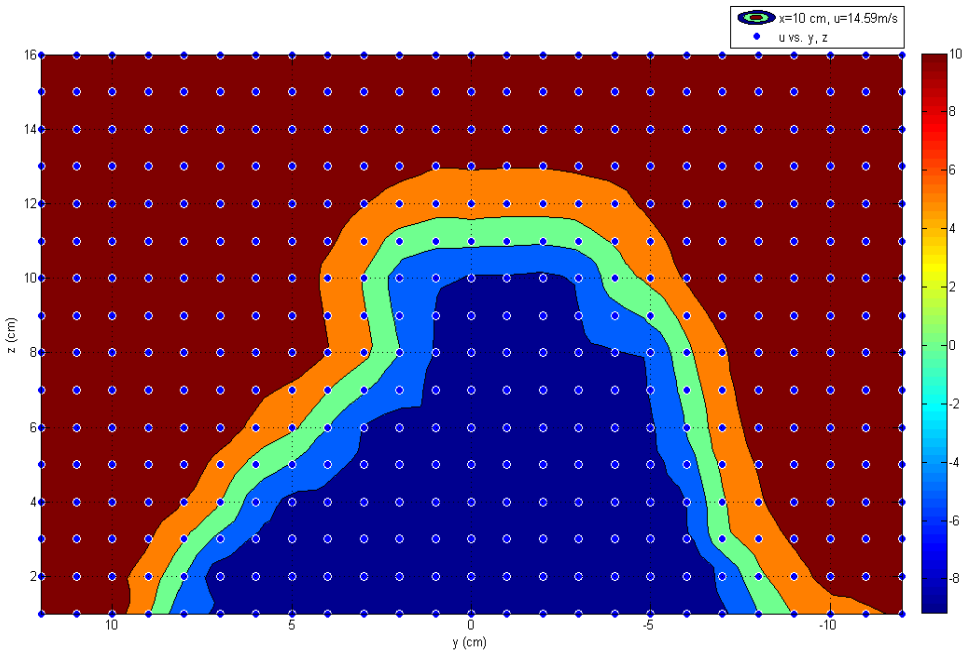

Figure 6.27: Contour plot for U=14.59 m/s, at x=10 cm

It is worthy to say that although negative flow velocities are still observed, partial positive flow regions located in negative flow region are not seen anymore which can be associated with increasing distance from model. Vortices and flow irregularities also has no more dominancy over the flow. However, an unexpected result of U=14.59 m/s case is encountered for this y-z plane. Wake locations which must have velocity values close to free stream value doe not converge to 14.59 m/s as seen. They have the level of 10 m/s. This is most probably a processing error. During post process of the velocity data for contour plot, it arises since surface plot seems normal.

6.2.1.5 Results of x=13 cm

Surface and contour plots of three different free velocities are represented in following figures.

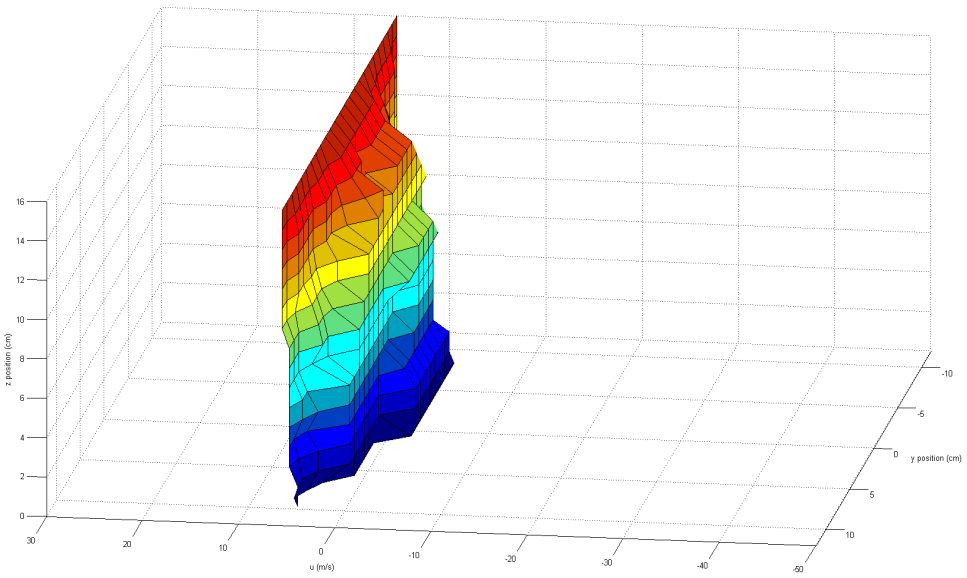

Figure 6.28: u vs y,z plot for U=5.26 m/s, at x=13 cm

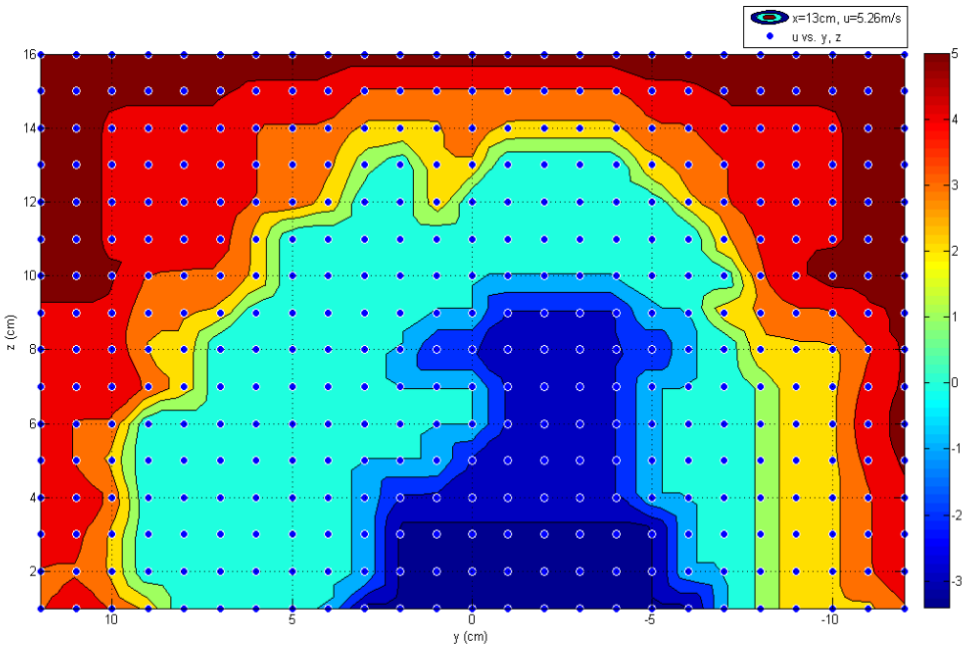

Figure 6.29: Contour plot for U=5.26 m/s, at x=13 cm

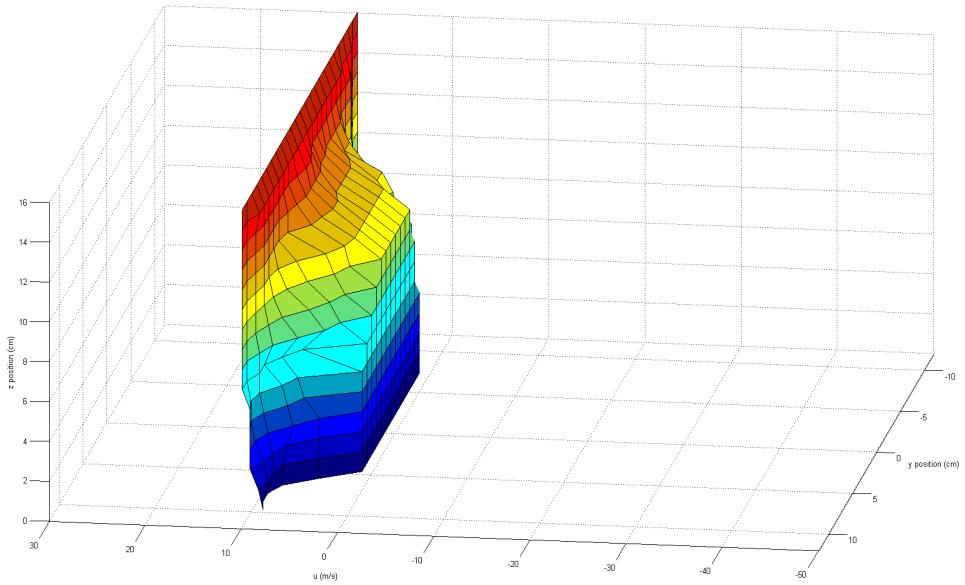

Figure 6.30: u vs y,z plot for U=9.96 m/s, at x=13 cm

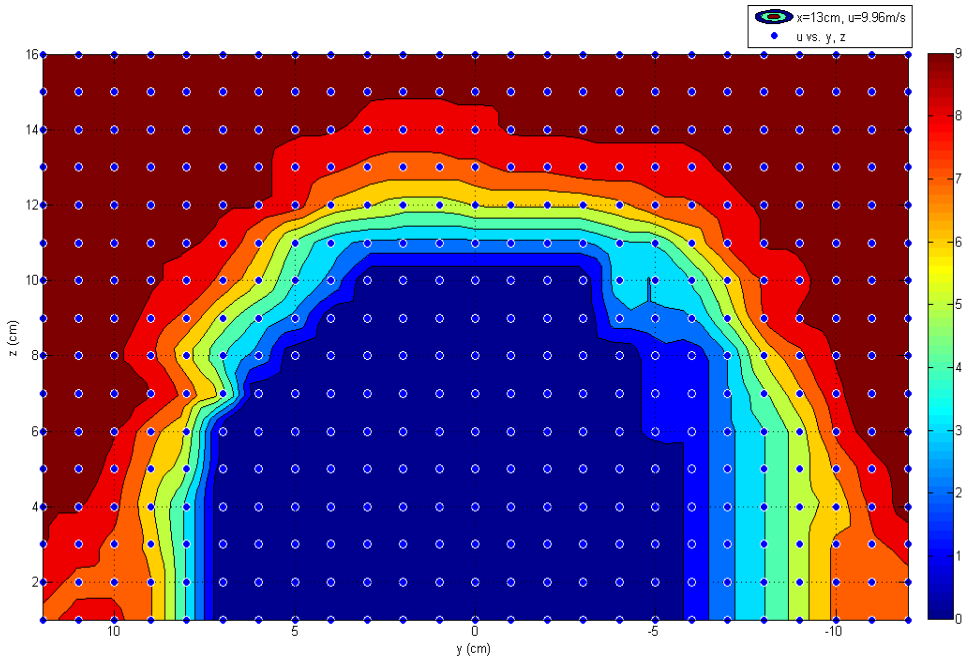

Figure 6.31: Contour plot for U=9.96 m/s, at x=13 cm

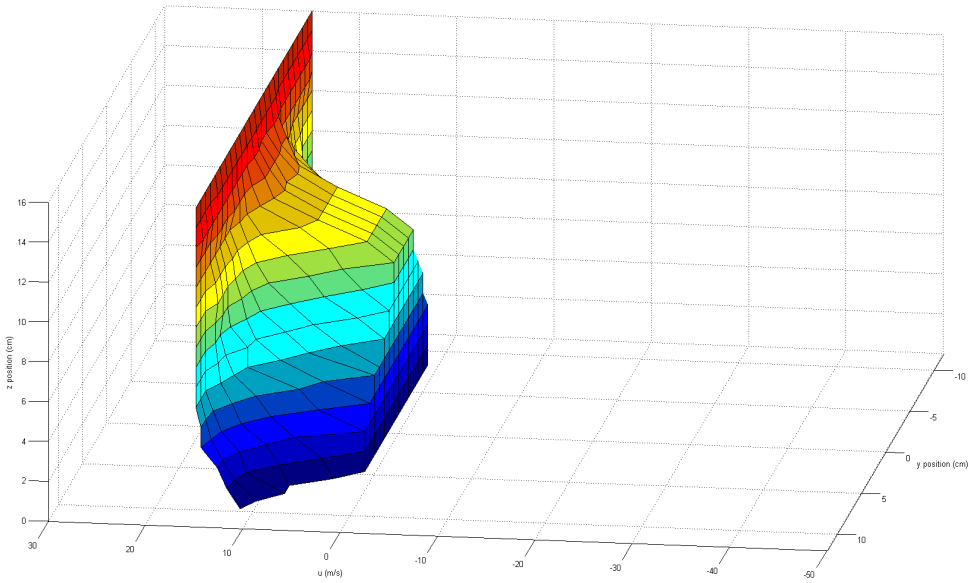

Figure 6.32: u vs y,z plot for U=14.59 m/s, at x=13 cm

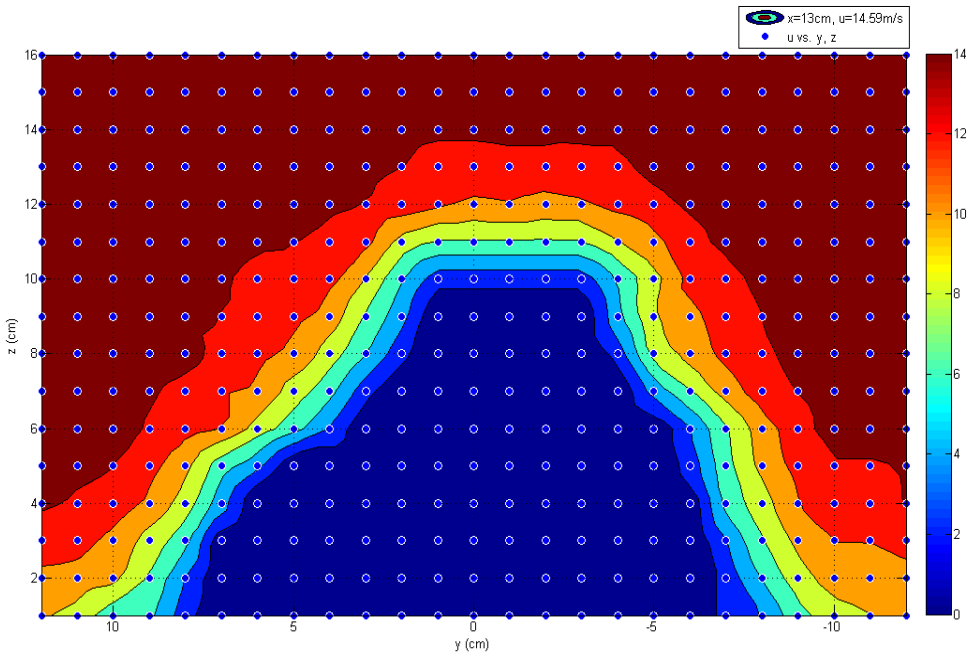

Figure 6.33: Contour plot for U=14.59 m/s, at x=13 cm

For this plane, flow velocities in wake region are higher than previous y-z plane for all cases. Negative values of flow velocities are not seen for U=14.59 m/s. Irregularities of flow are not seen for higher velocities. Wake characteristics of different free stream flows have a tendency to be stable.

6.2.1.6 Results of x=16 cm

Surface and contour plots of three different free velocities are represented in following figures.

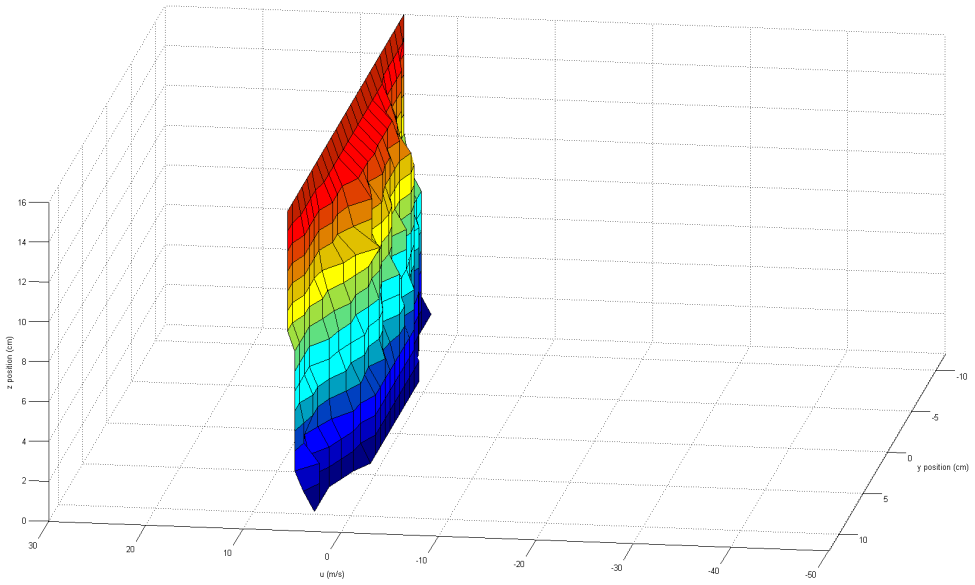

Figure 6.34: u vs y,z plot for U=5.26 m/s, at x=16 cm

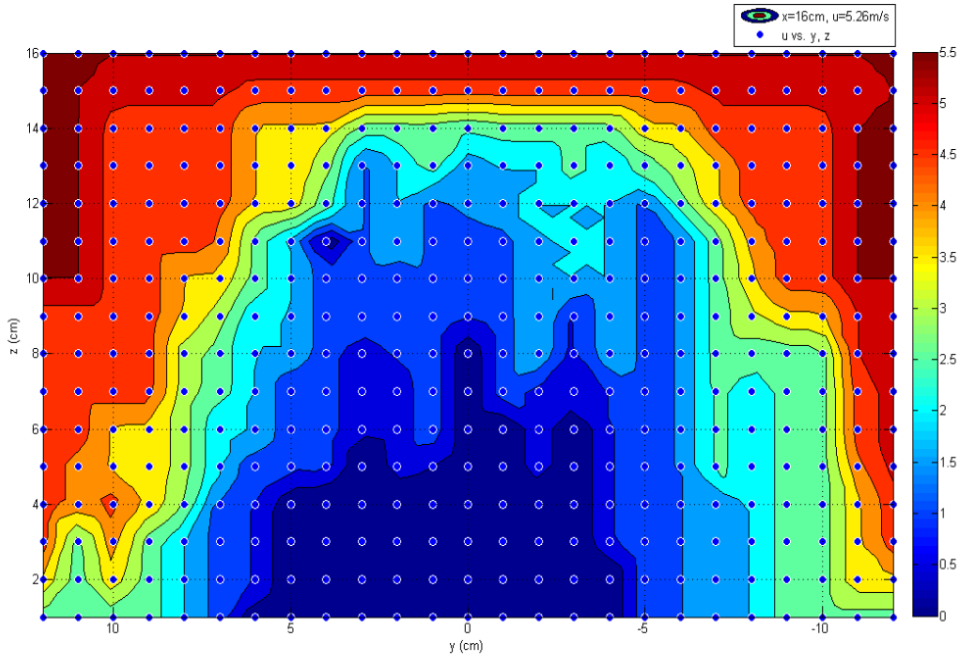

Figure 6.35: Contour plot for U=5.26 m/s, at x=16 cm

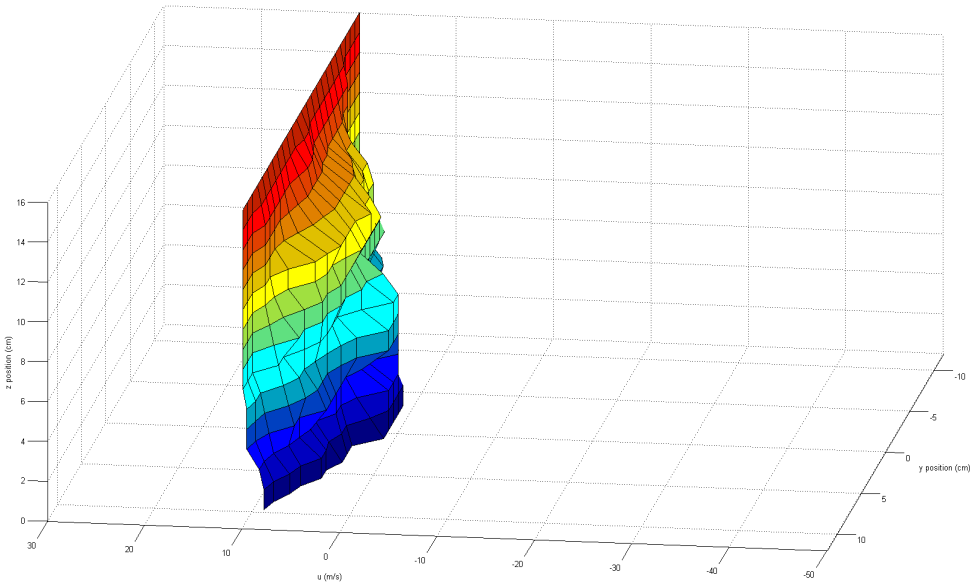

Figure 6.36: u vs y,z plot for U=9.96 m/s, at x=16 cm

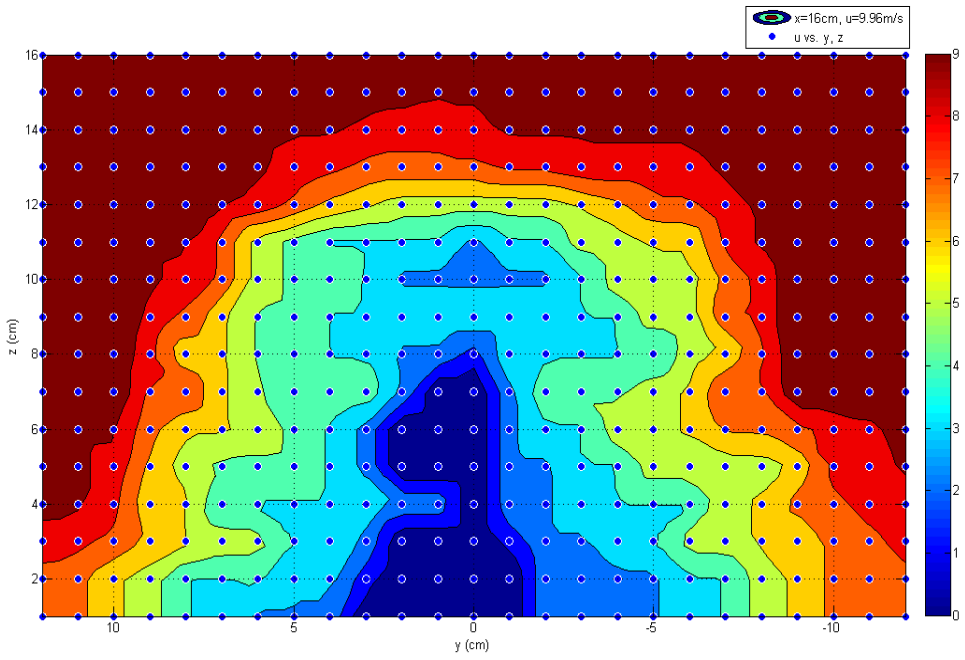

Figure 6.37: Contour plot for U=9.96 m/s, at x=16 cm

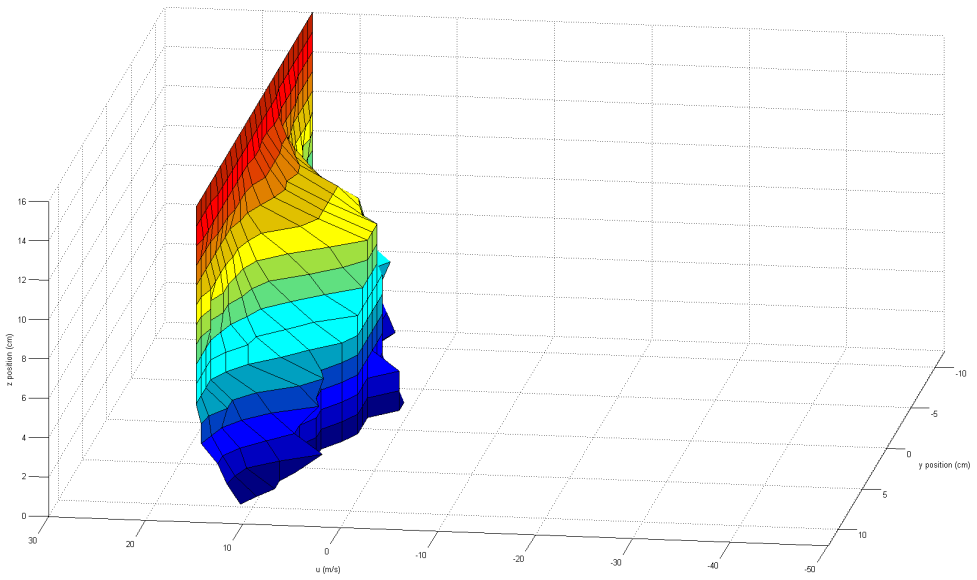

Figure 6.38: u vs y,z plot for U=14.59 m/s, at x=16 cm

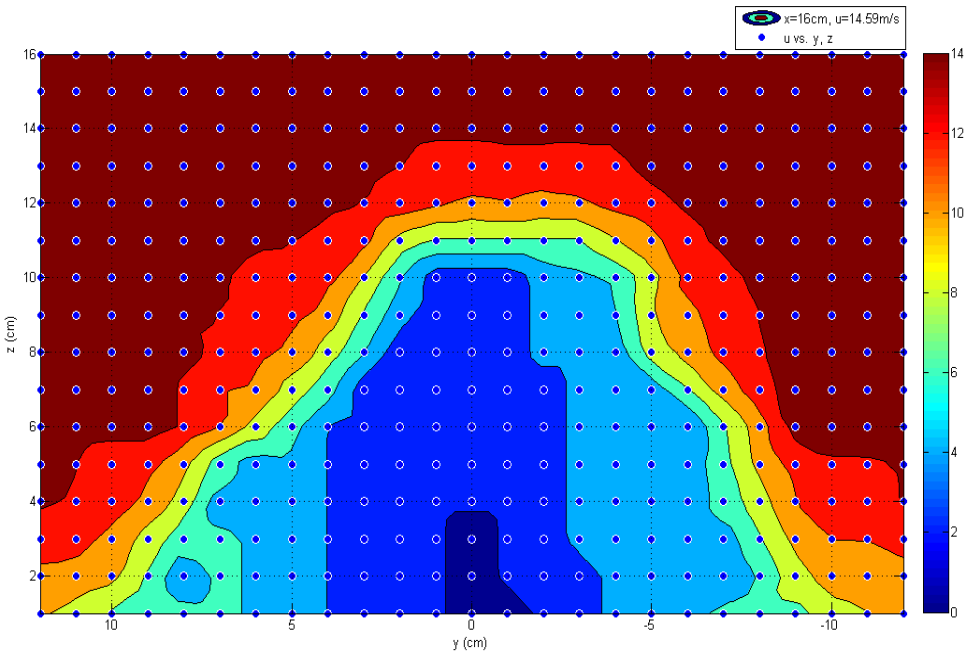

Figure 6.39: Contour plot for U=14.59 m/s, at x=16 cm

Flow velocities in the wake region are positive for all free stream conditions. However, fluctuations and the irregularities return partially for U=5.26 m/s and 9.96 m/s. Actually, this is an unexpected situation for this distance. For the highest velocity, flow characteristics are nearly fixed.

6.2.1.7 Results of x=20 cm

Surface and contour plots of three different free velocities are represented in following figures.

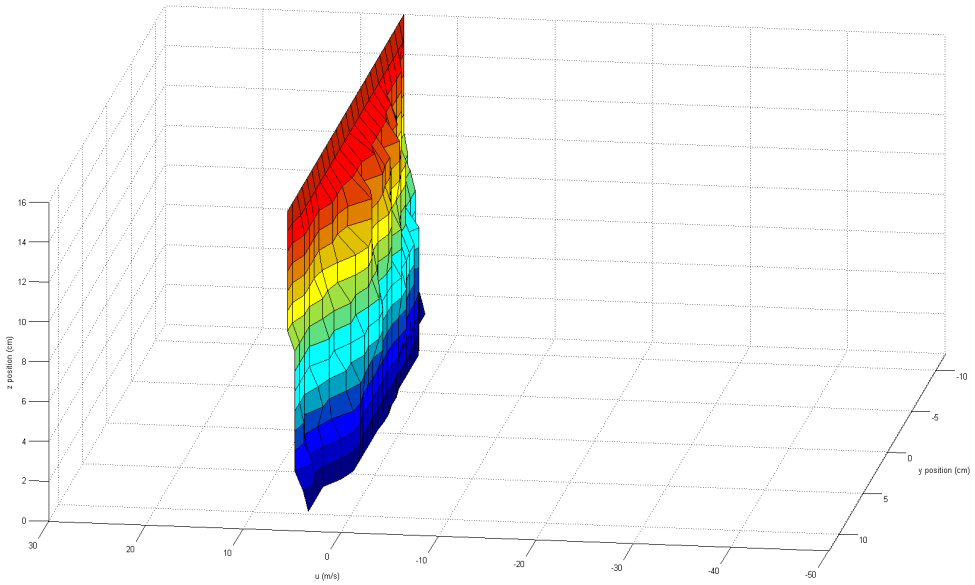

Figure 6.40: u vs y,z plot for U=5.26 m/s, at x=20 cm

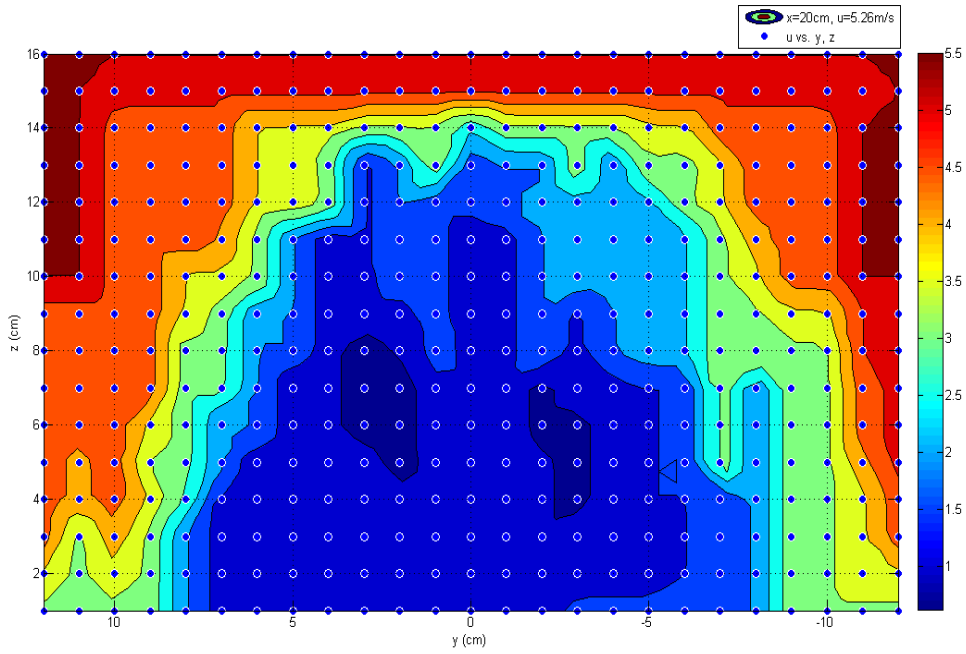

Figure 6.41: Contour plot for U=5.26 m/s, at x=20 cm

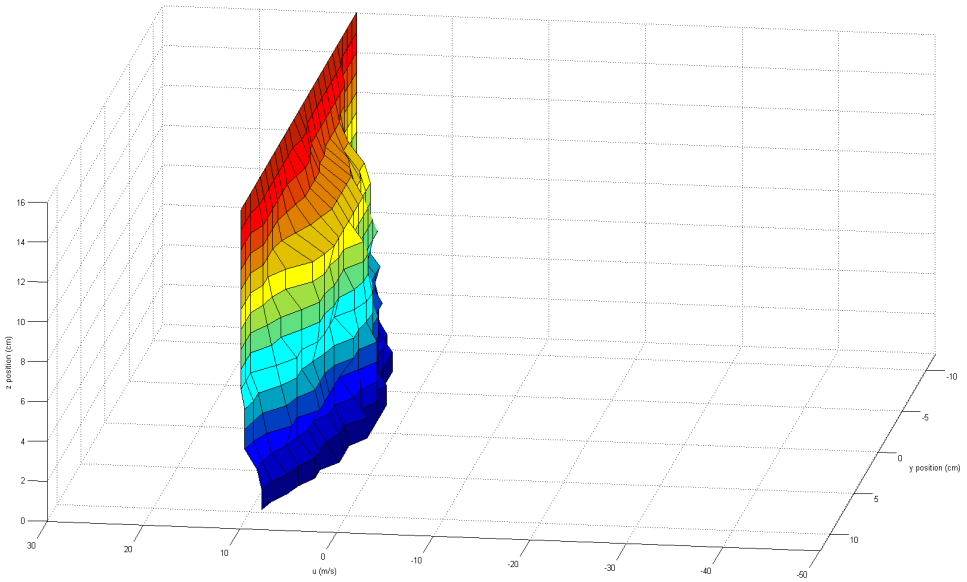

Figure 6.42: u vs y,z plot for U=9.96 m/s, at x=20 cm

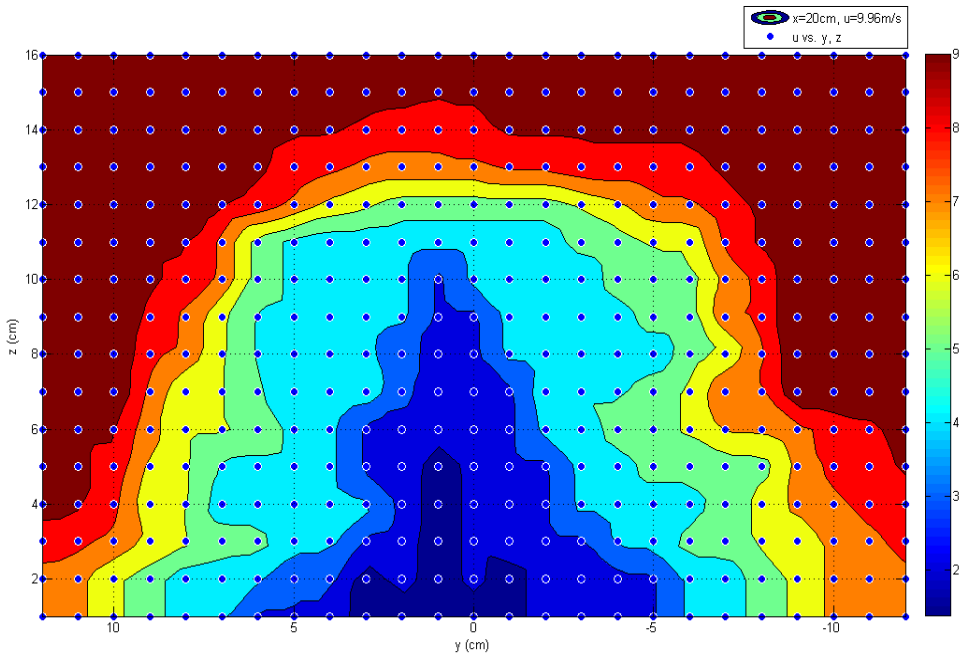

Figure 6.43: Contour plot for U=9.96 m/s, at x=20 cm

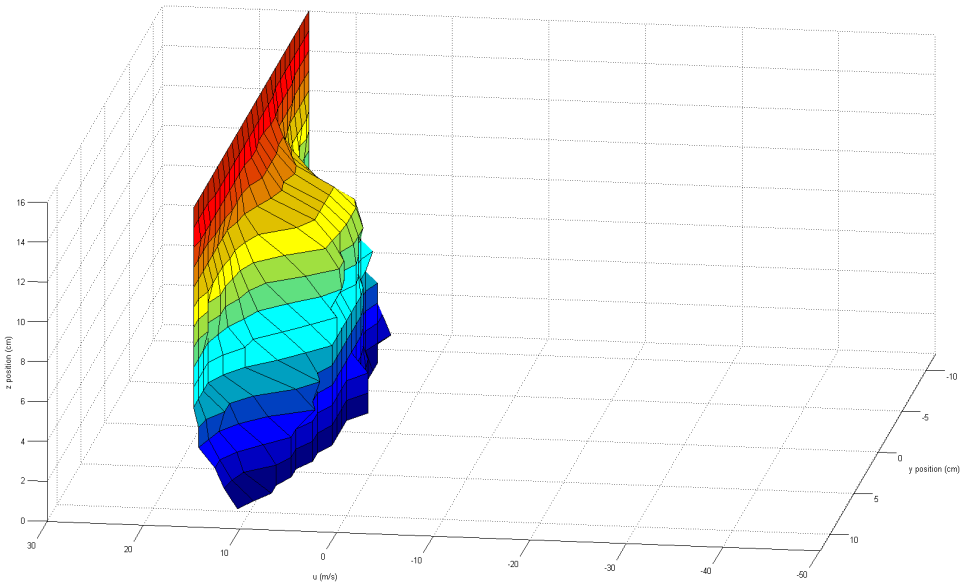

Figure 6.44: u vs y,z plot for U=14.59 m/s, at x=20 cm

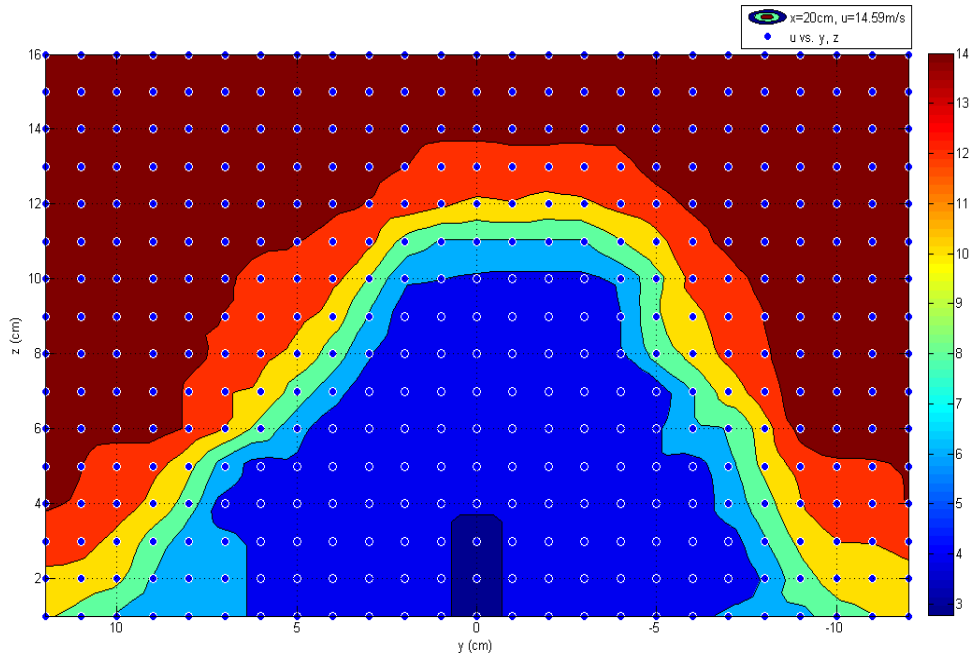

Figure 6.45: Contour plot for U=14.59 m/s, at x=20 cm

This plane is the seventh y-z plane and thus, the final plots are presented. Flow velocities in the wake region are still positive for all free stream conditions. However, fluctuations and the irregularities are still partially valid for U=5.26 m/s. Flow characteristics of all free stream cases seem to be fixed. This work is useful in terms of analyzing and learning the wake region characteristics for different distances from the body. This will give a reasonable sense for estimating the drag force by utilizing the wake integration method.

6.2.2 Drag force estimations with the wake integration method

In this part, the equation used in the drag force estimation is given. Then, related results are shown and discussed.

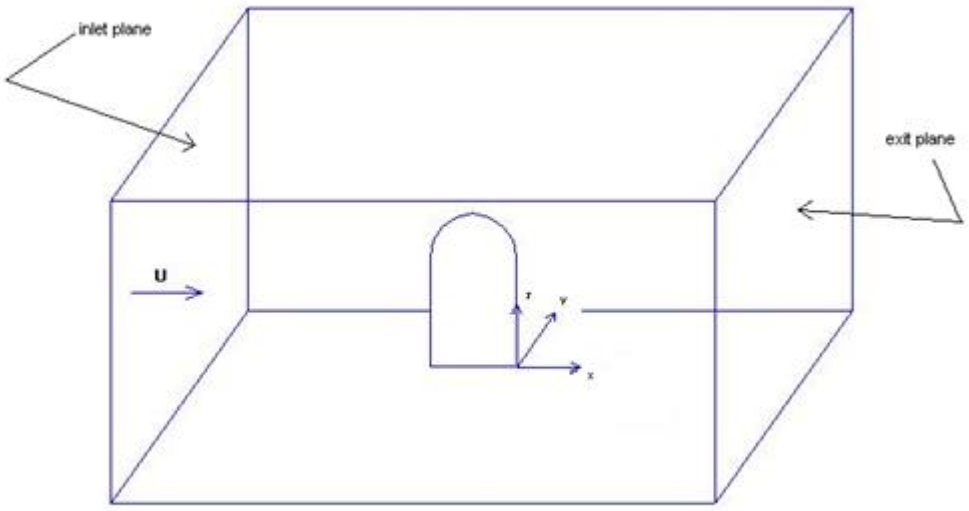

Figure 6.46: Simple representation of the control volume and the body

Equation used for calculating the drag force on the gimbal body is deducted simply from the principle of conservation of linear momentum. A control volume covering the body is determined as seen in Figure 6.46. It is not very hard to apply the conservation of momentum to the control volume whose inlet and outlet planes are

definite. Total force acting on the control volume is the sum of surface forces including the pressure forces. It also equals the net momentum flux of the control volume. Total force exerted on the control volume is:

$$\Sigma F = \Sigma F_{surface} + \Sigma F_{ext} \tag{6.1}$$

and

$$\Sigma \vec{F} = \iint_S \rho \vec{V}(\vec{V}.\vec{n}) dS \tag{6.2}$$

where $\Sigma F_{surface}$ is the total surface forces exerted on the control volume and its boundaries, ΣF_{ext} stands for gravity and electro-magnetic forces, also called body forces, acting on the fluid particles within the control volume. No body force exerts the fluid particles of the control volume. Hence, it can be considered that $\Sigma F_{ext} = 0$. Then the force equality on the control volume can be written as:

$$R + \iint_S -p\,\vec{n}\,dS = \iint_S \rho \vec{V}(\vec{V}.\vec{n}) dS \tag{6.3}$$

where R is the total reaction force exerted by the body in control volume on the fluid. Second term in equation (6.3) stands for pressure forces.

Drag force, D equals to x component of the total reaction force, R. But, directions of the forces are opposite to each other. Then drag force becomes:

$$-D + \iint_S -p\,\vec{n}\,dS = \iint_S \rho \vec{U}(\vec{U}.\vec{n}) dS \tag{6.4}$$

By using equation (6.4, the drag force exerted on the gimbal is written as:

$$D = \iint_{S_i} p_i dydz - \iint_{S_e} p_e dydz + \iint_{S_i} \rho U_\infty^2 dydz - \iint_{S_e} \rho u^2 dydz \qquad (6.5)$$

In this equation, first and second terms stand for pressure forces. Others are the flux terms. Then, the equation comes to a form of:

$$D = p_i A_i - p_e A_e + \rho U_\infty^2 A_i - \rho \int_{z_1}^{z_2} \int_{y_1}^{y_2} u^2(y,z)\, dydz \qquad (6.6)$$

where p_i is pressure of the inlet, p_e is pressure of the exit, U_∞ is free-stream velocity, u is the velocity at the exit plane, wake plane, also expressed as the function form u(y,z), A_i is the inlet area, A_e is the exit area, y_1 and y_2 are integration limits on y-plane, z_1 and z_2 are integration limits on z-plane.

Inlet and exit pressures and free-stream velocity can be easily measured and directly used in the above equation. However, the action is not simple for the velocity at the exit plane. For the evaluation of the last term in equation (6.2) velocity profile must be obtained for the exit plane, actually the wake region, determined earlier. Velocity profiles obtained and shown in previous part for seven different wake planes are used for the calculation of the drag force. Velocity functions arising from surface fits to the experimental data via Matlab are used as u(y,z) in the integration term of the drag force equation (6.2).

Estimated drag forces and comparison of them with measured drag forces via the load-cell is presented in Tables 6.2, 6.3 and 6.4.

Table 6.2: Drag estimation for free stream velocity of 5.26 m/s

CV exit planes	Estimated drag force (N)	Measured drag force by load-cell (N)	Percent difference %
x=1 cm	0.91	0.42	115
x=4 cm	0.92		118
x=7 cm	1.04		147
x=10 cm	1.03		145
x=13 cm	1.60		282
x=16 cm	1.59		279
x=20 cm	1.36		223

Table 6.3: Drag estimation for free stream velocity of 9.96m/s

CV exit planes	Estimated drag force (N)	Measured drag force by load-cell (N)	Percent difference %
x=1 cm	3.43	1.29	165
x=4 cm	3.18		146
x=7 cm	3.01		133
x=10 cm	2.28		76.7
x=13 cm	2		55
x=16 cm	1.63		26.4
x=20 cm	1.51		17

Table 6.4: Drag estimation for free stream velocity of 14.59 m/s

CV exit planes	Estimated drag force (N)	Measured drag force by load-cell (N)	Percent difference %
x=1 cm	2.23	2.46	9.3
x=4 cm	3.03		23.2
x=7 cm	3.55		44
x=10 cm	4.27		73.6
x=13 cm	3.03		23.2
x=16 cm	2.84		15.4
x=20 cm	2.77		12.6

According to the results shown in tables, applied wake integration method does not give accurate results generally. Therefore, it cannot be classified as successful totally. Especially for low free stream velocity, its percentage difference of estimation is very huge that the results obtained by the method are nonsense. It is not expected to give good results for wake planes very close to the body naturally. However, moving away from the body as a wake plane does not contribute anything and unfortunately, percent differences increase as the distance from the body increases. The main reason for unsuccessful estimation of the drag force is most probably that selected exit planes of the control volume are not far enough for low free stream velocities. In fact, it is considered that for low free stream velocities it can be difficult to have regular flow after the immersed body. On the other hand, the reason of such a huge difference can be nonconformity of the applied wake integration method for wakes of low free stream velocities. Additionally, velocity functions for exit planes coming from surface fittings are another error source. At some points it is very successful and covers measured values. However, at some different points it undershoots or overshoots and this can be taken into consideration as another factor of big differences.

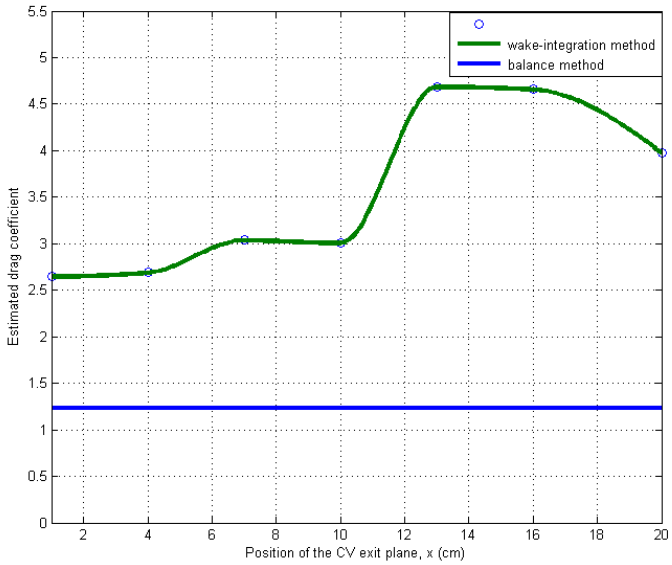

Figure 6.47: Variation of drag coefficient with the exit plane of control volume for U=5.26 m/s

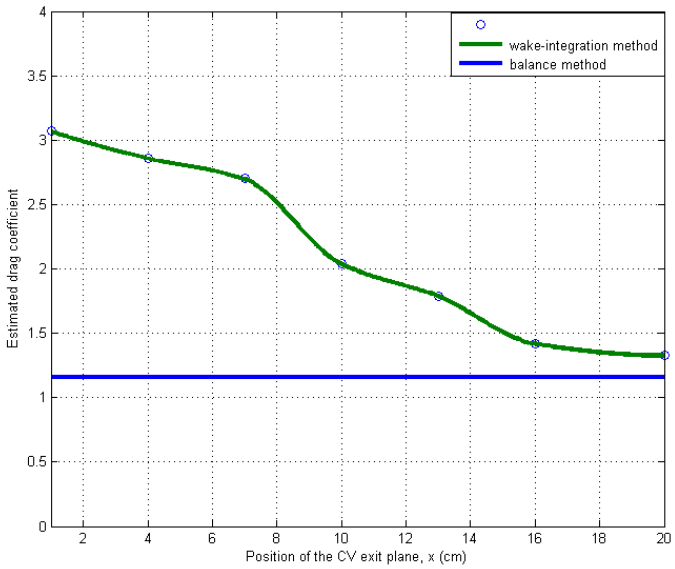

Figure 6.48: Variation of drag coefficient with the exit plane of control volume for U=9.96 m/s

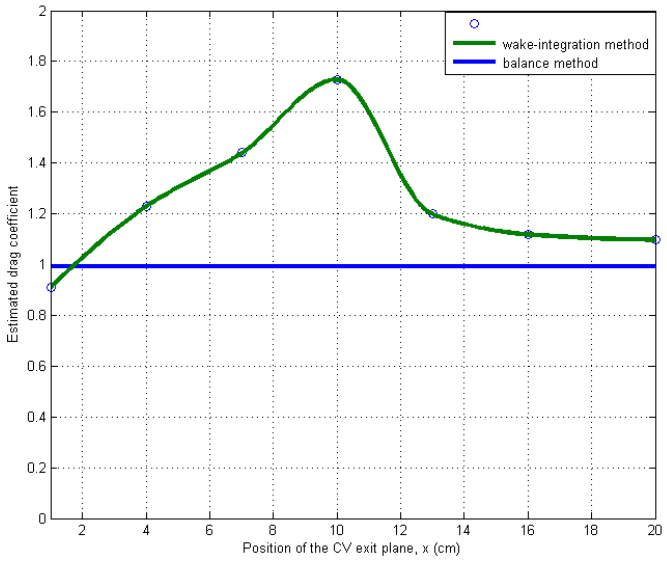

Figure 6.49: Variation of drag coefficient with the exit plane of control volume for U=14.59 m/s

Nevertheless, drag force prediction results for moderate and relatively high free stream velocities are encouraging. It is not possible to obtain good estimation results for the wake regions close to the body apparently since the flow characteristics are very chaotic. Vortices, backflows and flow irregularities create an obstacle for the use of wake integration method. However, progressively results of estimation come to the rational levels. Difference from load-cell drag force results of estimation decreases gradually with increasing distance to the body for moderate free stream velocity. Therefore, farther wake planes than x=20 cm have a possibility of giving better results. Nonetheless, amount of difference of x=20 cm for moderate free stream velocity case can be regarded as acceptable.

In fact, the method is the most successful for the relatively high free stream velocity case. Except close planes to the body, results are regular. Actually, in x=1cm plane there is a perfect estimation of drag force. However, this is a misleading result since this plane has the most chaotic flow characteristics. Therefore, this must be interpreted as a coincidence. Results of far planes as x=16 cm and 20 cm show that these planes are proper for ending the control volume for successful prediction of drag. Nevertheless, examining farther planes than x=20 cm can be useful for better accuracy. In addition, momentum flux term, which is last integral term in equation (6.6), can be calculated by numerical methods since necessary data is exit velocities of y-z planes and it is measured. In Appendix D, numerical approach for drag force calculation and examination for one plane can be found.

6.3 Turbulence levels of y-z planes

Turbulence level in wake region is surveyed for three free stream velocities for which drag is estimated by wake integration method. Actually, obtained values thought as turbulence intensity levels are u_{rms}/U_{mean} values since LDA used in experiments measures only x velocities of the flow. Therefore, these are u_{rms}/U_{mean} values. In fact, u_{rms}/U_{mean} can give information about flow characteristics like

turbulence intensity levels. They are not same properties but, they are similar properties. Wake planes in previous parts are used repeatedly. Measurement location is the origin of y axis with z=13 cm on y-z planes.

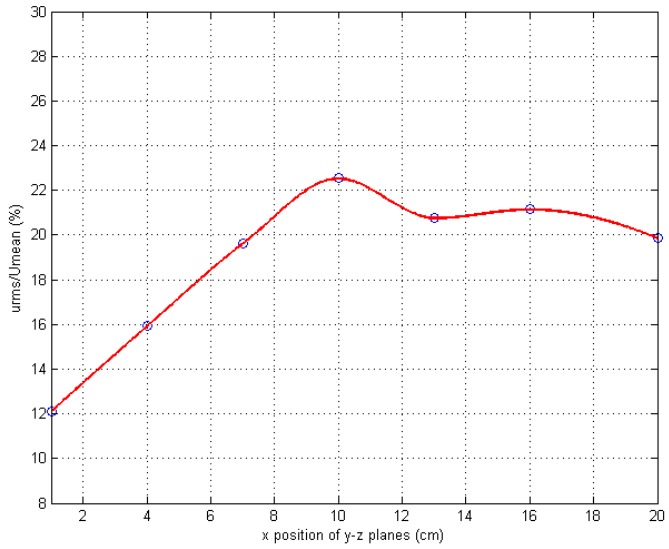

Figure 6.50: Variation of u_{rms}/U_{mean} level with x position of y-z planes for U=5.26 m/s

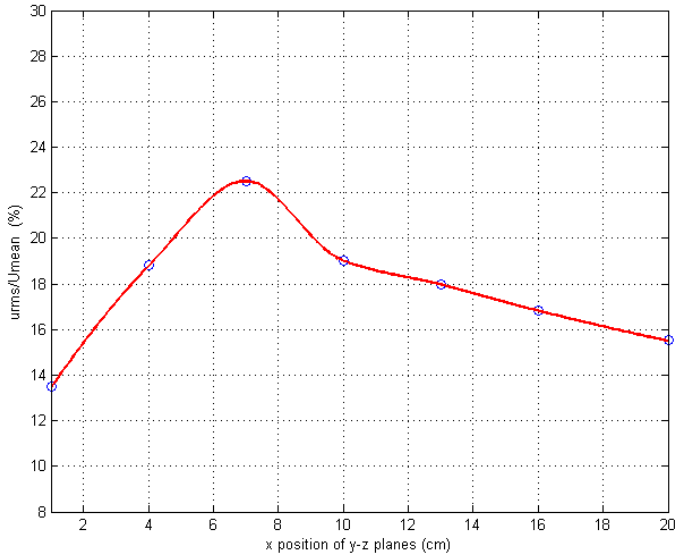

Figure 6.51: Variation of u_{rms}/U_{mean} level with x position of y-z planes for U=9.96 m/s

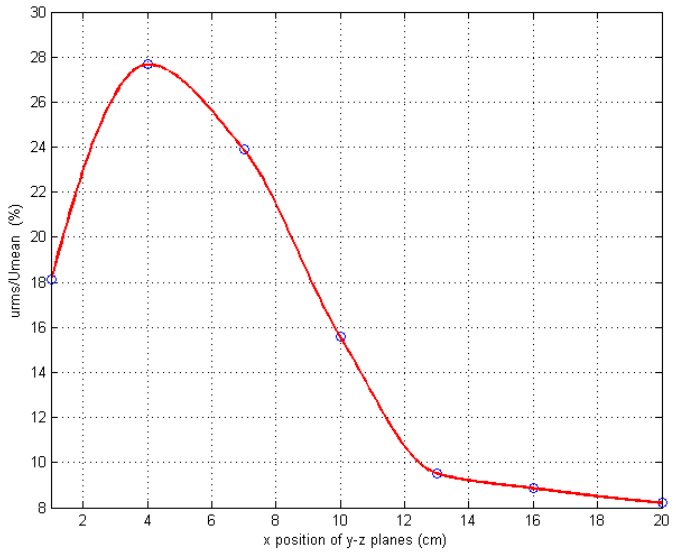

Figure 6.52: Variation of u_{rms}/U_{mean} level with x position of y-z planes for U=14.59 m/s

Above plots are useful for examining the flow in wake region. u_{rms}/U_{mean} levels of three different velocities for different y-z planes give a view related to previous parts. For U=5.26 m/s, turbulence level is high totally. For further planes from the body, it is still high. This can be an evidence of very huge differences from load-cell results in drag estimation results by wake integration method for this free stream velocity. u_{rms}/U_{mean} level is in a descending trend for higher free stream velocities. It has relatively moderate levels in further planes from the body for U=9.96 m/s. For U=14.59 m/s, u_{rms}/U_{mean} level has a top around x=4 plane and decreases continuously to the low values. This is also interpreted as matching up with drag estimation results by momentum method. As u_{rms}/U_{mean} decreases, estimated differences of drag force also decreases.

6.4 Flow visualization

For flow visualization some images are taken. By the help of the smoke generator and laser beam some y-z planes are examined. Flow at these planes is visualized.

However, some shortcomings have experienced. So, desired images for flow visualization cannot be captured.

Actually, the plan was performing flow visualization for different values of free stream velocities. But, it cannot be achieved since the CO_2 smoke scatters for even very low velocities. Therefore, all images are taken for free stream velocity of 2.20 m/s. Images for higher velocities than 2.20 m/s cannot be taken. Also images are not taken from the same reference point since nothing can be visualized for some y-z planes at the same reference point. Decreasing quantity of the smoke by the time due to choking of CO_2 tubes with oily remnants is another factor which gets flow visualization harder.

For the following three images, the camera is placed at nearly same place. It is located at left side and approximately 40 cm behind the body according to flow direction. Three images of close planes to the body can be seen in Figure 6.53, 6.54 and 6.55.

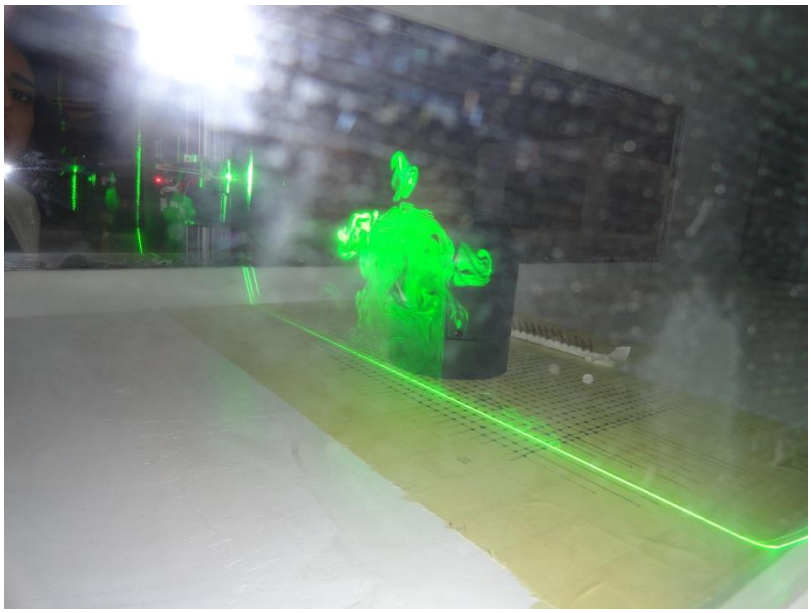

Figure 6.53: Image of y-z plane 1 cm behind the body

Figure 6.54: Image of y-z plane 3 cm behind the body

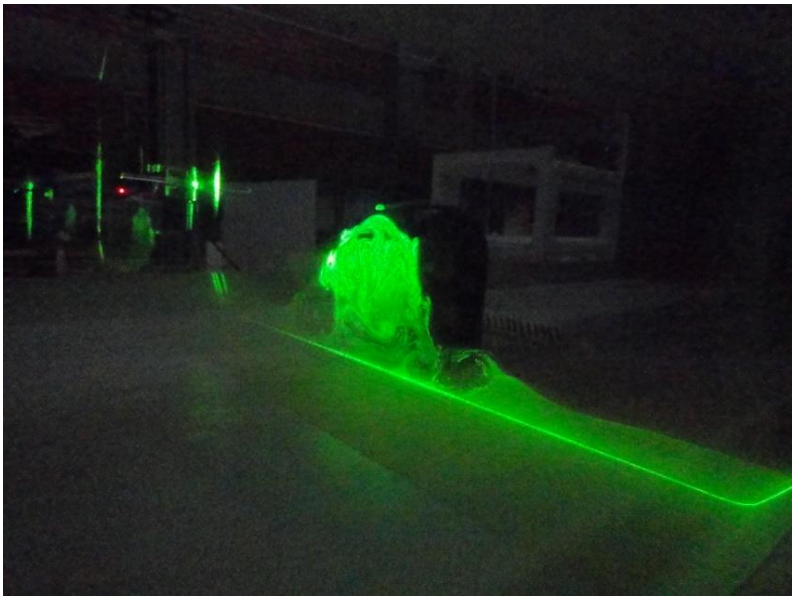

Figure 6.55: Image of y-z plane 5 cm behind the body

Generally flow behind the body can be seen for close planes. For Figure 6.53, an extra vortex on the top of the body is remarkable. Except this, Figure 6.54 and 6.55 images are alike and on the left side of the body according to flow direction vortices are more distinctive.

For further planes behind the body flow visualization gets harder since smoke become almost invisible. So, flow visualization for further planes is not successful and sufficient. Following figures are obtainable ones. For Figure 6.56, the camera is placed at the right side and nearly 40 cm behind the body according to flow direction.

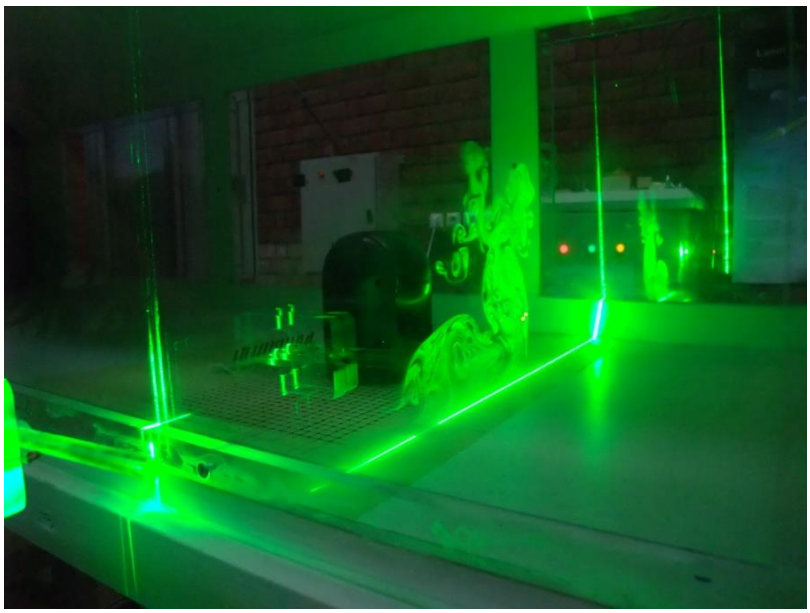

Figure 6.56: Image of y-z plane 12 cm behind the body

For Figure 6.57, 6.58 and 6.59, the camera is placed at right side and in front of the body.

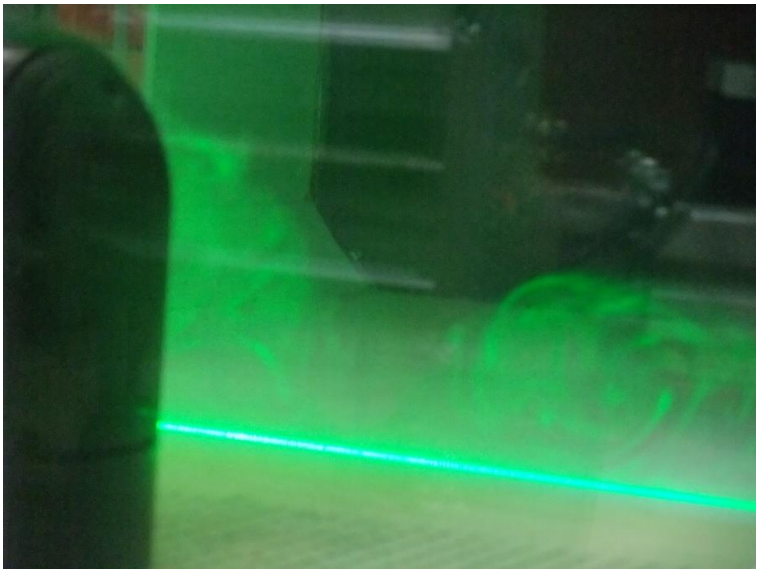

Figure 6.57: Image of y-z plane 14 cm behind the body

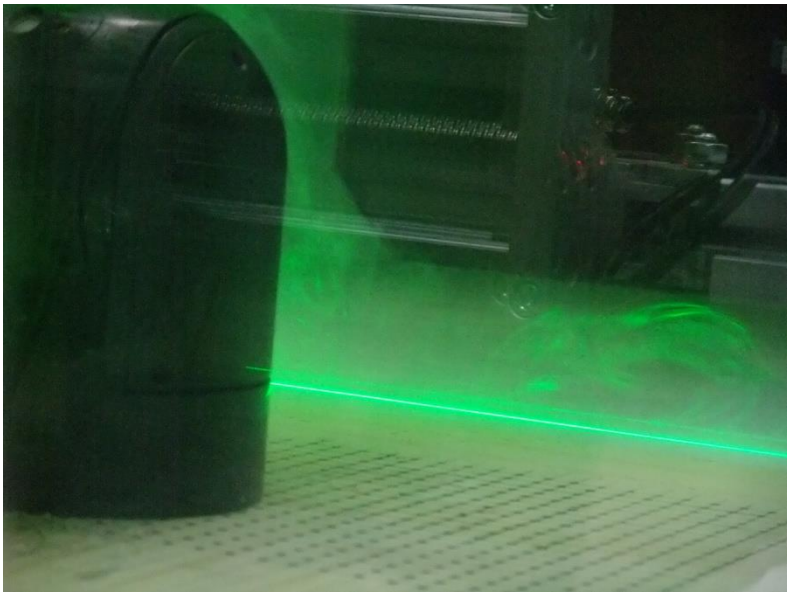

Figure 6.58: Image of y-z plane 16 cm behind the body

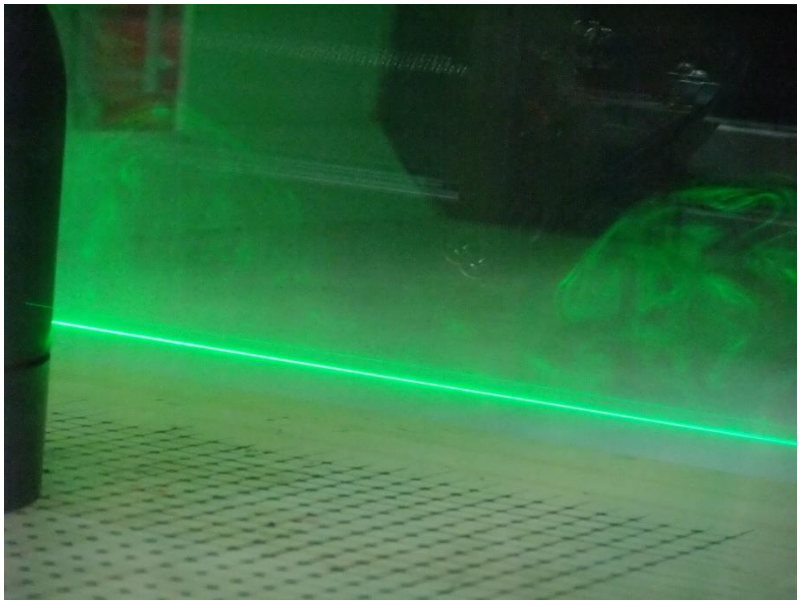

Figure 6.59: Image of y-z plane 20 cm behind the body

Vortex formations on the further planes can be seen even though they are not very clear. They are bigger vortices compared to vortices seen on close planes to the body. The clearest image of further planes is shown in Figure 6.56. Chaotic characteristics of flow and irregular vortices are remarkable.

Finally flow is visualized for planes intersecting the body at different x locations. Camera location is on the right side and in front of the body.

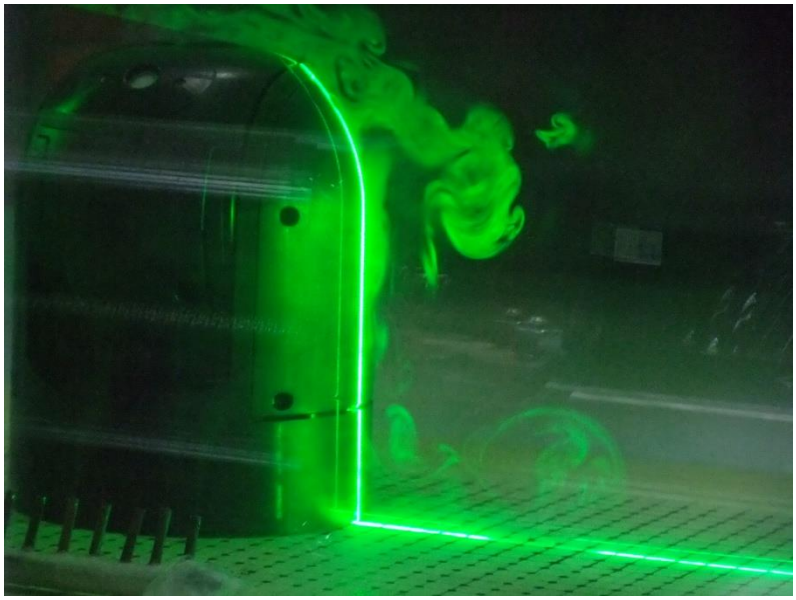

Figure 6.60: Image of y-z plane intersecting the middle plane of the body

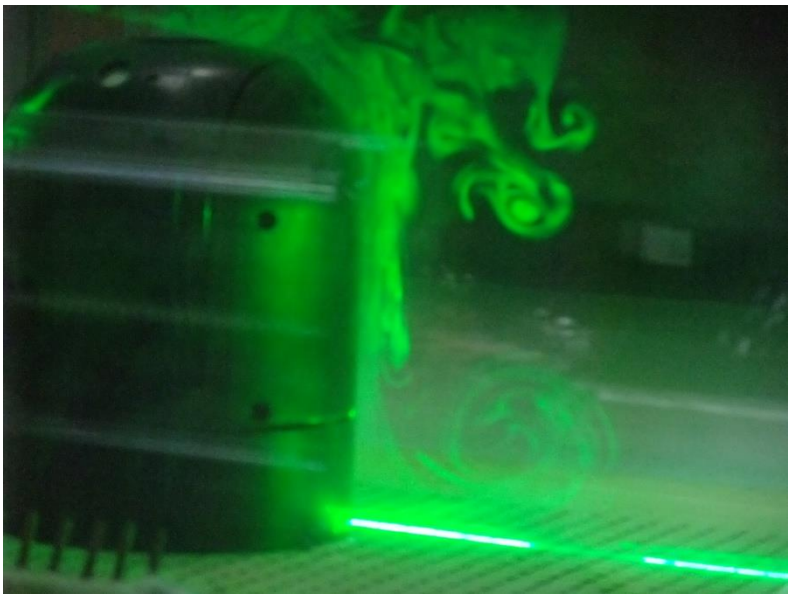

Figure 6.61: Image of y-z plane intersecting the body at 3 cm behind the middle plane

Flow visualization gives a general idea about the flow over the body and is useful for some points. However, it must be accepted that it is unsuccessful part of experiments. Problems due to the instrumentation and lack of experience are encountered. The plan was to perform a systematical process of flow visualization. Flow visualization of different y-z planes for free stream velocities varying from low velocities to high velocities gradually is the actual process which is planned. The camera must be positioned at the same location for all images since comparing images is a significant action. Owing to these reasons, flow visualization part of experiments can be thought as unsatisfying.

CHAPTER 7

SUMMARY AND CONCLUSION

This thesis study aimed to investigate drag coefficient and drag force acting on a mini gimbal system in a free flight. Mini gimbal is a payload system that is carried by mini UAVs generally. In this respect, obtaining the drag force exerted on mini gimbal system and general flow characteristics over the gimbal body were significant steps and experimental study related to these concerns was planned.

Two methods were used to obtain the drag force on the gimbal system. First method was direct measurement of the drag force with balance system in the wind tunnel. For this purpose, it was necessary to use convenient balance system for the tested body. Thus, a load-cell was designed firstly. The load-cell designed for this specific task was produced. After that, drag force measurements were performed.

Drag force were measured for various Reynolds number values, thereby free stream velocities varying from 5.26 m/s to 20.06 m/s, in the suitable working range of the wind tunnel. For ten different Reynolds numbers, drag coefficients were calculated. Relation between Reynolds number and drag coefficient was worked out. Reynolds number vs. drag coefficient plot was obtained. This was a significant work for the tested body, gimbal, since there wasn't any literature related to it. Therefore, results of this step were compared with results of similar bodies.

Although it was worked with ten different Reynolds number, experiments couldn't be performed for relatively high free stream conditions due to safety considerations related to the wind tunnel. All free stream velocities used in drag force measurement

experiments with the load-cell, from 5.26 m/s to 20.06 m/s, were in the interval of operating velocities of mini UAV. However, higher velocities for turbulent flow over the body weren't able to be experienced. This would be one of the remarkable steps of the experiments. Nevertheless, the load-cell design process and experiments with it were significant and drag force exerted on the body was measured and recorded successfully.

Second way for prediction drag force on the gimbal was the wake integration method. An experimental procedure was also necessary for this method. It was a combination of experiments and conservation of linear momentum principle. It was a CV analysis. Drag force expression was written for the body by using conservation of linear momentum.

For the evaluation of the drag force with this expression, some flow quantities were measured. Inlet and exit pressures, free stream velocity and exit velocity were measured for seven different y-z planes which are corresponding to exit planes of selected CV, starting from 1 cm behind the body to 20 cm behind the body. In other words, y-z planes were surveyed. Actually, the main aim of wake integration method was to determine the optimum control volume by evaluating the drag force and comparing it with known values, which are drag force measurement results of the load-cell.

Experiments and related calculations were performed for seven different y-z planes as stated before with three different free stream velocities, 5.26 m/s, 9.96 m/s and 14.59 m/s which were low, moderate and relatively high velocities. Exit velocity plots were obtained by the use of grid by grid velocity measurements for investigating general flow characteristics in the wake region of the gimbal. Flow irregularities and reverse flows were observed. Velocity data of exit planes were processed and used in drag force calculations by fitting it polynomial surface function via Matlab.

For relatively low velocities and close planes to body the drag force results had big differences from the load-cell measurements. It was interpreted that for low velocities the method would not give feasible results due to wider wake region compared to higher velocities. It was also interpreted that for close planes the method would not give reasonable results since at that regions flow was very chaotic and had irregularities due to closeness to the tested body. Another interpretation was related to evaluation of the integral consisting of the exit plane velocity. Surface function fitting sometimes might lead additional errors. Using numerical methods for the evaluation of the integral was more convenient and preferable.

At the end of experiments, some flow visuals were obtained by using smoke generator, laser beam and CCD camera. These visuals were examined with qualitative manner to see flow characteristics over the body and in the wake region of the body. For investigation purpose, some visuals were recorded.

After this thesis study, a few recommendations can be made about future works. First of all, literature is very inadequate about the gimbal body due to military usage of it. Therefore, many works related to it can arise. Drag force investigation for different positions of gimbal can be a future work since a gimbal system has two degrees of motion and has different positions in free flight. Depending these positions flow characteristics over it varies. In addition, drag reduction systems for the gimbal can be worked in a thesis study. This may lead to designing gimbals having different shapes and forms that eliminates undesired effects of flows and experiences less drag force.

REFERENCES

[1] Headwall Photonics, http://www.headwallphotonics.com, last visited on 12.10.2013.

[2] Diydrones.com, http://diydrones.com/profiles/blogs/quadrotor-project, last visited on 12.11.2013.

[3] Ntvmsnbc, http://www.ntvmsnbc.com/id/25118464/, last visited on 15.11.2013

[4] Military Technology Magazine, http://www.miltechmag.com/2012/08/auvsi-uas-systems-payloads.html

[5] Betz, A. (1925). Ein Verfahren zur direkten Ermittlung des Profilwiderstandes. ZFM, 16, 42-44.

[6] Maskell, E. C. (1973). Progress towards a method for the measurement of the components of the drag of wing of finite span, Royal Aircraft Establishment, TR 72232.

[7] Wu, J. C., Hackett, J. E., & Lilley, D. E. (1979). A generalized wake-integral approach for drag determination in three-dimensional flows, AIAA Paper 79-0279.

[8] Wu, J. C. (1982). A generalized wake-integral approach for drag determination in three-dimensional flows, National Science Foundation, ENG 79-00891.

[9] Van Dam, C. P. (1999). Recent experience with different methods of drag prediction. Progress in Aerospace Sciences, 35, 751-798.

[10] Kusunose K. (1998) Drag prediction based on a wake-integral method, AIAA Paper 98-2723.

[11] Van der Vooren, J. (2008). On drag and lift analysis of transport aircraft from wind tunnel measurements. Aerospace Science and Technology, 12, 337-345.

[12] Giles, M. B., & Cummings, R. M. (1999). Wake integration for three-dimensional flowfield computations: Theoretical development. Journal of Aircraft, 36(2), 357-365.

[13] Son, K., Choi, J., Woo-Pyung, J., & Choi, H. (2010). Effect of free-stream turbulence on the flow over a sphere, Physics of Fluids 22, 045101.

[14] Tamura, T., & Miyagi, T. (1999). The effect of turbulence on aerodynamic forces on a square cylinder with various corner shapes. Journal of Wind Engineering and Industrial Aerodynamics, 83, 135-145.

[15] Suhariyono, A., Kim, J. H., Goo, N. S., Park, H. C., & Yoon, K. J. (2006). Design of precsion balance and aerodynamic characteristics measurement system for micro aerial vehicles. Aerospace Science and Technology, 10, 92-99.

[16] Sun, D., Wu, H., Lam, C. M., & Zhu, R. (2006). Developmet of a small air vehicle based on aerodynamic model analysis in the tunnel tests. Mechatronics, 16, 41-49.

[17] Almeida, R. A. B., Vaz, D. C., Urgueira, A. P. V., & Borges, A. R. J. (2012). Using ring strain sensors to measure dynamic forces in wind-tunnel testing. Sensors and Actuators A, 185, 44-52.

[18] Aksel, M. H. (2008). Notes on fluid mechanics. (3.2 ed., Vol. 2). Ankara: Department of Mechanical Engineering, Middle East Technical University.

[19] White, F. M. (1998). Fluid mechanics. (4th ed.). Kingston: The McGraw-Hill Companies.

[20] Munson, B. R., Young, D. F., & Okiishi, T. H. (2002). Fundamentals of fluid mechanics. (4th ed.). New York: John Wiley & Sons, Inc.

[21] En.convdocs.org, http://en.convdocs.org/docs/index-36931.html, last visited on 20.12.2013.

[22] Snyder, T. (2012). A coupled wake-integral/vorticity confinement technique for the prediction of drag force. (Master's thesis, University of Akron).

[23] Hendrickson, R., Roman, D., & Rajkovic, D. (2006). Drag: An introduction, Informally published manuscript, Virginia Tech.

[24] Strain gauge measurement - a tutorial. (1998). National Instruments Corporation.

[25] Load cells, a primer on the design and use of strain gage force sensors. (1998). Interface, Inc.

[26] Beer, F. P., Johnston, E. R., & DeWolf, J. T. (2006). Mechanics of material. (4th ed.). Singapore: The McGraw-Hill Companies.

[27] Konukseven, İ. (2012) Uncertainty Lecture Notes. Informally published manuscript, Mechanical Engineering Systems Laboratory, Middle East Technical University.

[28] Fluke 922 airflow meter instruction manual. (2008). Fluke Inc.

[29] Köktürk, T. (2010). Aerodynamic analysis of tractor and semitrailer type road vehicles and investigation on drag reduction mechanisms. (Doctoral dissertation, Middle East Technical University, Ankara, Turkey).

[30] Gümüşlüol, Ü. (2006). Experimental investigation of the aerodynamic interactions of vehicle in close-following and passing situations. (Master's thesis, Middle East Technical University, Ankara, Turkey).

[31] Markland, E. (1976). A first course in air flow. Nottingham: Tecquipment Limited.

[32] Potter, M. C., & Foss, J. F. (1982). Fluid mechanics. Michigan: Michigan State University.

APPENDIX A

LOAD-CELL DESIGN

In this part, details of the load-cell design and production are explained.

In the wind tunnel experiments, the main aim is to measure the drag force and to obtain the coefficient of the drag for the gimbal body. Therefore, it is obvious that a force transducer or sensor which must be suitable to the tested body will be used for measuring the drag force. For this purpose, it is decided to design a load-cell for measuring drag force.

It is thought that strain gauges are convenient to be used in this case as a force transducer because they are easy to use. Working principle of them is simple and comprehensible. In addition, they are cheap and easily found in the market. It was also thought that it would be the quickest solution at that stage.

At this point, a few words about strain gauges can be written in order to make the load-cell design meaningful for our experimental study. Strain gauge is an instrument of which electrical resistance alters when subjected to any strain. Proportionality between amount of strain and change in electrical resistance is expected [24] [25].

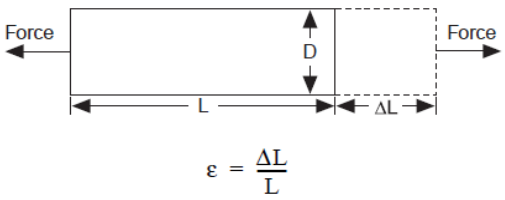

Figure A.1: Definition of strain [19]

Strain can be defined as the measure of deformation of a body caused by a force applied to it.

In addition to tensile stresses seen in Figure A.1, compressive stresses also create strain. Strain gauges are attached to a body which is exposed to any force creating a strain. Then the strain on the body forms same strain on the strain gauge.

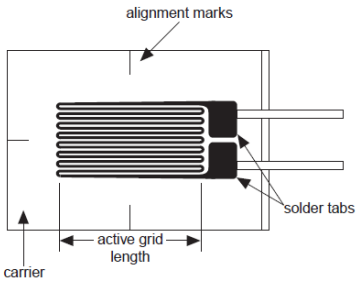

Figure A.2: Strain gauge [19]

Strain gauges differ from each others with their sensitivity to strain. Therefore, a parameter called as gauge factor is defined as the sensitivity of a stain gauge. Gauge factor (GF) can be expressed as:

$$GF = \frac{\Delta R/R}{\Delta L/L} = \frac{\Delta R/R}{\varepsilon} \qquad (A.1)$$

It is the ratio of the proportional resistance change to the strain. It is stated that the gauge factor of a typical strain gauge is around 2 [24].

Practically, the measured strain is very small for the majority of strain measurements. Hence, the value of the resistance change is usually very small and it is hard to detect this small change accurately. Thereby, strain gauges are always used in Wheatsone bridge configuration and the bridge is excited by a voltage generally. By this way the resistance change of the strain gauge can be detected more accurately via measuring the output voltage of the bridge shown in Figure A.3.

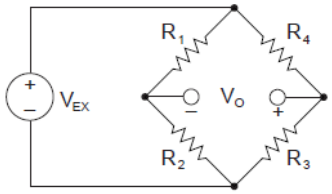

Figure A.3: Wheatsone bridge [19]

In a Wheatsone bridge, output voltage, V_o, corresponding to the excitation voltage, V_{ex}, can be expressed as:

$$V_o = \left(\frac{R_3}{R_3 + R_4} - \frac{R_2}{R_1 + R_2}\right) V_{ex} \qquad (A.2)$$

In the bridge configuration, if $R_1/R_2=R_4/R_3$, the output voltage, V_o, is zero. Resistance change in any arm provides a non-zero output voltage.

In the Wheatstone bridge circuit, the strain gauge can be used instead of R_4. Selecting the other resistances as $R_1=R_2$ and $R_3=R_G$, R_G stands for the strain gauge, provides expressing the output voltage, V_o, as a function of strain, ε. The change in the strain gauge resistance, ΔR, due to any strain can be written as:

$$\Delta R = \varepsilon . R_G . GF \qquad (A.3)$$

and putting it in to the (A.2) yields:

$$V_o = -\frac{\varepsilon . GF}{2}\left(\frac{1}{2 + \varepsilon . GF}\right) V_{ex} \qquad (A.4)$$

This type circuit with a strain gauge usage in Wheatstone bridge is called as quarter-bridge circuit. In this circuit the output voltage is the function of the strain as seen above equation; but, the output voltage function, $V_o(\varepsilon)$, is non-linear due to the strain term in the denominator.

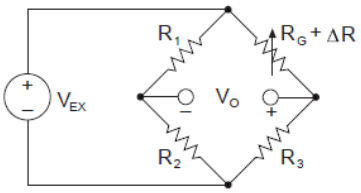

Figure A.4: Quarter-bridge circuit [24]

If it is thought that the excitation voltage is constant for every bridge case, for same amount of strains the output voltage will be same. However, two strain gauges usage in the Wheatstone bridge circuit, so as that one of them is in compression and the other is in tension, increases the output voltage for the same amount of strain and the excitation voltage. Thus, the sensitivity of the bridge to the strain will be increased.

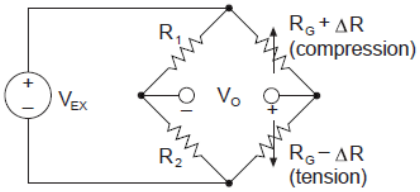

Figure A.5: Half-bridge circuit [24]

For this case, the bridge is called as half-bridge circuit and the output voltage can be re-written as:

$$V_o = \left(-\frac{\varepsilon . GF}{2}\right) V_{ex} \qquad (A.5)$$

Furthermore, sensitivity of the bridge can be doubled if strain gauges are used in all arms of the Wheatstone bridge circuit. In this case all strain gauges are active; two of them are in tension and other two are in compression. Then the bridge is named as full-bridge circuit and the output voltage is:

$$V_o = (-\varepsilon . GF)V_{ex} \qquad (A.6)$$

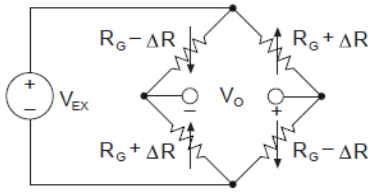

Figure A.6: Full-bridge circuit [24]

In order to have high sensitivity, it is decided to use the full-bridge circuit of strain gauges. After the decision of the circuit configuration, it is necessary to have a casing for the strain gauges which transfers the strain on it directly to strain gauges. Then, the measured output voltage which becomes non-zero by unbalancing the full-bridge strain gauge circuit will be proportional with the strain of the casing and thereby strain gauges. Also, it will be proportional with the force which causes strain on the casing. So, a casing which will carry strain gauges on it must be design firstly.

Designing of the casing of strain gauges is one of the most important parts of the total load-cell design since it has some remarkable points. Conceptual design is the first process of the design of the casing since it is important to identify which force must be measured and how. As stated for many times before, the main aim is to measure the drag force. It can be easily stated that the direction of the drag force exerted on the body by the fluid is always on the direction of the flow. So, it must be thought that the drag force acting on the tested body in wind tunnel must create a strain on the casing, designed for carrying the full-bridge strain gauges circuit, which is assembled with the tested body. Either the drag force itself or the bending moment steaming from drag force can create a strain on the casing. Therefore, it is decided to design a simple beam which will carry strain gauges. This beam is thought as assembled with the tested body. Also it must be fastened to rigid body like for obtaining the bending effect on it. Thus, the drag force exerted on the tested body

creates a bending moment on the beam and strain coming from bending moment can be detected by the full-bridge circuit.

The detailed design of the casing can be made after the decision of the concept. In detailed design, some calculations are performed. Material selection is very essential part of this process as well. Moreover, assembly details of the casing to the tested body must be considered.

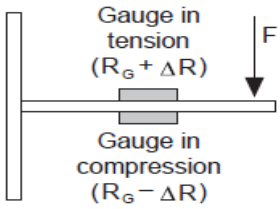

Figure A.7: General representation of the force on the beam [24]

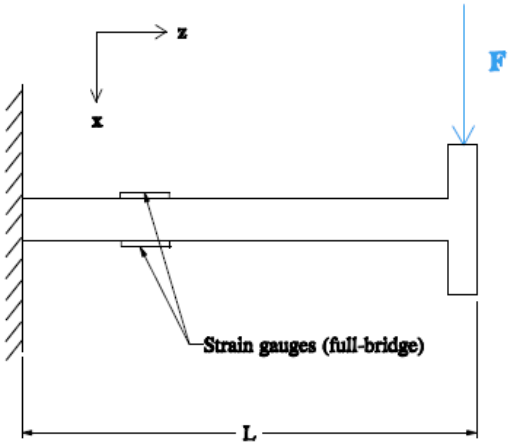

Figure A.8: Simple representation of the designed beam

Some calculations are needed for determining measuring range and strain gauge selection. For the casing designed as a beam, pure bending assumption is made. Moment on the beam causes pure bending and calculations are done according to pure bending assumption [26]. Simple free body diagram of the beam shows that

applied force on the beam is only the drag force. Then, the reaction force and the moment occur on the beam.

Figure A.9: Free body diagram of the beam

With the free body diagram force and moment balance is expressed. It is obvious that F stands for the drag force exerted on the body.

$$\sum F_x = 0 \quad \xrightarrow{yields} \quad R = F \tag{A.7}$$

$$\sum M_y = 0 \quad \xrightarrow{yields} \quad M = F.L \tag{A.8}$$

where L is the length of the beam.

Then, shear force bending moment diagram can be drawn as below.

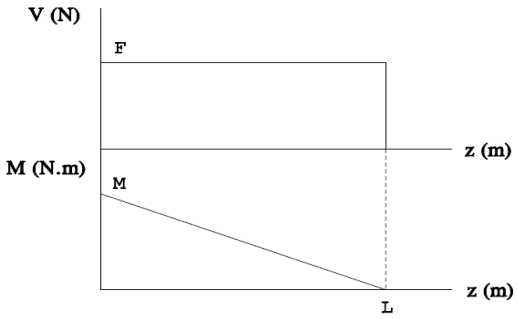

Figure A.10: Shear force-Bending moment diagram

Moment on any z location of beam can be expressed as:

$$M_y = F.z \qquad (A.9)$$

Tensile or compression stress on the beam can be calculated with below formula [26].

$$\sigma_z = \frac{M_y.x}{I} \qquad (A.10)$$

where x is the distance from neutral axis of the beam, I is area moment of inertia of the beam.

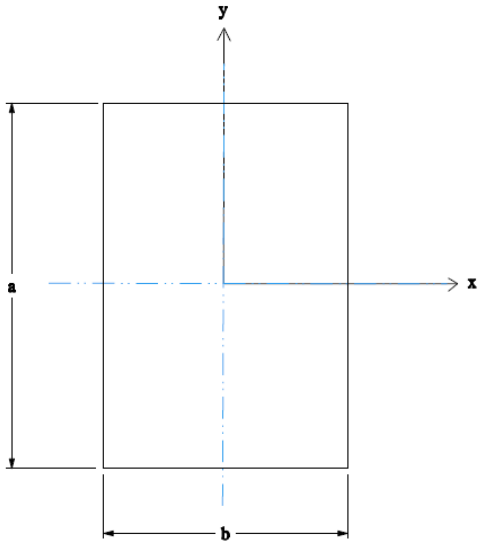

Figure A.11: Cross section and dimensions of the beam

There are two ways for the calculation of the area moment of inertia of the beam. Actually, in a more correct form, there are two types of area moment of inertia. It changes with the moment axis. The usage of it in bending stress equation differs according to bending moment occurred on it. The area moment of inertia is expressed as [26]:

$$I_x = \frac{1}{12} ba^3 \qquad (A.11.a)$$

$$I_y = \frac{1}{12} ab^3 \qquad (A.11.b)$$

For this beam the moment on y axis is applied on the beam; so, I_y is used for the calculation of bending stress.

It is also known that the stress is equal to:

$$\sigma = \varepsilon . E \qquad (A.12)$$

where E is the modulus of elasticity of the beam material and ε is the strain.

Via calculation steps above mentioned the strain can be obtained. Estimating the approximate strain value is essential since strain gauges used in the full-bridge circuit are selected according to this strain value.

It can be easily seen that strain gauges are glued on the plane of maximum stress. Then the strain of this plane can be re-written as:

$$\varepsilon = \frac{M_y . x}{E . I_y} \qquad (A.13)$$

Rearranging the above equation by replacing distance of neutral axis to the maximum stress plane x as b/2, moment about y-axis M_y with F.z and the area moment of inertia as in equation (A.11.b) gives:

$$\varepsilon = 6 \frac{F . z}{E . a . b^2} \qquad (A.14)$$

The strain is estimated with (A.14) basically which gives the opportunity of strain gauge selection as desired. It can be interpreted that the strain value can be adjusted optimally by selecting the independent variables z, a and b and the dependent variable E, which is dependent to material. The force, F, is a particular value for the particular free stream case. It is estimated once for the maximum case and used in strain equation as a constant.

Drag force is estimated firstly for the maximum case. Calculations and the selection of design values of variables are performed for the maximum drag force case to be on safe side. Drag force is written as the function of some variables as, by equation (3.5), $D(\rho, U^2, A_f, C_d)$ where A_f is the frontal area of the body. Density of air and the frontal area have particular values for the drag estimation. Free stream velocity, U, is selected as 30 m/s maximum. However, the value of the drag coefficient, C_d, for the gimbal is unknown. There is not any information about it in literature also. Therefore, the drag coefficient is thought to have a value of 1 approximately to estimate the drag force. Reason of this drag coefficient estimation as 1 can be explained. The gimbal has a blunt body characteristic and its shape is a combination of sphere and circular cylinder. Also by making use of the literature it is assumed as about 1. Then, the drag force is calculated approximately as 8.5 N for being used in strain calculations of the beam.

Strain value is very significant for strain gauges since it directly affects the sensitivity. Generally strain has the unit of micro strain. Actually the unit of it is mm/mm or in/in. Since general magnitude of strain is in micron levels, they are used in bridge configuration as previously mentioned. Nevertheless, sensitivity can be increased a bit by selecting the proper material having a low modulus of elasticity.

Moreover, material selection is significant when considering some other factors. Manufacturing type of the designed beam is most probably machining since it is quick, successful and cheap solution and very common in industry. If the machining

is chosen as a production type, the selected material must be a metal having high machinability property since metals are more commonly used in machining. In fact, plastic and its derivatives such as delrin, polyamide or ABS can be considered as a beam material since elasticity of them are in reasonable levels; however, machining of them is usually more time-consumer and thereby more expensive compared with metals although they can be regarded as easy-machined materials in industry. It is sometimes hard to obtain desired geometric dimensions and tolerances when machined and it prolongs the machining time and thereby the machining cost.

Another concern of material selection is regular mount of strain gauges to the beam surface and quality of these surfaces. Mounting of strain gauges is a sensitive process and generally done by the help of suitable adhesives. Hence, the beam material must be convenient for adhesives used in sticking. Plastics and sub-plastics are artificial poly-carbons and adhesives used for strain gauges cannot be work with them. Even they can react. Furthermore, the mounting place of strain gauges must be a part of design considerations. Surface roughness and quality of the mounting surface is important for proper work of strain gauges. Flatness of these surfaces must not exceed determined limits. In machining of plastics it is rather difficult to obtain optimal flatness tolerance and qualified surface finish.

Due to discussed reasons, it is decided to manufacture the beam from a metal. Most commonly used engineering metals in machining are steel and aluminum. They have both high machining capabilities. Aluminum is selected since it has a lower modulus of elasticity and density which provides lightness compared to the steel. The aluminum alloy 6061-T6 is used as the beam material.

After material selection, mechanical details of the load-cell are designed. Critical dimensions are determined and calculation for strain and yield stress is done. Strain calculation is very significant in terms of selecting suitable strain gauge.

Calculations via Mathcad can be seen below.

$F := 8.5N \qquad z := 95mm$

$a := 10mm \qquad b := 3mm \qquad x := \frac{b}{2}$

$I := \frac{1}{12} \cdot a \cdot b^3 = 2.25 \times 10^{-11}\, m^4$

$M := F \cdot z = 0.807\, J$

$\sigma := \frac{M \cdot x}{I} = 5.383 \times 10^7\, Pa$

$E := 69GPa \qquad$ for Al 6061-T6

$\varepsilon := \frac{\sigma}{E} = 7.802 \times 10^{-4}$

Figure A.12: Design calculations via Mathcad

It must be noted that yield strength of Al 6061-T6 is 241 MPa. Calculated stress is below this value and it can be used without any failure. Also the strain is calculated as 780 μstrain. This is a reasonable value for proper strain gauge selection which will be used in full-bridge configuration.

The beam and legs which will be used for fixing the beam to the rigid body such as ground are modeled via Pro Engineer.

Figure A.13: Solid model of the leg

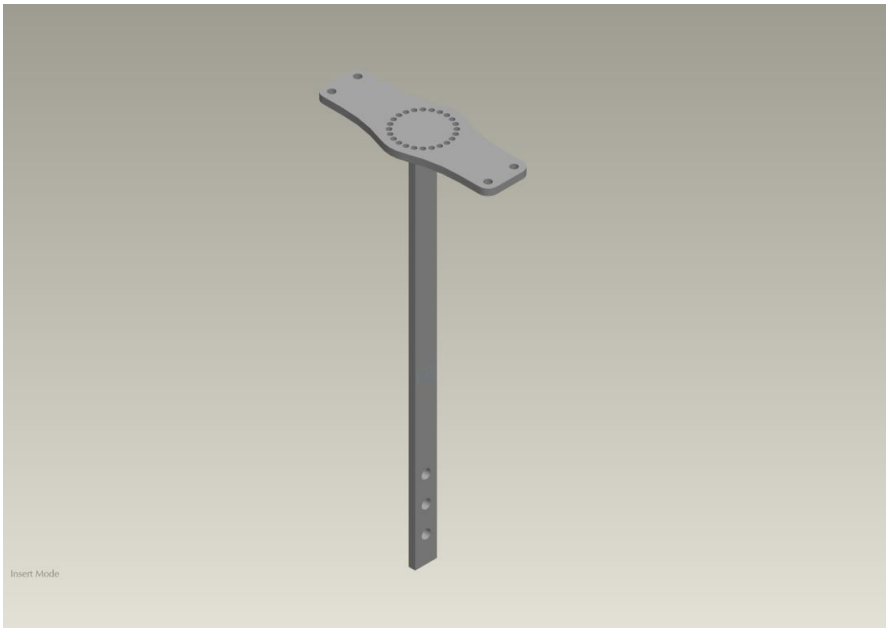

Figure A.14: Solid model of the beam

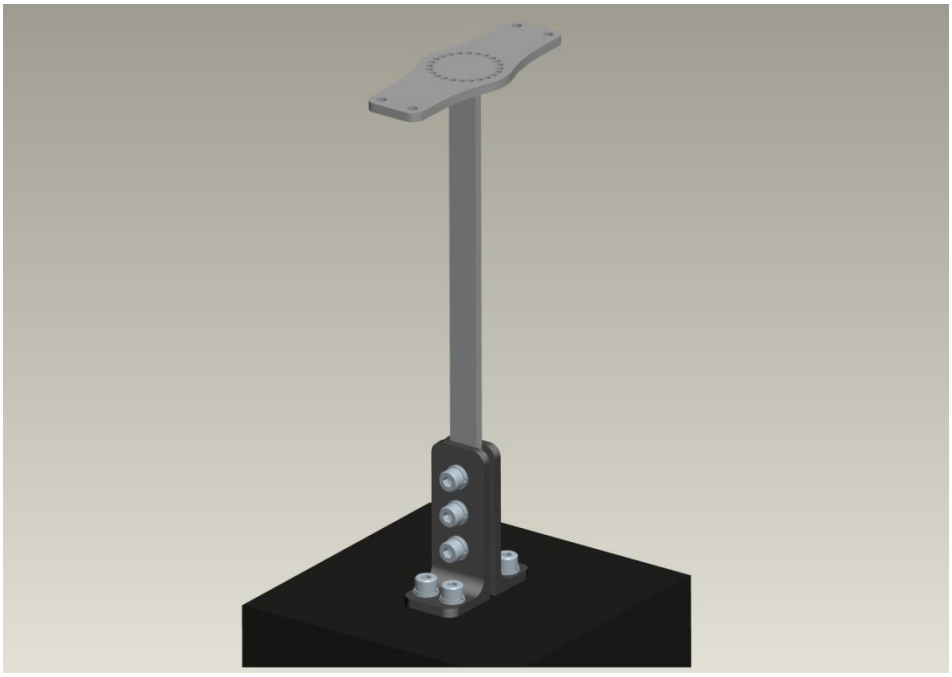

Figure A.15: Assembly of the beam and legs to a rigid body

Assembly of the beam and legs to a rigid body can be seen in Figure A.14. M4 screws and nuts are used to assemble the beam and legs. M4 screws are also used for fixing the assembly to a rigid body.

An important point of design is holes located on upper surface of the beam. As a footnote, they can be seen more detailed technical drawing attached to end of this part. There are two types of through holes which are distinct from each other by their diameters located on the upper surface. Holes having bigger diameters and located on the four sides of upper surface are for assembling of the load-cell to any body desired to be tested in the wind tunnel such as Ahmed body, MIRA model etc. Other smaller holes are used for assembling it to the gimbal body.

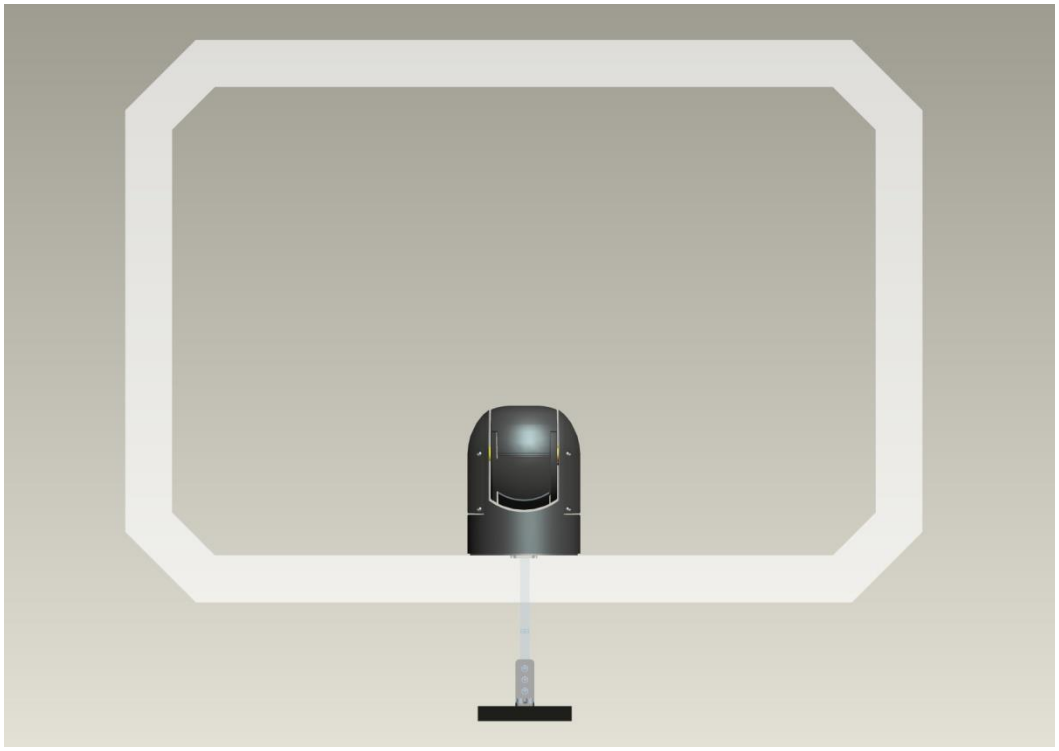

Figure A.16: Assembly of the gimbal and the load-cell (balance) in the wind tunnel

Also a modal analysis via Ansys Workbench is performed and mode shapes and related frequencies are obtained for validating the design before the manufacturing process (Figure A.16). Then, first prototypes of the beam and legs are manufactured. Five axis milling machine is used for manufacturing prototypes. Finally, the load-cell is ready with sticking the strain gauges on it. (Images of it can be seen in Chapter 4.)

Calibration process and data of the load-cell can be found in Chapter 5. With 18V excitation voltage, the sensitivity of the load-cell is measured as 0.012 N approximately. In addition, rational measurement upper limit for the load-cell can be estimated as 10 N.

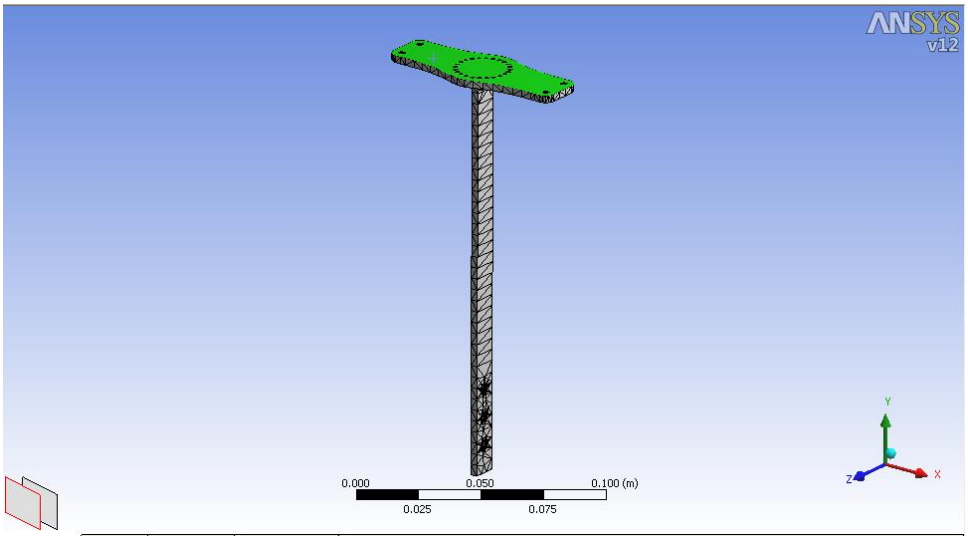

Figure A.17: Meshing for finite element analysis in Ansys

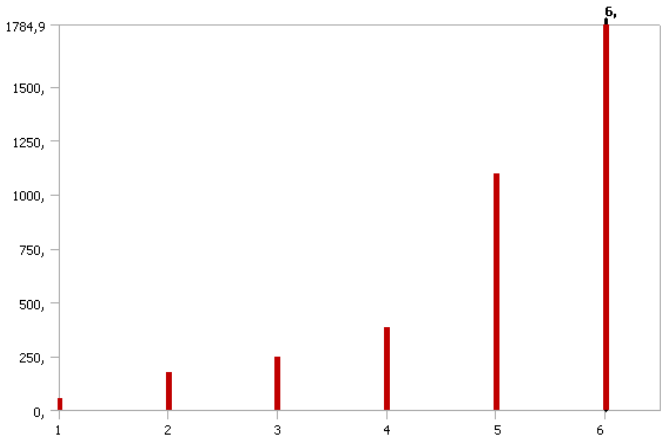

Mode	Frequency [Hz]
1,	53,644
2,	176,24
3,	246,94
4,	381,01
5,	1094,9
6,	1784,9

Figure A.18: Natural frequencies for modes

Figure A.19: Manufactured prototypes of the beam and legs

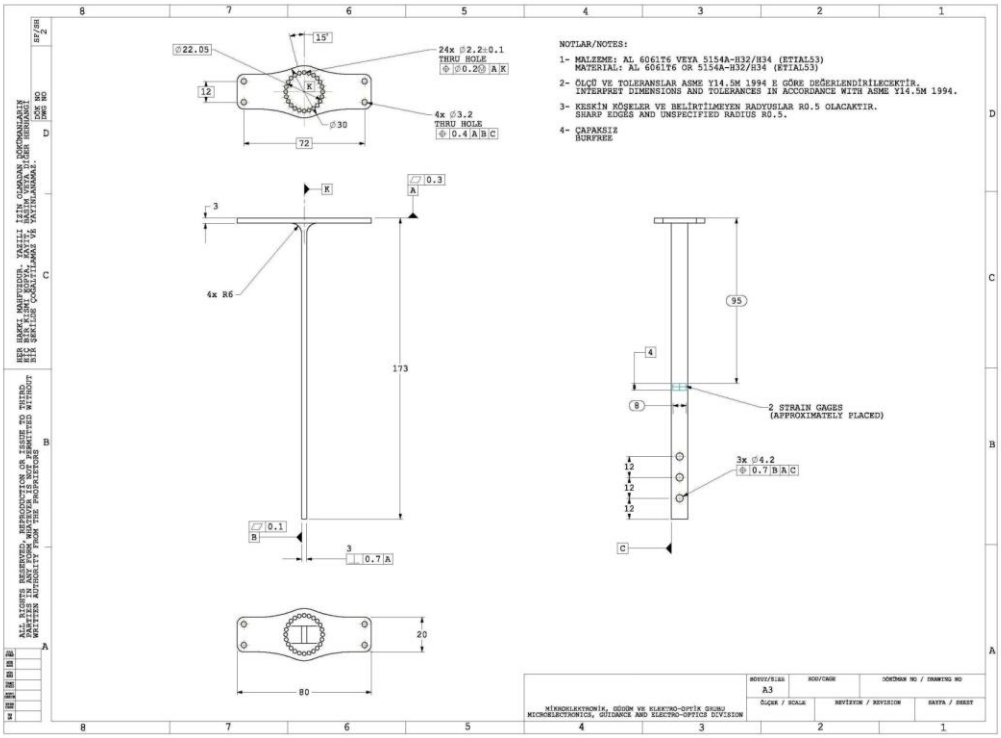

Figure A.20: Technical drawing of the beam

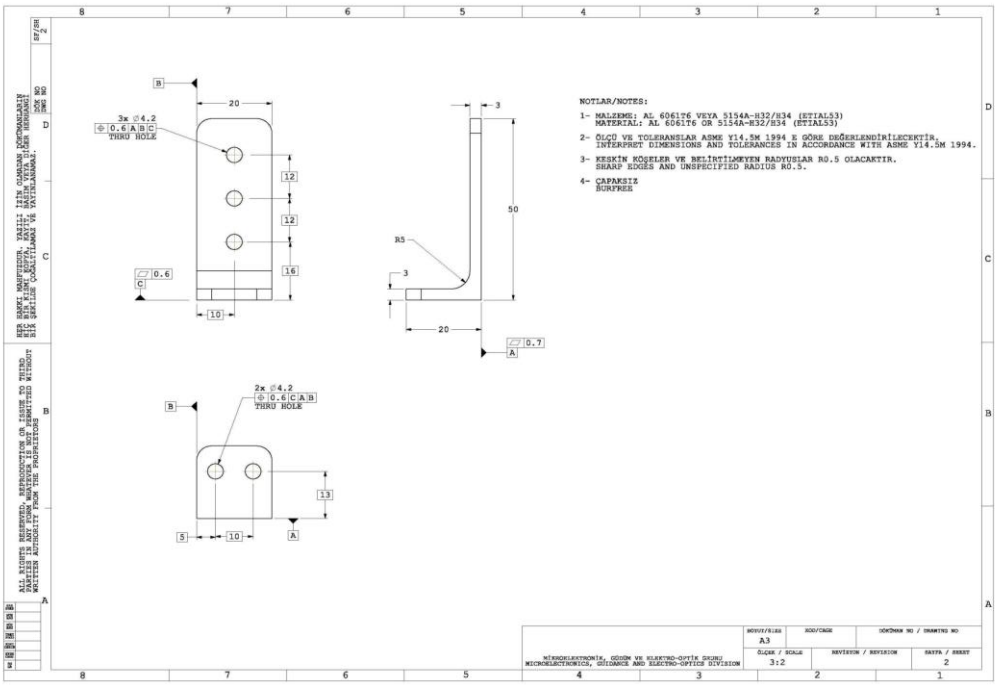

Figure A.21: Technical drawing of the leg

APPENDIX B

UNCERTAINTY ANALYSIS

Uncertainty analysis is necessarily performed for experimental studies since experimental measurements are prone to uncertainties. Every experimental measurement has an uncertainty. Moreover, uncertainty in calculations is usually encountered as a combination of uncertainties of variables used in calculations.

If Q is a function of the variables, it can be expressed as [27]:

$$Q = Q(x_1, x_2, \ldots., x_n) \tag{B.1}$$

It takes the form as:

$$Q(x_1, x_2, \ldots., x_n) = \overline{Q} + \delta Q \tag{B.2}$$

where δQ is an overall uncertainty.

Then, the uncertainty can be expressed as [22]:

$$\delta Q = \left[\left(\frac{\delta Q}{\delta x_1}\delta x_1\right)^2 + \left(\frac{\delta Q}{\delta x_2}\delta x_2\right)^2 + \cdots + \left(\frac{\delta Q}{\delta x_n}\delta x_n\right)^2\right]^{1/2} \tag{B.3}$$

where δx_1, δx_2, …, δx_n are uncertainties of variables.

For example, uncertainty of the drag coefficient is calculated with (B.3)

B.1 Uncertainty in the density of air

Air is assumed as a ideal gas and the density of an ideal gas is expressed by the help of ideal gas relation as:

$$\rho = \frac{P}{R.T} \qquad (B.4)$$

where R is the gas constant, P is the pressure and T is the temperature.

Uncertainty of the density can be expressed by the help of (B.3) as:

$$\delta\rho = \left[\left(\frac{\delta\rho}{\delta P}\delta P\right)^2 + \left(\frac{\delta Q}{\delta T}\delta T\right)^2\right]^{1/2} \qquad (B.5)$$

and partial derivatives are:

$$\frac{\delta\rho}{\delta P} = \frac{1}{R.T} \qquad (B.6)$$

$$\frac{\delta\rho}{\delta P} = -\frac{P}{R.T^2} \qquad (B.7)$$

During experiments, atmospheric pressure is 681 mmHg and the temperature is 27.4 ^{o}C. Then, it can be said that uncertainty in temperature is 0.05 ^{o}C and uncertainty in pressure is 0.5 mmHg since scale of them is 0.1 ^{o}C and 1 mmHg. The ideal gas constant, R is 0.287kJ/kgK.

With the help of (B.5), (B.6) and (B.7) and measurement values and uncertainties the uncertainty in the density of air is calculated as $\delta\rho=\pm 6.44\text{x}10^{-4}$ kg/m^3.

B.2 Uncertainty in the free-stream velocity

Uncertainty in the free-stream velocity can be interpreted as δU=±0.37 m/s for free stream of 14.59 m/s according to technical data sheet of air flow meter. It is given that ±2.5% of the measurement value is predicted as an accuracy range [28].

B.3 Uncertainty in the frontal area

Frontal area of the model is calculated as:

$$A_f = \frac{\pi r^2}{2} + 2rL \qquad (B.8)$$

Uncertainty of the frontal area can be expressed as:

$$\delta A_f = \left[\left(\frac{\delta A_f}{\delta r}\delta r\right)^2 + \left(\frac{\delta A_f}{\delta L}\delta L\right)^2\right]^{1/2} \qquad (B.9)$$

and partial derivatives are:

$$\frac{\delta A_f}{\delta r} = \pi r + 2L \qquad (B.10)$$

$$\frac{\delta A_f}{\delta L} = 2r \qquad (B.11)$$

r and L are the dimensions of frontal area and they are measured by a caliper as 60 mm and 80 mm respectively. The sensitivity of the caliper is 0.01 mm and then uncertainty in dimensions can be taken 0.005 mm.

By using above values and equations (B.9), (B.10) and (B.11) uncertainty in the frontal area is calculated as $\delta A_f = \pm 1.84 \times 10^{-6}$ m^2.

B.4 Uncertainty in the drag force

Uncertainty in the drag force is $\delta D = \pm 0.05$ N according to the load-cell design.

B.5 Uncertainty in the drag coefficient

Drag coefficient is expressed as:

$$C_d = \frac{2D}{\rho A_f U^2} \qquad (B.12)$$

Uncertainty of the drag coefficient can be expressed by the help of (B.3) as:

$$\delta C_d = \left[\left(\frac{\delta C_d}{\delta D} \delta D \right)^2 + \left(\frac{\delta C_d}{\delta \rho} \delta \rho \right)^2 + \left(\frac{\delta C_d}{\delta A_f} \delta A_f \right)^2 + \left(\frac{\delta C_d}{\delta U} \delta U \right)^2 \right]^{1/2} \qquad (B.13)$$

and partial derivatives are:

$$\frac{\delta C_d}{\delta D} = \frac{2}{\rho A_f U^2} \qquad (B.14)$$

$$\frac{\delta C_d}{\delta \rho} = \frac{-2D}{\rho^2 A_f U^2} \qquad (B.15)$$

$$\frac{\delta C_d}{\delta A_f} = \frac{-2D}{\rho {A_f}^2 U^2} \qquad (B.16)$$

$$\frac{\delta C_d}{\delta U} = \frac{-4D}{\rho A_f U^3} \qquad (B.17)$$

Sample calculation for the case of U=14.59 m/s and D=2.46 N with calculated ρ and A_f=1.7x10^{-2} m^2 and known uncertainties from previous steps gives δC_d=±0.29.

APPENDIX C

BLOCKAGE CORRECTION METHOD USED IN CALCULATIONS

When wind tunnel measurements are the subject, it is stated that due to existence of wind tunnel walls the flow over the body is affected. It is accelerated around the tested body since wind tunnel walls reduces the flow area. Therefore, free stream conditions and wind tunnel conditions differ from each other. This situation also affects measurement results. Especially drag force or coefficient of drag is measured larger in wind tunnel experiments. Hence, they must be corrected by a factor calculated for some criteria.

The total blockage has two types: solid blockage and wake blockage. Presence of the model in the wind tunnel is called as solid blockage. At body locations in the wind tunnel the flow velocity increases and thus the pressure decreases. It is expressed in above paragraph basically. Wake blockage is occurred due to the wake region behind the body. It also affects the flow velocity and pressure gradient. It brings additional drag force for wind tunnel measurement case [29] [30].

Short summary of the blockage in the wind tunnels is considered as sufficient. In literature, there are many works and papers related to blockage and its correction methods. Various methods of blockage correction are available. Many of them are complex solutions and details of them can be found in literature.

Since necessary measurements for many blockage corrections method are not performed during experiments, also not having deeper knowledge related to them, they cannot be used for correcting the drag force results. The results of drag

coefficient are corrected by the continuity method. It is a simple method and easily used in correction calculations. It is stated that despite of being simple, the continuity method yields better overall correction than some methods for blockage ratios 3.5-10% and also for nor bluff neither streamlined bodies it could be interpreted as adequate [30].

Continuity equation is expressed for the wind tunnel test section with the tested body as,

$$U.A_{tunnel} = U_{actual}.\left(A_{tunnel} - A_f\right) \qquad (C.1)$$

where U is the free-stream velocity, U_{actual} stands for actual velocity around the model, A_{tunnel} is the area of the wind tunnel section and A_f is the frontal area of the model. Measured drag coefficient can be written as;

$$C_{d\_measured} = \frac{2D}{\rho A_f U^2} \qquad (C.2)$$

Inserting the actual velocity instead of free-stream velocity in the drag coefficient equation gives:

$$C_{d\_corrected} = \frac{2D}{\rho A_f U^2 \left(\frac{A_{tunnel}}{A_{tunnel} - A_f}\right)^2} \qquad (C.3)$$

Then, re-expressing (C.2) and (C.3) together,

$$C_{d\_corrected} = C_{d\_measured}\left(\frac{A_{tunnel} - A_f}{A_{tunnel}}\right)^2 \qquad (C.4)$$

Due to the velocity increase around the model in the wind tunnel, drag coefficient comes out larger in measurements.

If (C.4) is re-expressed with high order terms in it and high order terms are neglected, (C.4) becomes;

$$C_{d\_corrected} = C_{d\_measured}\left(1 - 2\frac{A_f}{A_{tunnel}}\right) \qquad (C.5)$$

Neglecting high order terms is a suitable action, especially for low blockage values. The blockage value for the gimbal is calculated as 0.045, which is a low value and corrections are made according to (C.5).

APPENDIX D

NUMERICAL APPROACH FOR CALCULATING DRAG FORCE

As stated in some parts of Chapter 6, velocity profile at the exit plane of selected CV is obtained from surface fitting via Matlab. After that, these velocity profiles are used in equation (6.6) for evaluating the drag force. Results of estimations for different x-y planes can be seen in Chapter 6. Actually, big differences from the load-cell results are met for some x-y planes. For further wake regions and higher free stream velocities estimation results get closer to the load-cell results.

In equation (6.6), terms except exit momentum flux which is the last integral term consisting u^2 can be easily handled. Yet, integration is necessary for this term. It is achieved by using surface fitting as stated before. However, velocity functions for exit planes coming from surface fittings can be interpreted as error sources. Actually, as seen in Figure D.2, at some points it is very successful and covers measured values; but, at some different points it undershoots or overshoots. Although R^2 values of fittings are usually higher than 0.91, it increases calculation errors when combining with measurement errors. Therefore, numerical integration of this double integral term can be an alternative. For this purpose, u velocities in discretized y-z planes are used to evaluate the integral term.

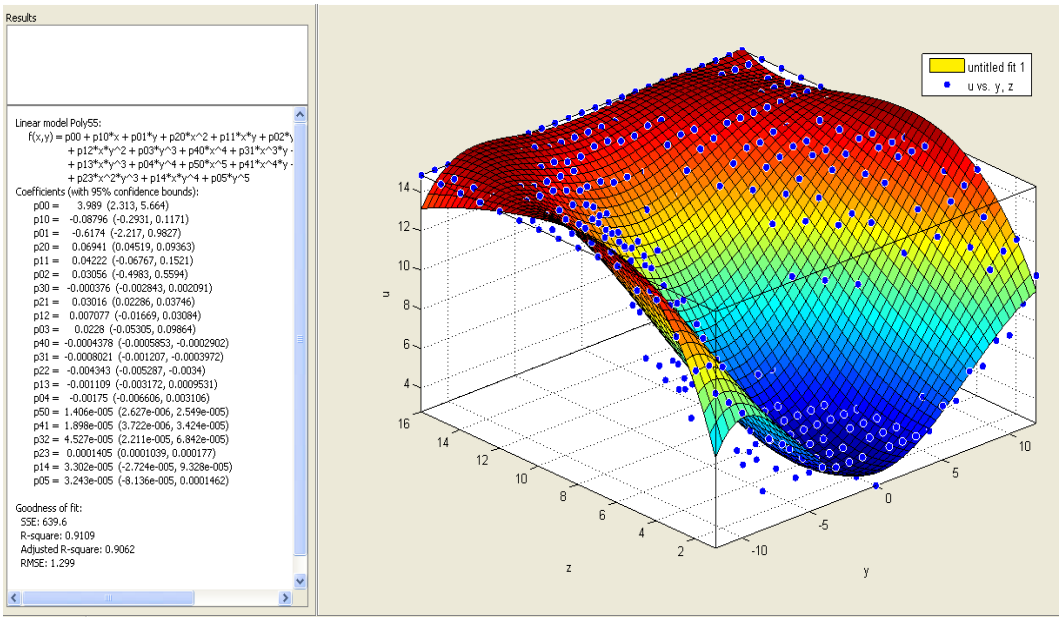

Figure D.1: Surface fitting example of exit plane velocity, u(y,z)

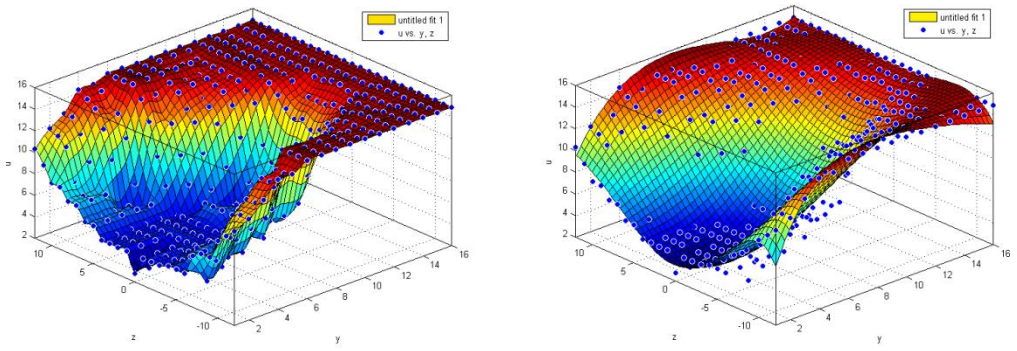

Figure D.2: Velocity distribution and corresponding surface fitting for free stream of 14.59 m/s for x=20 cm plane

Different methods can be used for numerical integration. General logic behind it is to calculate the volume under the surface of velocity distribution. For this purpose two methods are used for the sample calculation of x=20 cm plane.

Firstly, triangular meshes are discretized for data array. Actually, in 3D space a plane passes through three points. Triangular surfaces are created for each three data, next to each other, and the summation of the volume under these triangular surfaces gives the result.

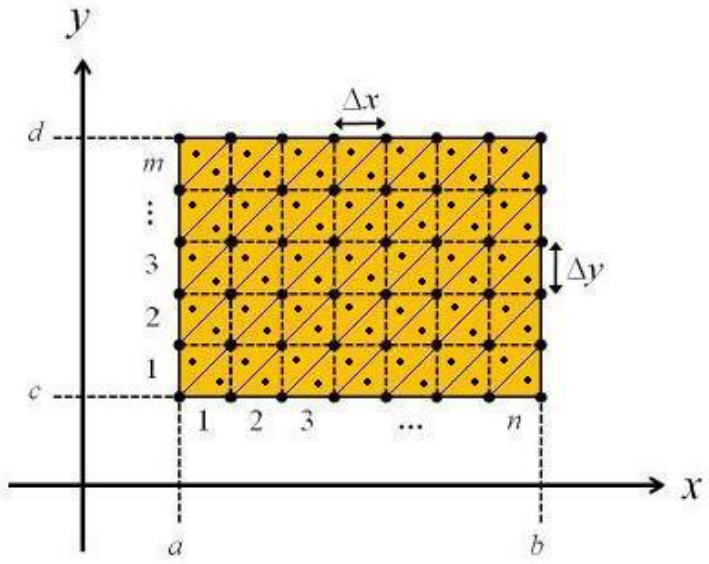

Figure D.3: Triangular meshes for data

Volume under a triangular element is calculated with coming method. The data is accepted as f(x,y)=z function. Let's write z values of first triangular element in Figure D.3 as $f(a,c)=z_1$, $f(a,c+\Delta y)= z_2$ and $f(a+\Delta x,c+\Delta y)= z_3$ and assume that $z_3 > z_2 > z_1$. Then the volume of one element can be expressed by using volume of triangular prism as:

$$V' = \Delta x \Delta y \frac{z_1}{2} + \Delta x \Delta y \frac{z_2 - z_1}{3} + \Delta x \Delta y \frac{z_3 - z_2}{3} \qquad (D.1)$$

Then the total volume can be found by summation of all triangular sub-volumes. It can be noted that all triangular surfaces are connected each other and the total

volume is the volume under the whole surface which is a combination of all triangular surfaces.

In addition, another method is use for numerical integration. Data is discretized as rectangular sub-domains, actually square since for this case Δx= Δy.

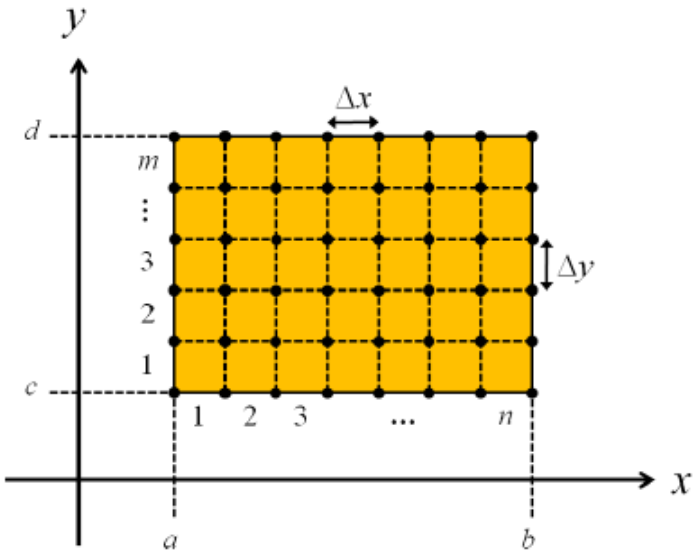

Figure D.4: Rectangular sub-domains of discretized data

Volume of each sub-domain can be calculated by using four corners of sub-domain. Average of values at four corners of rectangular element is used for volume calculation. It can be expressed as:

$$V'_{ij} = \frac{1}{4}\Delta x \Delta y \left(f(x_i, y_j) + f(x_{i-1}, y_{j-1}) + f(x_i, y_{j-1}) + f(x_{i-1}, y_j) \right) \quad (D.2)$$

where x_i=a+iΔx and y_j=c+jΔy, with i = 0, 1, 2,…, n and j = 0, 1, 2,…, m. Again, the summation of each volume gives the total volume. It is different from first method since volume of each element is computed from average values of corners.

Sample drag force calculation is performed by using with these numerical methods for free stream of 14.59 m/s of x=20 cm plane. Drag forces are found as 2.52 N and 2.64 N and percent differences from load-cell measurement results are 2.5% and 7.6% respectively. First method using triangular meshes evaluate the output flux term slightly higher than the second method. Therefore, drag force found by first method is a bit lower and thereby closer to load-cell measurement result. The reason of better prediction with triangular meshes is that the method uses actual values for calculating each sub-volume instead of approximating with averages. Actually, both numeric methods gives better drag force estimations compared to surface function fitting method since computed data set discard of some undershoots and overshoots steming from surface function fitting. Numeric methods use exact values of measurements. This explains some big differences of wake integration method from load-cell measurement. It is obvious that calculation method of exit momentum flux affects results and these big differences. Evaluation of drag force for further planes with numerical methods can give better results and provide to determine optimum control volume for the wake integration method.